ELECTRONIC PHENOMENA AT GRAIN BOUNDARIES AND OTHER DEFECTS IN SILICON

A thesis
presented to the University of Manitoba
in partial fulfillment of the
requirements for the degree of
Doctor of Philosophy
in
Electrical Engineering

by

A.W. de Groot

Winnipeg, Manitoba, 1983

ELECTRONIC PHENOMENA AT GRAIN BOUNDARIES AND OTHER DEFECTS IN SILICON

by

Alex Wouter de Groot

A thesis submitted to the Faculty of Graduate Studies of the University of Manitoba in partial fulfillment of the requirements of the degree of

DOCTOR OF PHILOSOPHY

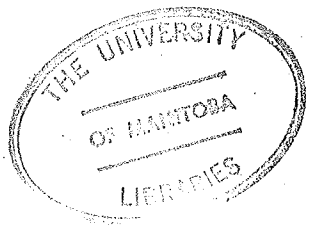

ABSTRACT

This thesis consists of experimental and theoretical investigations of various electronic defect phenomena in silicon.

Experimental investigations of the photovoltaic properties of metal-silicon Schottky barriers are reported, in which edge collection of the photocurrent is dominant as in the majority-carrier grating solar cells proposed by Green. Both elemental metals and alloy Schottky electrodes, and both crystalline and semicrystalline cast silicon have been studied. The superposition principle for dark currents and photocurrents is shown unambiguously to be violated, and the effects of grain boundary recombination and shunt resistance are identified. Limitations to the operation of these devices above the semi-empirical limit of continuous Schottky barrier solar cells is seriously compromised by enhanced space-charge recombination current. This results from the large photocurrent densities for low contact area/active area ratios. The treatment of the space-charge recombination mechanism under optical illumination follows the normal Sah-Noyce-Shockley approach, but we introduce here a built-in "recombination potential" to encompass the non-zero recombination for short-circuit conditions.

An extension of Shockley-Read-Hall kinetics is presented for interface states at grain boundaries in silicon. The emission of majority carriers by these states is generalized to include thermionic-field emission (TFE), which is shown to be important in many practical cases. Comparison is made with experimental results obtained on studies of isolated grain boundaries in silicon. One of the principal results is that energy distributions of interface states deduced from electrical characteristics of grain boundaries must be interpreted

using a model which includes TFE. The importance of TFE increases with the doping concentration of the silicon, N, and the voltage applied across the grain boundary, V, and decreases with increasing temperature. It is legitimate to neglect TFE from the interface states and consider pure thermal emission only for $NV \lesssim 10^{16} cm^{-3}V$ at a temperature of 300 K, or $NV \lesssim 10^{15} cm^{-3}V$ for 130 K.

The above theory, developed for interface states at a single energy level is expanded to encompass states distributed in energy. It is found that the interface state energy distribution in grain boundaries is temperature dependent. This conclusion is based upon experimental observations of the emission rate over a wide temperature range. The physical interpretation of this result is that contraction of the silicon material at reduced temperatures occurs primarily at the grain boundaries. This affects the potential wells which determine the interface state wave functions. Interpretation of the interface state density according to the Seager-Pike-Ginley treatment which, in addition to other limitations, neglects thermionic-field emission, overestimates the density and underestimates the interface state energies relative to the majority carrier band. The theoretical treatment of interface state emission presented in this thesis is expected to be easily extended to the treatment of similar processes at other semiconductor interfaces.

A cryogenic system, employed in the above investigations, which offers several advantages over traditional low temperature systems was designed and constructed. Controlled temperatures from approximately -180°C upward and with a stability to within ± 0.5°C

could be maintained over extended periods. Specific temperature vs time progressions can be obtained through application of an external reference voltage signal. For example, linear temperature sweeps of rates up to at least 4°C/min and with a linearity better than 0.5% are possible. The entire system consists of a thermometer with analog output and a power supply (± 8 V, 10 mA and 5-25 V, 1.25 A) in addition to the unit described here; the cost of materials for this latter unit is less than $25.00. Appropriate quantities of nitrogen gas under pressure and liquid nitrogen are required.

ACKNOWLEDGEMENTS

The author wishes to thank Prof. Dr. H.C. Card for his patient supervision and never faltering encouragement throughout the extent of this project.

The author is also indebted to his colleagues in the Materials and Devices Research Laboratory at the University of Manitoba for valuable discussions, suggestions, and assistance in some of the experimental work.

Ms. C. Bain's stoical acceptance of innumerable iterations, revisions, corrections, and improvements - real or imagined - during the typing and collation stages of this work was greatly appreciated.

A special debt of gratitude is due to Mr. M. van der Tol of the Numerical Applications Group at the University of Manitoba for his invaluable contribution to the computational work.

Financial assistance from the Natural Sciences and Engineering Research Council of Canada is also gratefully acknowledged.

CONTENTS

CHAPTER I

INTRODUCTION

The material in this thesis is arranged so that each chapter is self-contained, with its own references and conclusions. As a result, a few references are listed in more than one chapter, and some repetition in closely related chapters such as CH III and CH IV could not be entirely avoided. It is hoped, however, that rather than being distracting, this will serve to reinforce some of the common basic concepts.

The work presented here comprises a combination of experimental and theoretical investigations of defect phenomena in silicon with an emphasis on polycrystalline silicon, which is a form of this material characterized by a lack of uniform crystal orientation throughout a sample of any appreciable size. Instead, we find distinct regions - or grains - where each grain has its own crystal orientation which differs from that of its neighbours. The interfaces between the grains are the grain boundaries.

Average grain sizes can vary substantially, depending on the fabrication methodology, from fine-grained (200 - 500 Å) through small-grained and medium-grained to large-grained (≈ 1 mm). The latter material is often referred to as semicrystalline. Thus, polycrystalline silicon covers the wide range between amorphous silicon, characterized by a total absence of a crystal structure, and crystalline material which is produced - within the limitations of fabrication technology - as single crystals of considerable dimensions.

Polycrystalline silicon finds important application in terrestrial solar cells on account of its significantly lower fabrication cost compared to crystalline material. Indeed, even continuous ribbons can be fabricated today, whereas crystalline material is limited in size to slices of about 10 cm in diameter.

Another area where thin films of polycrystalline silicon show great promise is integrated circuit technology, and particularly in very large scale integrated circuits. Typical applications here include passive loads and interconnections. A major advantage in these roles compared to the traditional methods - diffused resistors and metallic interconnections - is the freedom of positioning relative to diffused components and the possibility of multilevel structures, both leading to savings in chip area.

Current transport through polycrystalline material is governed by transport across the grain boundaries rather than by the bulk transport properties of the crystalline material in the grains. The theory of conduction through the grain boundaries is based upon a model in which potential barriers occur at the boundary. These barriers are the result of charge trapped in the interface states, i.e. the electronic states which are distributed in energy within the bandgap of the material. The electronic states originate from the disturbance of the crystal periodicity at the grain boundary.

The first investigations of polycrystalline semiconductor materials date back to circa 1950, when Volger[1] postulated that polycrystalline semiconductor thin films were composed of regions of high resistivity (grain boundaries) separating regions of low resistivity, the crystalline grains. Taylor, Odell and Fan[2] were the first to study single grain boundaries and to present a model for current transport across a grain boundary which was based on carrier diffusion through two opposing space charge regions.

Vogel, Read and Lovell[3] performed an experimental investigation of recombination at grain boundaries, and although they concluded

the existence of a large number of recombination centres at the grain boundary, they were unable to estimate their density.

The work of Petritz[4] on photoconductivity in polycrystalline semiconductor thin films led to a transport model in which thermionic emission, rather than diffusion, was the major bottleneck to majority carrier flow across the grain boundary.

Subsequent workers have generally adopted the thermionic emission theory although the two transport mechanisms are not mutually exclusive; rather, it is a matter of which phenomenon is dominant.

The work of Seto[5] was significant for the understanding of polycrystalline silicon, the earlier work having concentrated upon germanium. His results, interpreted in terms of thermionic emission theory, provided substantial agreement between theory and experiment. Nevertheless, diffusion theory will also produce predictions which are in agreement with Seto's experimental results.

Systematic analysis of carrier recombination in optically illuminated polycrystalline material by Card and Yang[6] produced quantitative results on the dependence of minority carrier lifetime on doping concentration, grain size and grain boundary interface state density.

Seager, Pike and Ginley performed theoretical calculations and several experimental investigations of isolated grain boundaries in silicon.[7,8] They assumed thermionic emission of majority carriers to be the dominant transport mechanism, and observed varistor-like behaviour in silicon bicrystals. They also developed a theory for the thermal emission from interface states, which will be extended in this thesis to encompass thermionic-field emission as well.

The second chapter in this thesis deals with the application of polycrystalline silicon in solar cells. It is shown how the grain boundaries affect the performance of these devices. In Chapter III a theoretical model is presented for thermionic-field emission from grain boundary interface states at a single energy level. This phenomenon must, under appropriate conditions, be considered together with thermal emission. The theory of this chapter is extended to the case of interface states distributed in energy in Chapter IV. There, the theory is compared with experimental data for a specific case. It is also shown how the relevant parameters of a sample may be determined. The conclusions include a hypothesis concerning the temperature dependence of the interface state energy distribution. Chapter V describes the design, construction, and performance of a cryogenic system which was used in the experiments involving low temperatures. Finally, recommendations for further work are presented in Chapter VI.

References

1. J. Volger, 'Note on the Hall Potential Across an Inhomogeneous Conductor', Phys. Rev., 9, pp. 1023-1024, 1950.

2. W.E. Taylor, N.H Odell and H.Y. Fan, 'Grain Boundary Barriers in Germanium', Phys. Rev., 88, pp. 867-875, 1952.

3. F.L. Vogel, W.T. Read and L.C. Lovell, 'Recombination of Holes and Electrons at Lineage Boundaries in Germanium', Phys. Rev., 94, pp. 1791-1792, 1954.

4. R.L. Petritz, 'Theory of Photoconductivity in Semiconductor Films', Phys. Rev., 104, pp. 1508-1518, 1956.

5. J.Y.W. Seto, 'The Electrical Properties of Polycrystalline Silicon Films', J. Appl. Phys., 46, pp. 5247-5254, 1975.

6. H.C. Card and E.S. Yang, 'Electronic Processes at Grain Boundaries in Polycrystalline Semiconductors Under Optical Illumination', IEEE Trans. Elec. Dev., ED-24, pp. 397-402, 1977.

7. C.H. Seager, G.E. Pike and D.S. Ginley, 'Direct Measurement of Electron Emission from Defect States at Silicon Grain Boundaries', Phys. Rev. Lett., 43, pp. 532-535, 1979.

8. C.H. Seager and G.E. Pike, 'Grain Boundary States and Varistor Behavior in Silicon Bicrystals', Appl. Phys. Lett., 35, pp. 709-711, 1979.

CHAPTER II

PHOTOVOLTAIC PROCESSES IN METAL SEMICRYSTALLINE SILICON SCHOTTKY BARRIERS AND IMPLICATIONS FOR GRATING SOLAR CELLS*

* The contents of this chapter have been published in Solid State Electronics Vol. 25, No. 9, pp. 917-923, 1982.

1. Introduction

Recent interest in reducing the cost of photovoltaic cells for terrestrial solar energy conversion has led to the introduction of a solar grade silicon material, which may be called semicrystalline silicon. Following the classification of Lindmayer and Putney[1], this semicrystalline material has the following characteristics: grain size of > 1 mm , high crystal order within grains with lifetime of > 1 μs , and non-conductive grain boundaries. While the cost of this material presently remains excessive for widespread use in photovoltaic power systems, one may reasonably expect the present research and development activity[2] to result in processes for its fabrication at substantially reduced costs in the near future.

At the same time many novel approaches to the simplification of the cell fabrication have also been reported. Of particular interest to us in the context of the studies described in the present paper are the Schottky barrier solar cell in its two geometries (i) the continuous metal case and (ii) the grating structure. These are both devices in which the dark currents are due primarily to majority carrier transport across the Schottky barrier and may be called majority carrier devices after the terminology of Shewchun et al[3]. An example of case (i) is the Cr-MIS devices studied most extensively by Anderson et al[4]. We have a particular interest here in (ii), the operation of which was first proposed and investigated theoretically by Green[5]. This device is potentially more efficient than (i) because

the dark current is proportional only to the area covered by metal, whereas the photocurrent is approximately proportional to the total area provided the metal coverage is low and the grid spacing is considerably smaller than the minority carrier diffusion length[6].

In contradistinction to devices (i) and (ii) there is another family of devices known as minority carrier or minMIS solar cells[7-10]. These devices incorporate an intentional insulating layer of tunneling thickness (1 to 2 nanometers) between the metal and semiconductor. Dark current in this case is due to minority carriers as in a PN junction, and these devices must not be regarded therefore as Schottky barriers. In fact, these minMIS cells operate in the minority carrier mode as a result of a pronounced inversion layer induced in the surface region. For a p-type semiconductor, these minority carrier devices can be referred to as induced PN junction devices and can be treated for practical purposes as N+P junction solar cells even though no diffused N region is present.

It must be realized however that in all devices (majority and minority cells alike) the photocurrent is due to the collection by the metal of minority carriers. Only the dominant mechanism for the dark currents differ.

Our attention in this chapter focusses primarily on the majority carrier solar cells, and cases (i) and (ii) discussed above are illustrated schematically in Fig. 1. While the minority carrier grating cells have been actively studied recently, to our knowledge the majority carrier grating cells have not been experimentally investigated. In the following sections, we describe the experimental depen-

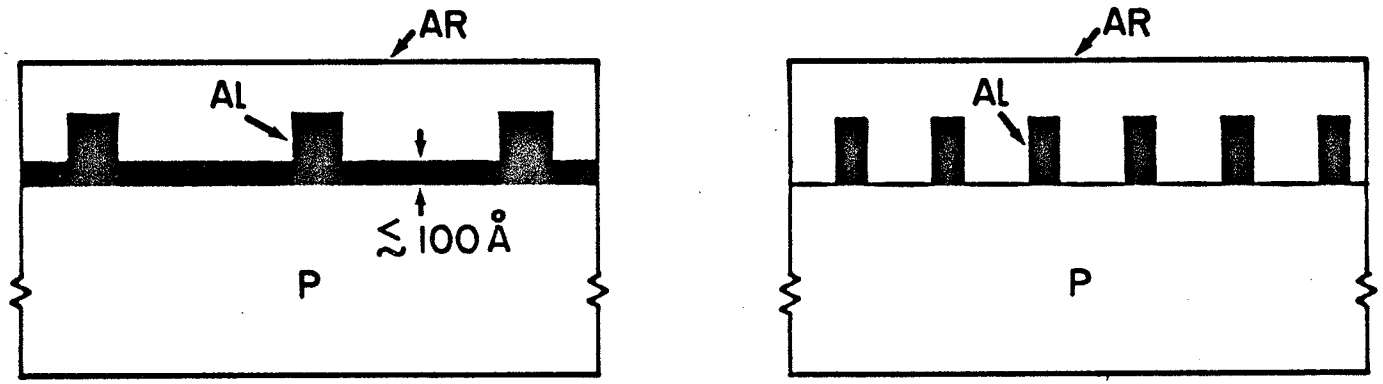

a) Continuous metal cell

b) Grating cell

Fig. 1 Schematic representation of a) continuous metal cell with thin aluminum and occasional thick strips to decrease series resistance, and b) grating cell with thick aluminum strips for edge collection only.

dence of the photovoltaic behaviour of metal-silicon Schottky barriers upon the metal (aluminum and aluminum-silver alloys), the form of the semiconductor (crystalline and semicrystalline Wacker 'Silso' silicon), the optical illumination intensity, and the geometrical position of the Schottky barrier contacts with respect to grain boundaries in the silicon. The purpose of this work is to show how the mechanisms contributing to the photovoltaic characteristics may be effectively separated, in order to understand the effects of recombination within the grains and at grain boundaries, shunt resistance of grain boundaries, and the voltage dependence of the photocurrent itself. We show experimentally that this last effect is in violation of the superposition principle of solar cells, in agreement with the warnings of earlier workers[11].

2. Experimental Procedures

The semiconductor material used in the present investigations was (1) crystalline silicon wafers of (111) orientation, 0.3 mm thickness, and p-type doping concentration of $N_a = 1.2 \times 10^{16}$ cm^{-3}, and (2) semicrystalline silicon wafers prepared by the 'Silso' casting process[14] and obtained from Wacker Siltronix Corp. These wafers were of thickness 0.45 mm, with a p-type doping concentration of $N_a = 3 \times 10^{15}$ cm^{-3}.

The silicon surfaces were cleaned in organic solvents and etched in a CP4A solution (3-70% nitric acid/1-acetic acid/1-50% hydrofluoric acid) for ≃ 3 mins. This surface treatment has been found to result in Schottky barriers with near-ideal behaviour with respect to interface-related phenomena.

The metal electrodes were evaporated from tungsten filaments at a base pressure of $\simeq 10^{-6}$ torr. In the case of Ag/Al alloy electrodes, a novel co-evaporation technique was developed in which the tungsten filaments for the Ag and Al were connected in parallel but were of different lengths to control the relative evaporation rates of these two metals. The composition of the alloy electrodes was controlled by the proportions of metal on the separate filaments, which were evaporated to completion.

If the filament lengths, and hence the evaporation temperatures, are selected such that both evaporations are completed simultaneously, then, as a first order approximation, the composition of the deposited alloy will be directly related to the amounts of evaporants used. A shutter was used to shield the evaporation sources until both filaments had reached their final temperatures so that electrodes of uniform composition might be realized.

No quantitative data were obtained for the thickness of the 2mm diameter electrodes because in the current investigation it was only necessary to deposit suitably large amounts of the evaporants to ensure that only edge collection would take place in the resulting Schottky barriers.

3. Results

Typical experimental current-voltage characteristics obtained under dark conditions for Schottky barriers of aluminum, silver, and aluminum/silver alloys on crystalline silicon are shown in Fig. 2. The corresponding results for semicrystalline Wacker silicon devices are shown in Fig. 3. A silver-only Schottky barrier (on p-type material) exhibited near-ohmic characteristics. In the case of aluminum-semicrystalline silicon contacts, a variety of characteristics was obtained depending upon the position of the electrode with respect to grain boundaries in the material. Representative samples of this behaviour are shown in Fig. 4. As for the optically-illuminated case, the dependences of the (photovoltaic) current-voltage characteristics on the intensity of the illumination are shown in Fig. 5. For convenience, a summary of representative data obtained from the devices studied is given in Table 1.

4. Discussion: Dark Measurements

The dark current-voltage characteristics of the previous section have been interpreted as arising primarily from the thermionic emission of majority carriers (holes) from the semiconductor into the metal under forward bias conditions. This mechanism is described by[12]

$$I_1 = aA^* T^2 \exp(-\phi_b/V_T) \left[\exp(V/n_1 V_T) - 1\right] \qquad (1)$$

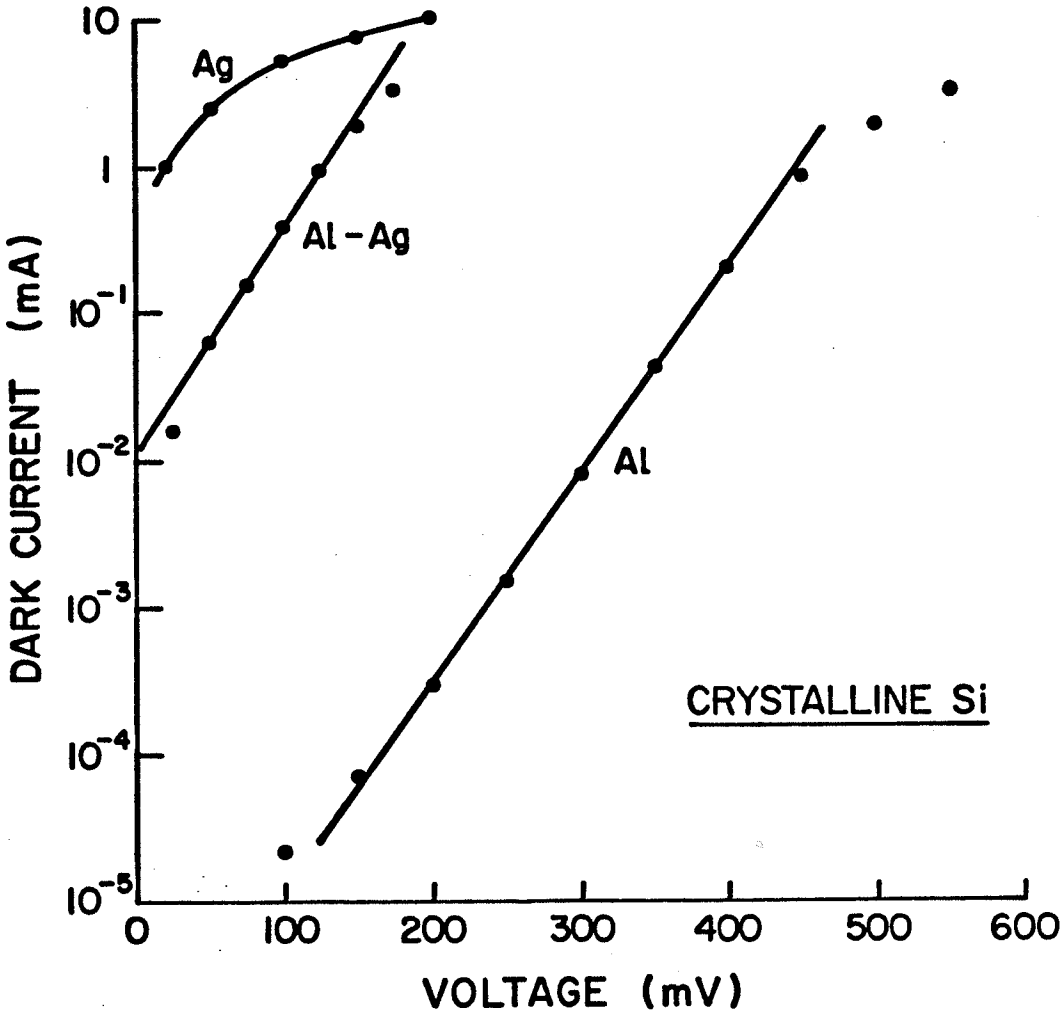

Fig. 2 Dark I-V characteristics for aluminum, aluminum/silver, and silver electrodes on crystalline silicon.

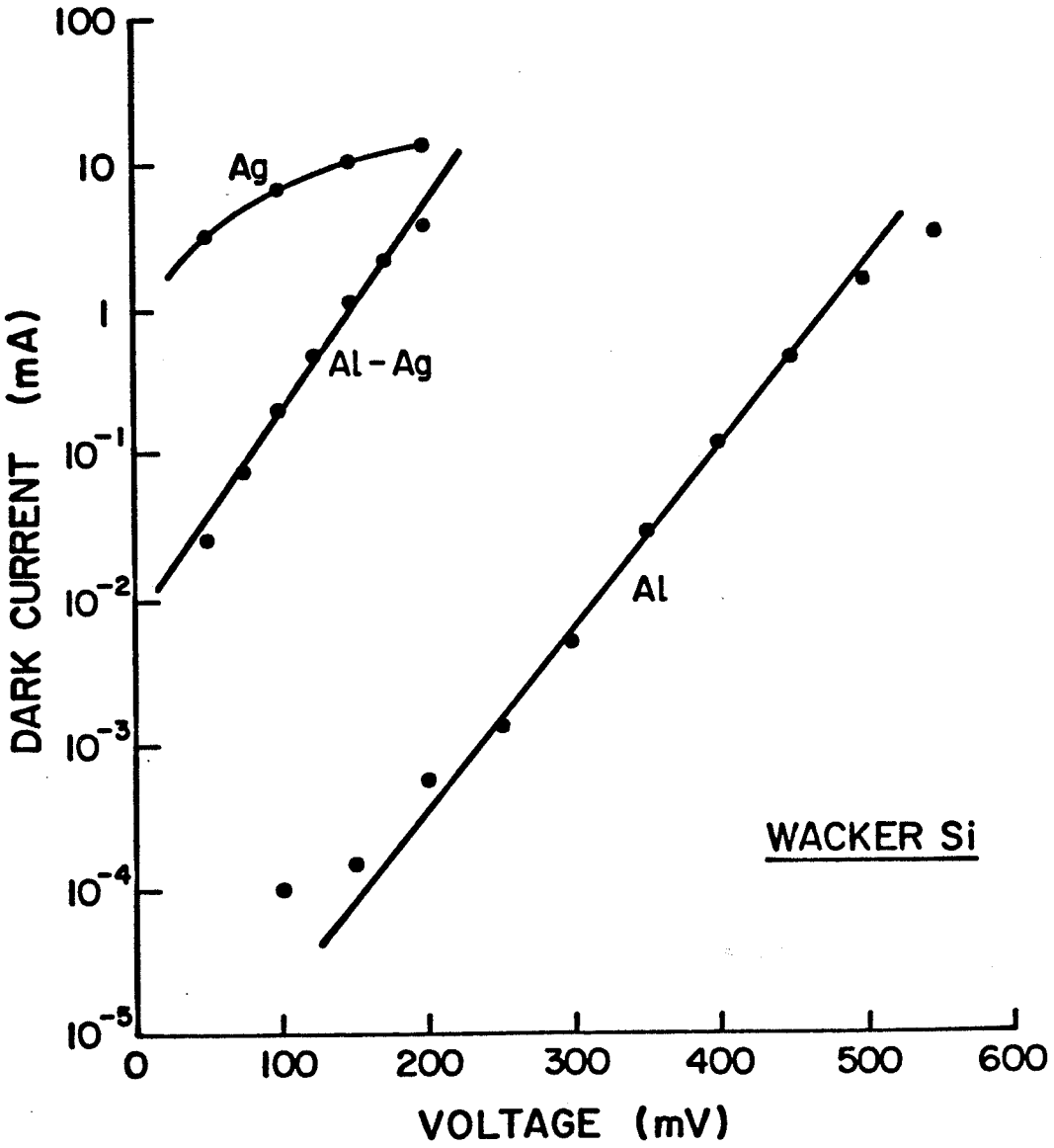

Fig. 3 Dark I-V characteristics for aluminum, aluminum/silver, and silver electrodes on semicrystalline (Wacker) silicon.

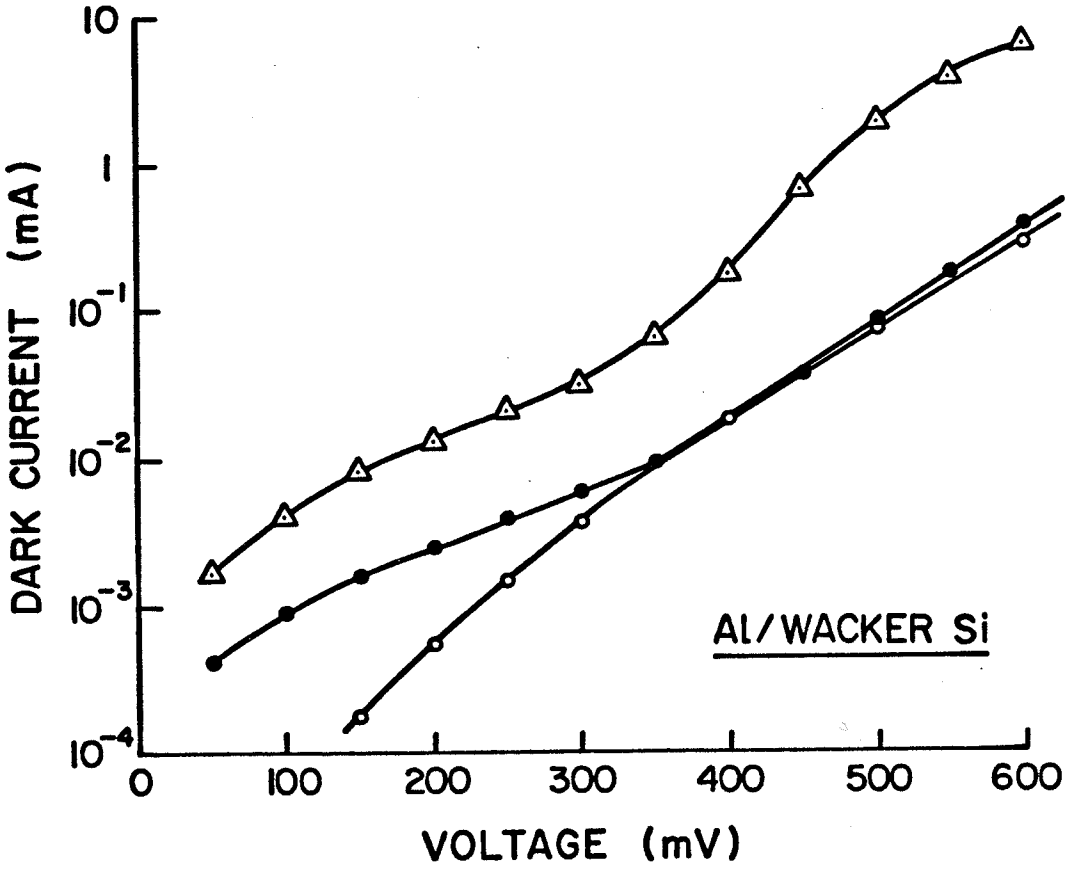

Fig. 4 Examples of dark I-V characteristics for aluminum-Wacker silicon contacts encompassing grain boundaries.

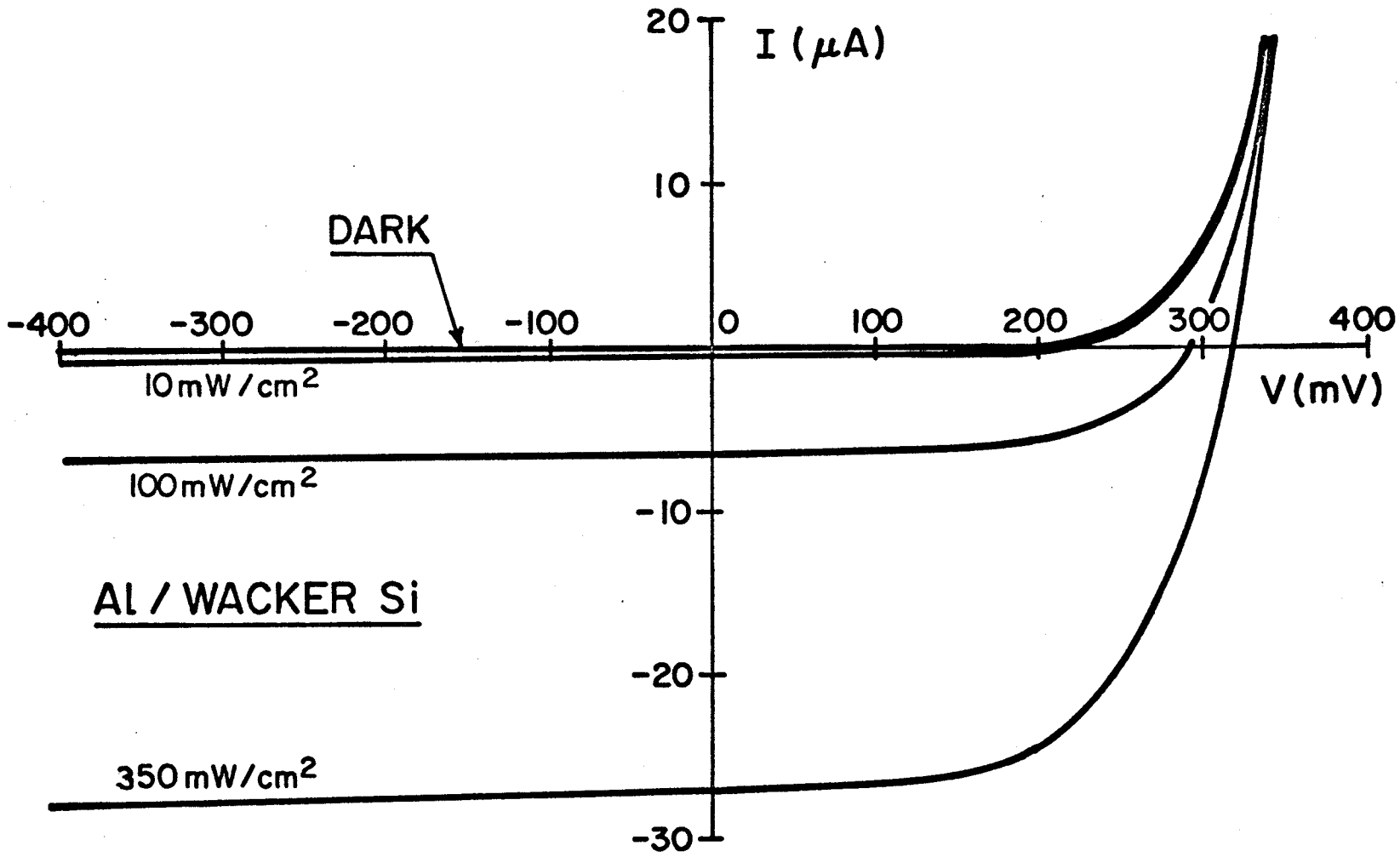

Fig. 5 An example of illuminated I-V characteristics for aluminum semicrystalline silicon.

TABLE 1 - Summary of Data

Sample	Metal	Si type	ϕ_b (mV)	n	N_t (cm^{-3})	R_{sh} (kΩ)
12 3,4	Aℓ	Wacker	732	2.68		> 3000*
12 5,6	Aℓ	Wacker	740	2.50	Wacker	250
12 5,5	Aℓ	Wacker	934	1.21	2.8×10^{15}	> 3000*
12 4,4	Aℓ	Wacker	936	1.67		130
16 3,6	Aℓ+Ag	Wacker	609	1.08		96
16 II	Aℓ+Ag	Cryst	594	1.08	Crystalline	46
19 2	Aℓ	Cryst	933	1.18	6.9×10^{13}	720

* no accurate measurement possible; lower limit only.

where I_1 is the thermionic emission current, a is the contact area, A^* the modified Richardson constant $\simeq 30\ Acm^{-2}K^{-2}$ for Schottky barriers on p-type silicon[13], ϕ_b is the Schottky barrier height, V the applied forward voltage (positive on semiconductor), n_1 the ideality factor, and $V_T = kT/q$.

There is also a component of the dark current due to recombination in the space-charge region[12]

$$I_2 = \frac{aqW\sigma v_{th}}{2} N_t n_i [\exp(V/n_2 V_T) - 1] \qquad (2)$$

where W is the width of the space-charge region, v_{th} is the thermal velocity of free carriers, σ and N_t are the capture cross-section and volume density of recombination centers (in the space-charge region). Here we assume σ and v_{th} for electrons and holes to be equal.

In addition, there is a contribution to the dark current which arises from the injection of minority carriers (electrons) into the semiconductor from the metal under forward bias[12]

$$I_3 = \frac{a(qkT)^{\frac{1}{2}} \mu_n^{\frac{1}{2}} n_i^2}{\tau_n^{\frac{1}{2}} N_a} [\exp(V/n_3 V_T) - 1] \qquad (3)$$

where μ_n is the electron mobility, n_i is the intrinsic carrier concentration, N_a is the doping concentration and τ_n is the electron lifetime. According to a simple model[13], $\tau_n = (\sigma v_{th} N_t)^{-1}$ with N_t the density of recombination centers in the neutral region in this case.

Finally, in the presence of a shunt resistance R_{sh}, we expect a fourth contribution to the dark current

$$I_4 = V/R_{sh} \qquad (4)$$

Strictly speaking the voltage V in Eqns (1) to (3) refers to the junction voltage which may differ from the applied voltage if a significant series resistance is present. We have determined however, that for all the devices reported in this paper, this series resistance is completely negligible. This is a consequence of the relatively small areas of our Schottky barriers and is an advantage in removing one source of non-ideality from both the dark and optically-illuminated characteristics.

We have also been able to eliminate the component I_3 from the analysis, since for the range of ϕ_b encountered in the present devices, I_1 is always larger by at least two orders of magnitude. In order to justify this approximation, it is necessary to have a representative value for τ_n. This we have obtained for the Wacker material from the work of Koliwad and Daud[14] to be 300 ns. In the case of crystalline silicon, τ_n will be larger still, which further reduces I_3 in that material. The other parameters in Eqn. (3) are

taken to be their crystalline values, which are known with a much better degree of precision than is τ_n .

We have shown in Figs. 2 and 3 the experimental data points for our p-type crystalline and Wacker silicon for Al, Al/Ag and Ag contacts. In all cases these devices are expected to behave as majority carrier (Schottky barrier) solar cells with $I_1 >> I_3$. It should be noted however that by introducing an intentional oxide layer in the case of aluminum-p-type silicon, the term I_1 may be greatly suppressed due to an attendant increase in ϕ_b and a reduction in the effective Richardson constant by a factor of the oxide tunneling probability for holes[15,16]. In this case I_3 exceeds I_1 and a minority carrier solar cell is obtained[10], but this oxide layer was not introduced in the present studies.

From the results of Figs. 2 and 3 for the dark currents of metal-crystalline silicon and metal-semicrystalline silicon contacts we make the following observations:

1. The Schottky barrier height (average value) decreases with the concentration of silver in the electrode from $\phi_b \simeq 840$ mV for pure aluminum to $\phi_b \simeq 400$ mV for pure silver.
2. Near-ideal behaviour is observed for both crystalline and semicrystalline materials with Ag and Ag/Al alloys which are of lower barrier height than Al . No difference in ϕ_b is observed for crystalline and semicrystalline material within experimental error. For these devices I_1 dominates and $n_1 \simeq 1$.
3. Near-ideal behaviour is observed for Al on crystalline silicon with a noticeable contribution from space-charge recombination I_2.

This contribution is identifiable here because the large ϕ_b of Al/Si contacts reduces the saturation current of I_1 below that of I_2.

4. For Al on semicrystalline silicon, a variety of behaviour is observed depending on the position of the electrode with respect to grain boundaries. For contacts centered within a grain, behaviour similar to (3) for crystalline silicon is obtained. For contacts spanning more than one grain, non-ideal behaviour is observed, with major contributions from space-charge recombination I_2 and also in some cases from shunt resistance I_4. In those cases where I_4 is important, n in the total voltage dependence may be much greater than 2, otherwise $1 < n < 2$.

Several conclusions and implications can be drawn from the dark characteristics and the above observations.

(i) The non-idealities observed for the contacts of large barrier height result from I_2 and I_4, components which are also present in the devices with low ϕ_b but are swamped by the much larger component I_1. These non-idealities do <u>not</u> arise from metal-silicon interface effects since if they did, these interface effects would contribute for all values of ϕ_b. In fact, a detailed analysis of interface effects shows that any non-idealities introduced by oxide layers and interface states will be most apparent for devices with low ϕ_b.

(ii) The pre-exponential factor in the component I_2 for Al/semicrystalline silicon is one to two orders of magnitude larger than that for Al/crystalline silicon contacts. This

implies that the density of recombination centers is 10 to 100 times larger in semicrystalline silicon. It is not clear whether this results primarily from grain boundary defects or from increased dislocation densities within the grain, but both effects are present.

(iii) Shunt resistances appear to be the result of grain boundaries which completely penetrate the silicon to the back ohmic contact. The grain boundaries in the Wacker material are known to be primarily columnar[17]. The effects of these occasional shunt resistances are only observable because of the small electrode areas employed in this work. For large area solar cells, the active junction area will be orders of magnitude larger, so that shunt resistances in the range of 130 kΩ to >3 MΩ as observed here will not adversely affect device efficiency.

5. Discussion: Optically-Illuminated Measurements

The current voltage characteristics under optical illumination can be described by the expression

$$I = I_1 + I_2 + I_3 + I_4 + I_{ph} \qquad (5)$$

where the sign of the last term is negative since the photocurrent I_{ph} opposes currents I_1 to I_4. For our devices I_3 may be neglected. For increased optical illumination intensity $|I_{ph}|$ is increased but according to the superposition principle of solar cells[11] the other

terms in Eqn. (5) should be unaffected. In that case

$$I \simeq I_{dark} + I_{ph} \tag{6}$$

where I_{ph} is dependent on illumination intensity but independent of voltage.

In Fig. 6 we plot the experimental results for $I_{dark} - I$ as a function of voltage for several illumination levels. The same qualitative dependence is observed for all devices studied. We note that $I_{dark} - I$ is not constant but decreases with forward voltage V. This is in violation of the superposition principle, Eqn. (6). This violation is anticipated in the work of Ref. 11 and has previously been observed for the crystalline case by Panayotatos and Card[18]. In determining the origin of this violation and in understanding the edge-collected electron photocurrent, the following observations are important:

1. The decrease in $I_{dark} - I$ with increasing forward bias voltage V is observed to some extent in all devices.
2. The percentage decrease in $I_{dark} - I$ for a given V increases with the optical illumination intensity.
3. This effect (increased violation of superposition principle with V) is more pronounced in the case of semicrystalline silicon than in the case of crystalline silicon.
4. The effect is larger for lower Schottky barrier height ϕ_b.

These observations are consistent with the hypothesis that the reduction in $I_{dark} - I$ with V is due to a reduction in the flux of (photogenerated) electrons collected by the metal at larger V due

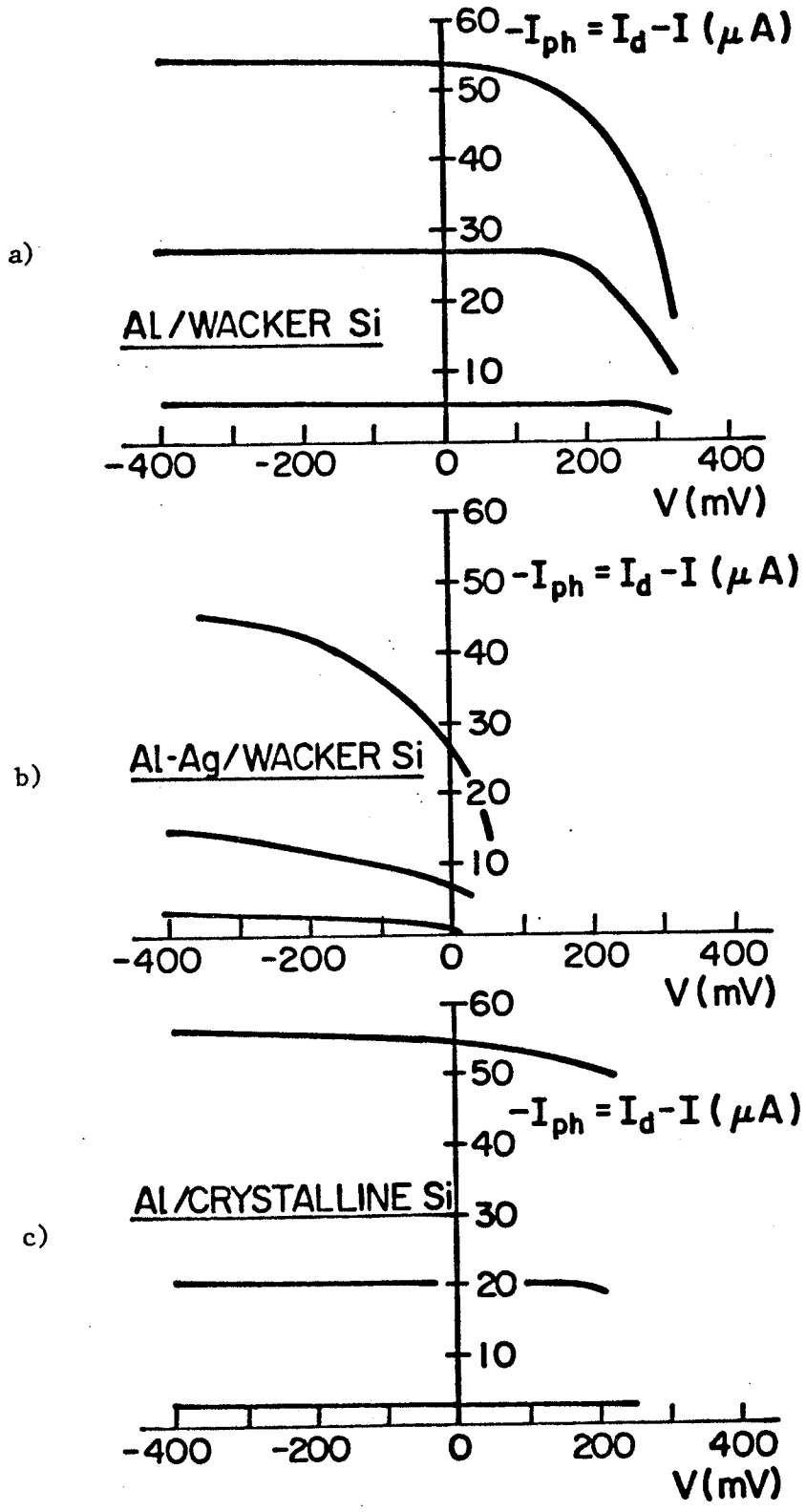

Fig. 6 Voltage dependence of photocurrent for a) Al on semicrystalline Si , b) Al/Ag on semicrystalline Si , and c) Al on crystalline Si .

to enhanced recombination in that part of the space-charge region through which they pass during collection. This portion of the space-charge region is at the periphery of the metal electrodes. For the majority-carrier grating solar cells, the area occupied by the collecting contact is small compared to the area in which the photogenerated electrons, collected by that contact, are produced. This means that the photocurrent densities (current/unit area) are orders of magnitude larger than the dark current densities. This is unlike the cases of continuous metal majority-carrier cells or minority carrier grating structures, for which dark and photocurrent densities are equal at the open-circuit voltage. The violation of the superposition principle is thus expected to be greatest in the majority carrier grating structures, since an increased photocurrent density implies an increased electron concentration (and consequently enhanced recombination) in the space-charge region[19]. This is expected to seriously compromise the efficiency of these devices.

Our conviction that increased space-charge recombination is responsible for the departures from the superposition principle is based primarily upon observations 2 and 3 above and the voltage dependence of I under optical illumination. As the illumination intensity increases, the photocurrent density increases and with it the minority carrier (electron) concentration in the collecting space-charge region. This increases the recombination current I_2 in Eqn. (2) above its dark value for a given voltage V across this region. A quasi-Fermi level separation $E_{fn} - E_{fp}$ exists in the space-charge region even for $V = 0$ so long as an appreciable photocurrent is being collected. This

appears as an enhanced pre-exponential factor in Eqn. (2). With increases in V, I_2 increases with a voltage dependence described by $n_2 \simeq 2$, as expected on the basis of the Sah-Noyce-Shockley treatment[20].

The decrease in $I_{dark} - I$ may actually be interpreted in two ways with identical results. One may view I_2 in Eqn. (5) as an expression of the dark space-charge recombination current, in which case I_{ph} is the collected photocurrent, which decreases with V. Alternatively, and more conveniently, I_{ph} may be taken to be the maximum (short-circuit) photocurrent for all V so that I_{ph} is a constant in Eqn. (5), in which case I_2 is now an expression of the space-charge recombination under optical illumination. We can in this case write

$$I_2 \simeq \sigma N_t v_{th} W \frac{aqn_i \exp(\Delta E_{fo}/n_2 kT)}{2} \left[\exp(V/n_2 V_T)\right] \qquad (7)$$

for the optically-illuminated case. $I_2(0)$ is the space-charge recombination for $V = 0$ which is non-zero in the presence of the (short-circuit) photocurrent. This term is already included in the measured value of short-circuit current.

The pre-exponential factor in I_2 has been modified from the dark case by replacing n_i in Eqn. (2) by $n_i \exp(\Delta E_{fo}/n_2 kT)$ in Eqn. (7). In this expression $\Delta E_{fo} = E_{fn} - E_{fp}$ is the splitting of the quasi-Fermi levels for $V = 0$ which increases with illumination intensity from a dark value of zero. Strictly, ΔE_{fo} is the value of this splitting at the position in the space-charge region where the

recombination rate is a maximum ($n \simeq p$), as clearly explained for the dark case by Grove[21]. The illumination has a similar effect as an applied voltage, which also splits the Fermi levels by an amount $E_f = qV$. One can regard the effect of the illumination as a built-in 'recombination potential' of magnitude $\Delta E_{fo}/q$ which drives the recombination process even for $V = 0$. As V increases, the Fermi level splitting increases to $\Delta E_f \simeq \Delta E_{fo} + qV$ and the only effect of ΔE_{fo} is therefore to provide a constant increase in the pre-exponential factor of I_2 in Eqn. (7).

The increases in I_2 with optical illumination intensity (due to increases in the recombination potential $\Delta E_{fo}/q$) are also more pronounced with semicrystalline silicon than with crystalline silicon. This is due to the increased density of recombination centers in semicrystalline silicon, due in part to the presence of grain boundaries and in part to increased dislocation density within the grains. This increases N_t in Equation (7) for semicrystalline silicon, as discussed in an earlier section.

Figure 7 shows the voltage dependence of $I - I_{sc}$ for various illumination levels. The space-charge recombination current for $V = 0$, $I_2(0)$, is found by extrapolation. Its illumination dependence is expressed through the quasi-Fermi level splitting ΔE_{fo} in Eqn. (7).

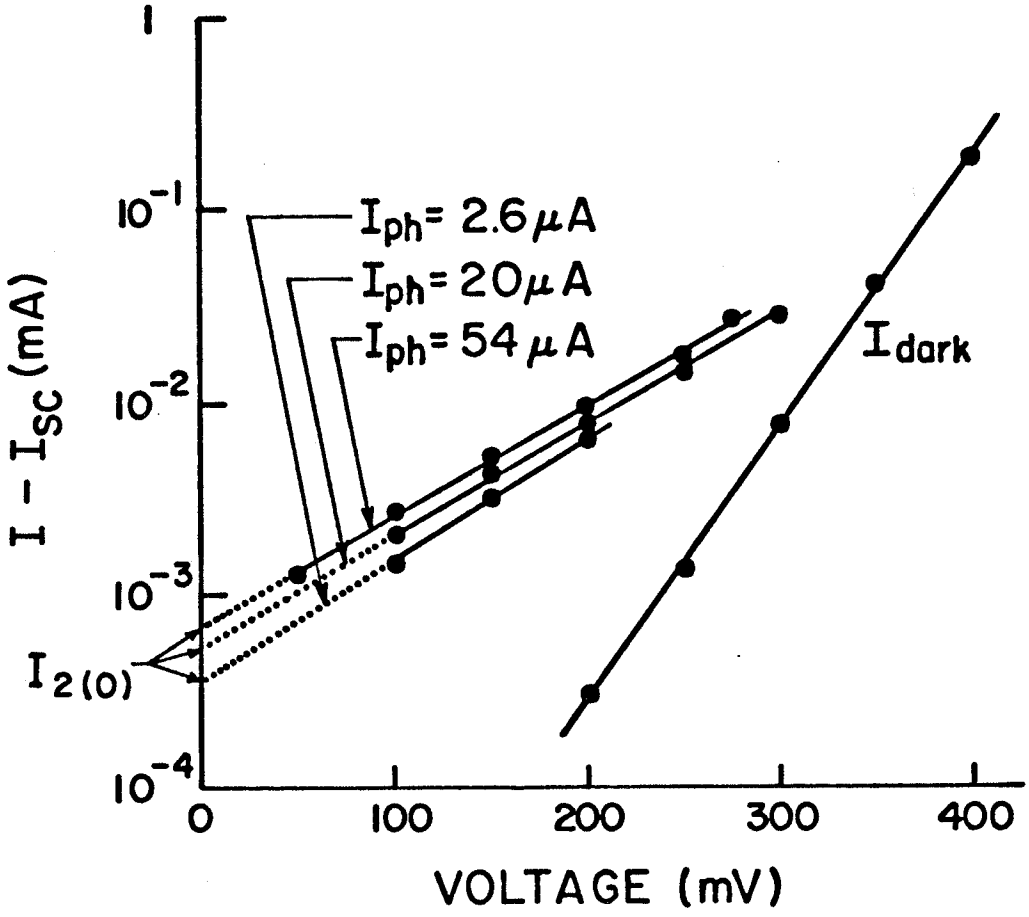

Fig. 7 Voltage dependence of $I - I_{sc}$ for various illumination levels in the case of aluminum electrodes on crystalline silicon. The dark I-V characteristic ($I_{sc} = 0$) is included for comparison.

6. Conclusions

On the basis of the experimental observations reported in this study, and in view of the above discussions of these observations we wish to advance the following conclusions:

1. The majority-carrier grating solar cells depend for their improved efficiency, over that of continuous metal Schottky barrier solar cells, upon the employment of small contact area/active area ratios. We have shown here that this brings with it the problem of very large photocurrent densities at the contact, and a resultant bottleneck to the collection of the photogenerated minority carriers due to enhanced space-charge recombination.
2. Space-charge recombination under optical illumination can be regarded as the composite effect of a built-in voltage, resulting from the splitting ΔE_{fo} of the quasi-Fermi levels under short-circuit conditions, and the increase in ΔE_f due to the photovoltage V.
3. The superposition principle [11] is not satisfied in majority-carrier grating solar cells, even for crystalline silicon.
4. Semicrystalline silicon is only marginally inferior to crystalline silicon as a material for large-area solar cells, in which the effects of shunt resistance will be negligible.
5. Provided reasonable care is exercised in the surface preparation of semicrystalline silicon all of the non-idealities observed in both dark and optically illuminated Schottky barriers to this material can be explained in terms of an extended SNS [20] description of space-charge recombination currents, and the inclusion of shunt resistances in occasional localized regions of the material.

References

1. J. Lindmayer and Z.C. Putney, Proc. of 14th IEEE Photovoltaic Spec. Conf., San Diego, CA, IEEE Press: New York, pp. 208-213, Jan. 7-10, 1980.

2. T. Surek et al, Proc. 15th IEEE Photovoltaic Spec. Conf., Kissimmee, Fl., IEEE Press: New York, pp. 1251-1260, 1981.

3. M.A. Green, F.D. King and J. Shewchun, Solid State Electronics, 17, pp. 551-561 and 563-572, 1974.

4. W.A. Anderson, J.K. Kim and A.E. Delahoy, IEEE Trans. on Electron Dev., ED-24, pp. 453-457, 1977.

5. M.A. Green, Appl. Phys. Lett, 27, pp. 287-288, 1975.

6. A.K. Kong and M.A. Green, J. Appl. Phys., 49, pp. 473-442, 1978.

7. R.B. Godfrey and M.A. Green, IEEE Trans. on Electron Dev., ED-27, pp. 737-745, 1980.

8. N.G. Tarr, D.L. Pulfrey and P.A. Iles, Appl. Phys. Lett., 35, pp. 258-260, 1979.

9. R.E. Thomas, C.E. Norman and R.B. North, Proc. 14th IEEE Photovoltaic Spec. Conf., San Diego, CA, IEEE Press: New York, pp. 1350-1353, 1980.

10. K.K. Ng and H.C. Card, IEEE Trans. on Electron Dev., ED-27, pp. 716-724, 1980.

11. F.A. Lindholm, J.G. Fossum and E.L. Burgess, IEEE Trans. on Electron Dev., ED-26, pp. 165-171, 1979.

12. E.H. Rhoderick, Metal-Semiconductor Contacts, Clarendon Press: Oxford, 1978.

13. S.M. Sze, Physics of Semiconductor Devices, 2nd Edition, John Wiley and Sons: New York, 1981.

14. K.M. Koliwad and T. Daud, Proc. 14th IEEE Photovoltaic Spec. Conf., San Diego, CA, IEEE Press: New York, pp. 1204-1208, 1980.

15. H.C. Card, Solid St. Electron., 20, pp. 971-976, 1977.

16. K.K. Ng and H.C. Card, J. Appl. Phys., 51, pp. 2153-2157, 1980.

17. K. Roy, K.D. Rasch and H. Fischer, Proc. 14th IEEE Photovoltaic Spec. Conf., San Diego, CA, IEEE Press: New York, pp. 897-901, 1980.

18. P. Panayotatos and H.C. Card, IEE Proc. I. Solid St. and Electron Dev., 127, pp. 308-311, 1980.

19. P. Panayotatos and H.C. Card, Solid St. Electron., 23, pp. 41-47, 1980.

20. C.T. Sah, R.N. Noyce and W. Shockley, Proc. IRE, 45, pp. 1228-1235, 1957.

21. A.S. Grove, Physics and Technology of Semiconductor Devices, John Wiley and Sons: New York, 1967.

CHAPTER III

THERMIONIC-FIELD EMISSION FROM INTERFACE STATES AT GRAIN BOUNDARIES IN SILICON*

* The contents of this chapter have been accepted for publication in Journal of Applied Physics.

1. Introduction

Interface states at grain boundaries in semiconductors have been studied recently by several workers, for example Refs. 1-7. These states are known to affect the transport of majority carriers across the grain boundaries, and also to act as recombination centers for excess minority carriers. Their study is of practical importance for the understanding of the carrier mobility in polycrystalline semiconductors, and for the characterization of optoelectronic and photovoltaic phenomena in these materials.

The capture and emission of electrons and holes by the grain boundary interface states is normally treated using the kinetic model, rate equations, and occupancy statistics developed by Shockley and Read[8] and by Hall.[9] This phenomenology was originally developed for isolated (point) defects in semiconductors, and is not always appropriate for the treatment of localized states at interfaces. For example, in the present chapter we deal with electrically-active grain boundaries (GB) in semiconductors in which, for n-type material, electrons are transferred from the surrounding region to grain boundary interface states, leaving a positively charged donor region adjacent to a negative GB plane.

The space-charge regions present large electric fields normal to the grain boundary, which assist the emission of majority carriers from the interface states. For example, in an n-type semiconductor, electrons trapped in grain-boundary interface states need not be thermally excited to the conduction band at E_c to escape. They may be thermally excited to energies below E_c at which they can tunnel through the potential barrier provided by the forbidden energy region in the

presence of an electric field; this process is thermionic-field emission (TFE) of electrons from interface states.

We illustrate in this chapter that a proper description of carrier transport across grain boundaries in semiconductors, of transient capacitance measurements of grain boundaries under non-equilibrium conditions, or indeed of any experimental situation in which interface generation-recombination processes are of importance to the phenomenon under study, requires that thermionic-field emission processes be included. Under special circumstances which are defined quantitatively later in this chapter, the simple thermal emission of the SRH Model[8,9] will also serve for interface problems, but only for low electric fields normal to the grain boundary and at high temperatures.

2. Theory

In Fig. 1 is shown the energy-band diagram in the region of a grain boundary (GB) in an n-type semiconductor. Also shown are interface states, at an energy E_t, at the grain boundary. These states are associated with grossly distorted (bent and/or stretched) bonds between silicon atoms at defects on the grain-boundary plane. We assume an acceptorlike character for these states, on the basis of empirical evidence from earlier studies (1,6,7), so that each state which is occupied by an electron contributes one elementary negative charge $-q$. If the surface density of these states is $N_{is}(cm^{-2})$ and the occupancy is f_{is} where $0 < f_{is} < 1$, the charge per unit area on the grain boundary is represented by a delta function of strength $Q_{is} = -q\, N_{is}\, f_{is}\ (Ccm^{-2})$. In the depletion approximation, the width of the space-charge region is $W = N_{is}\, f_{is}/2\, N_d$ for a uniform donor distribution

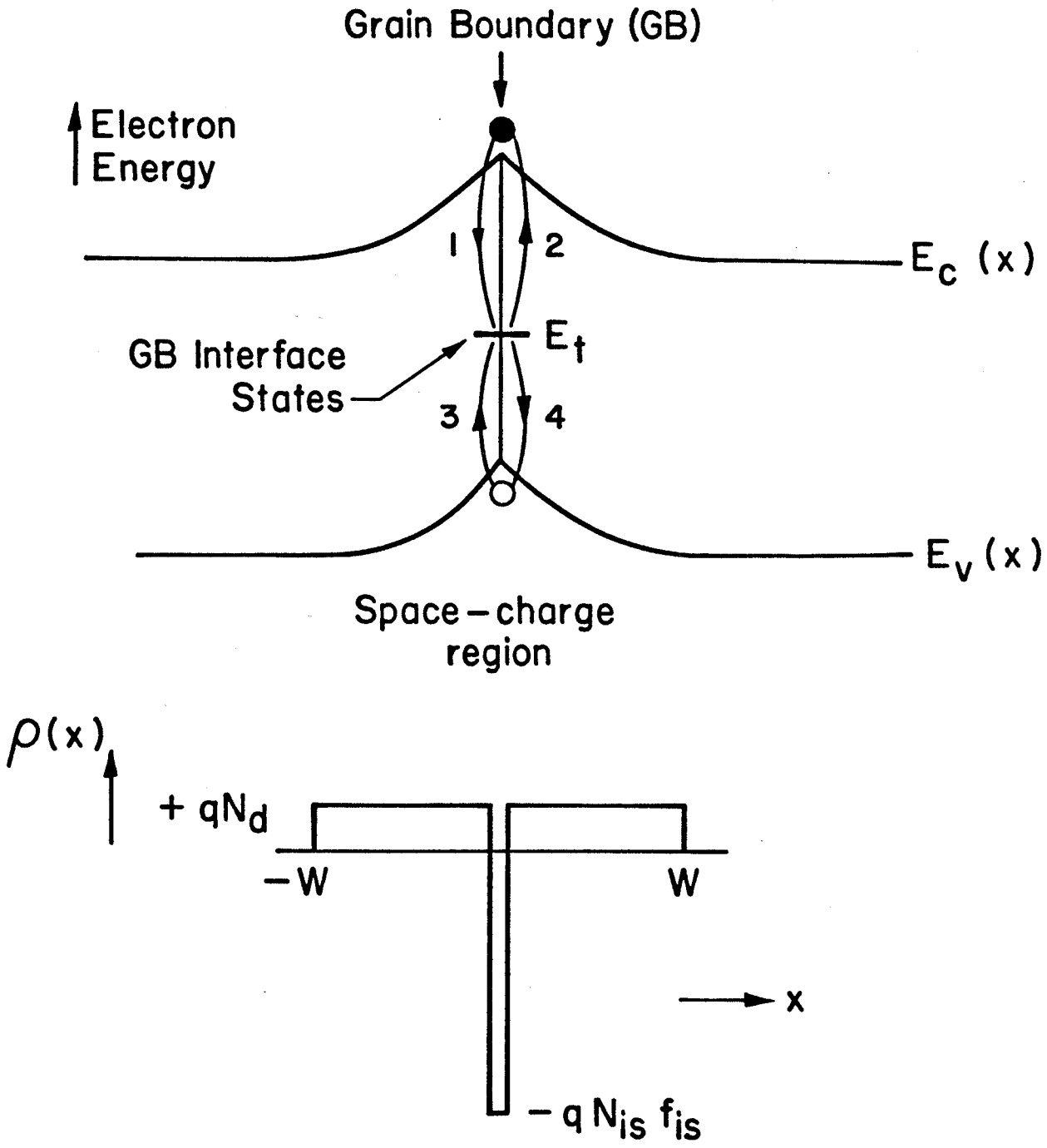

Fig. 1 Energy-band diagram in vicinity of grain boundary showing charge exchange between interface states of energy E_t and the conduction and valence bands. 1,2,3, and 4 correspond to electron capture, electron emission, hole capture and hole emission respectively. Lower figure shows charge distribution.

$N_d(cm^{-3})$.

Let us consider the mechanisms by which the GB interface states can exchange charge with the conduction and valence bands in the semiconductor. We begin by employing the well-known rate equations used by Hall[9] and by Shockley and Read[8] for localized (trap) states in semiconductors, which are expected to apply in some circumstances to the GB interface states. These state that the net capture rate of electrons by interface states of energy E_t and density N_{is} is given by

$$U_{cn} = N_{is}\,\sigma_n\,v_n[(1-f_{is})n - f_{is}\,n_1] \qquad (1)$$

where U_{cn} has units $cm^{-2}s^{-1}$, n is the electron concentration (cm^{-3}) at the grain boundary, σ_n is the capture cross-section (cm^2) of the interface states for electrons, v_n is the electron thermal velocity ($cm\ s^{-1}$), and n_1 (cm^{-3}) is given by

$$n_1 = N_c \exp\left(\frac{E_t - E_c}{kT}\right) \qquad (2)$$

with N_c the effective density of states in the conduction band and E_c the energy of the conduction band edge at the grain boundary. Similarly the net capture rate of holes is given by

$$U_{cp} = N_{is}\,\sigma_p\,v_p[f_{is}\,p - (1-f_{is})p_1] \qquad (3)$$

with

$$p_1 = N_v \exp\left(\frac{E_v - E_t}{kT}\right) \qquad (4)$$

where σ_p is the capture cross-section of the interface states for holes, p is the hole concentration at the grain boundary, v_p is the thermal velocity of holes, N_v is the effective density of states in the valence band, and E_v is the energy of the valence band edge at the grain boundary.

In Eqns. (1) and (3), f_{is} is the occupation function of the interface states, which is the fraction of these states that is occupied by electrons. Under steady-state conditions the net capture rates of holes and electrons are equal, and by equating Eqns. (1) and (3) we find

$$f_{is} = \frac{n\,\sigma_n + p_1\,\sigma_p}{\sigma_n(n+n_1) + \sigma_p(p+p_1)} \qquad (5)$$

The first term on the RHS of Eqns. (1) and (3) corresponds to capture of electrons and holes, processes 1 and 3 in Fig. 1, respectively. The second term on the RHS of these equations corresponds to emission of electrons and holes respectively by thermal processes (2 and 4 in Fig. 1).

In addition to charge exchange with the conduction and valence bands by thermal processes (Eqns. (1) and (3)), the interface states may emit charge to these bands by quantum-mechanical tunneling processes. For example, in Fig. 2, electrons trapped in the GB interface states may tunnel to the conduction band through the potential barrier of the semiconductor. A similar analysis applies to hole emission from GB interface states in p-type semiconductors. In order

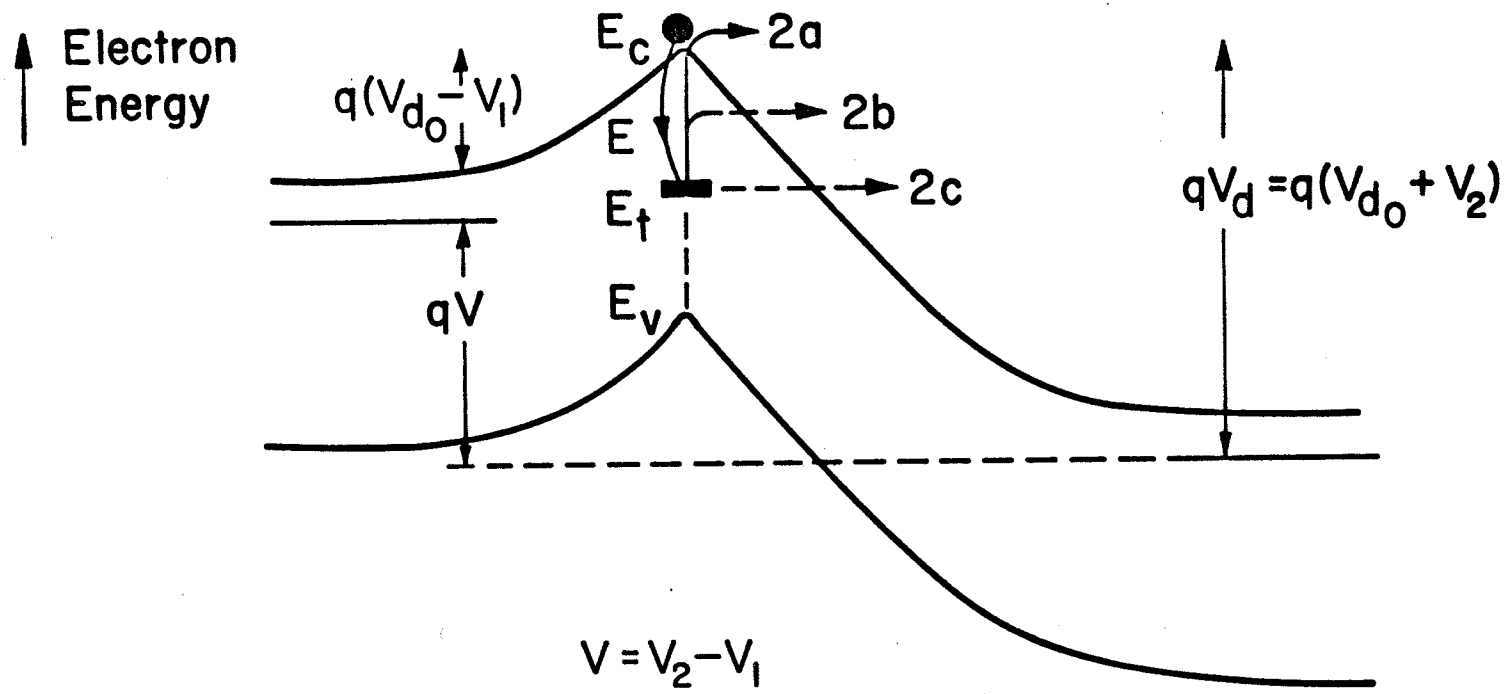

Fig. 2 Grain boundary under applied bias voltage V . V_1 and V_2 are voltages developed on forward and reverse-biased sides of the grain boundary. Process 1 is electron capture. Processes 2a, 2b, 2c correspond to thermal emission, thermionic-field emission, and pure field emission of electrons from the GB interface states, respectively.

to deal with tunneling in a general way, we consider all contributions due to thermionic-field emission at energies from E_t to E_c in Fig. 2. Some aspects of the present treatment are reminiscent of the approach of Freeman and Dahlke[10] to interface states in tunnel MIS devices. For tunneling transitions at the energy E_t, the net rate of electron transfer to the conduction band may be written[10]

$$U = \frac{N_{is}\,(f_{is}-f_n)}{\tau_t} \tag{6}$$

where f_n is the occupancy of the conduction band states of energy E, which under the non-equilibrium cases of interest in this work may be taken as zero without loss of accuracy, and τ_t is the time constant for tunneling given by[11,12]

$$\tau_t = \tau_o \exp\left(\frac{2(E_c-E_t)^{3/2}}{3\,E_{oo}\,V_d^{1/2}}\right) \tag{7}$$

based upon a WKB approximation for tunneling through a triangular barrier, in which τ_o is only weakly dependent upon energy E_t [12], V_d is the diffusion potential at the grain boundary (Fig. 2), E_c and E_t are epxressed in eV, and E_{oo} is given by

$$E_{oo} = \frac{\hbar}{2}\left(\frac{N_d}{m^* \varepsilon_s}\right)^{1/2} \tag{8}$$

where $\hbar(=h/2\pi)$ is expressed in Js, N_d is the donor doping concentra-

tion in the silicon (m^{-3}), m^* is the effective mass (kg) of the tunneling carriers, and ε_s is the permittivity of the silicon (F/m). E_{oo} is a notation introduced by Padovani and Stratton[11] for field emission in Schottky barriers.

Thermionic-field emission of electrons may be regarded as a two-step process in which electrons are excited thermally to virtual states above E_t and subsequently tunnel through a reduced barrier (process 2b in Fig. 2). The contribution from an incremental range dE about an energy E (between E_t and E_c at the GB) is given by

$$U(E)dE = \frac{N_{is} f_{is}}{\tau_t(E)} \frac{1}{kT} \exp\left(\frac{E_t - E}{kT}\right) dE \qquad (9)$$

where we have employed the normalized probability distribution for the occupation of the virtual states with $E > E_t$

$$n(E) = \frac{1}{kT} \exp\left(\frac{E_t - E}{kT}\right) \qquad (10)$$

for which

$$\int_{E_t}^{\infty} n(E)\, dE = 1 \qquad (11)$$

as required.

Expression (9) also applies to the pure thermal emission of electrons provided that the tunneling exponential in Eqn. (7) is taken to be unity for $E > E_c$ and infinity for $E < E_c$, so that the limits of integration for the total thermal emmision are E_c and infinity, rather

than E_t and E_c, as for the thermionic field emission component.

Thus, we obtain

$$U_{(\text{no tunneling})} = \int_{E_c}^{\infty} U(E)dE = \frac{1}{kT} \int_{E_c}^{\infty} \frac{N_{is}\, f_{is}}{\tau_o} \exp\left(\frac{E_t - E}{kT} \right) dE$$

$$= \frac{N_{is}\, f_{is}}{\tau_o} \exp\left(\frac{E_t - E_c}{kT} \right) \qquad (12)$$

This may be equated with the final term of Eqn. (1) for the thermal emission of electrons

$$U_{(\text{no tunneling})} = N_{is}\, f_{is}\, n_1\, \sigma_n\, v_n \qquad (13)$$

and using Eqn. (2) for n_1, comparison of Eqns. (12) and (13) gives the result

$$\frac{1}{\tau_o} = N_c\, \sigma_n\, v_n \qquad (14)$$

We must bear in mind that Eqn. (14) is simply a consequence of requiring a smooth transition in our model with increasing temperature from field emission through thermionic-field emission to purely thermionic emission of electrons from the GB interface states. The two sides of Eqn. (14) are arrived at by unrelated physical models.[8,12] Nevertheless let us test whether this equation is quantitatively reasonable.

τ_o has been derived from first principles for one- and three-

dimensional delta-function potential wells which were used to characterize traps in insulators.[12] The theoretical estimates of τ_o were approximately 10^{-15} and 10^{-13} s in the 1D and 3D cases. Experimental results presented in the same study indicated a $\tau_o \approx 10^{-12}$ s. In Eqn. (14), $N_c \simeq 10^{19}$ cm^{-3} and $v_n \simeq 10^7$ cm s^{-1} at 300 K, with a fairly weak combined temperature dependence of T^2.[13] The capture cross-section for electrons σ_n can vary widely for deep traps in semiconductors, but is typically in the range of 10^{-16} to 10^{-12} cm^2.[14] Adopting a representative value of $\sigma_n \simeq 10^{-14}$ cm^2 gives order of magnitude agreement with Eqn. (14), which is satisfactory considering the very different types of experiments which are performed to phenomenologically determine σ_n and τ_o.

Since expression (9) gives satisfactory results in the thermionic-emission limit, and also leads to Eqn. (6) in the field-emission limit where Eqn. (10) is replaced by a delta-function at energy E_t, we are able to write for the general thermionic-field emission case that

$$U = \int_{E_t}^{\infty} U(E)dE = \frac{1}{kT} N_{is} f_{is} \int_{E_t}^{\infty} \frac{\exp((E_t-E)/kT)}{\tau_t(E)} \, dE$$

$$= \frac{N_{is} f_{is}}{kT \tau_o} \left(\int_{E_t}^{E_c} \frac{\exp((E_t-E)/kT) \, dE}{\exp(2(E_c-E)^{3/2}/3 E_{oo} V_d^{1/2})} \right.$$

$$\left. + \int_{E_c}^{\infty} \exp((E_t-E)/kT) \, dE \right) \qquad (15)$$

where the second integral is identical with Eqn. (12) and hence may be equated to Eqn. (13). Note that $\tau_t(E) = \tau_o$ in the range of E for this second integral.

A calculation has been made of the relative importance of thermionic-field emission (first term on RHS of Eqn. (15)) as compared to the usual thermal emission of SRH kinetics (second term on RHS of (15)). The ratio of these contributions to the emission may be expressed as

$$\frac{TFE}{TE} = \frac{\int_{E_t}^{E_c} \frac{\exp((E_t-E)/kT) \, dE}{\exp(2(E_c-E_t)^{3/2}/3 E_{oo} V_d^{1/2})}}{\int_{E_c}^{\infty} \exp((E_t-E)/kT) \, dE} \qquad (16)$$

The ratio is shown in Fig. 3 plotted vs. temperature for GB interface states of energy E_c - 0.55 eV (midgap) in silicon with $N_d V_d$

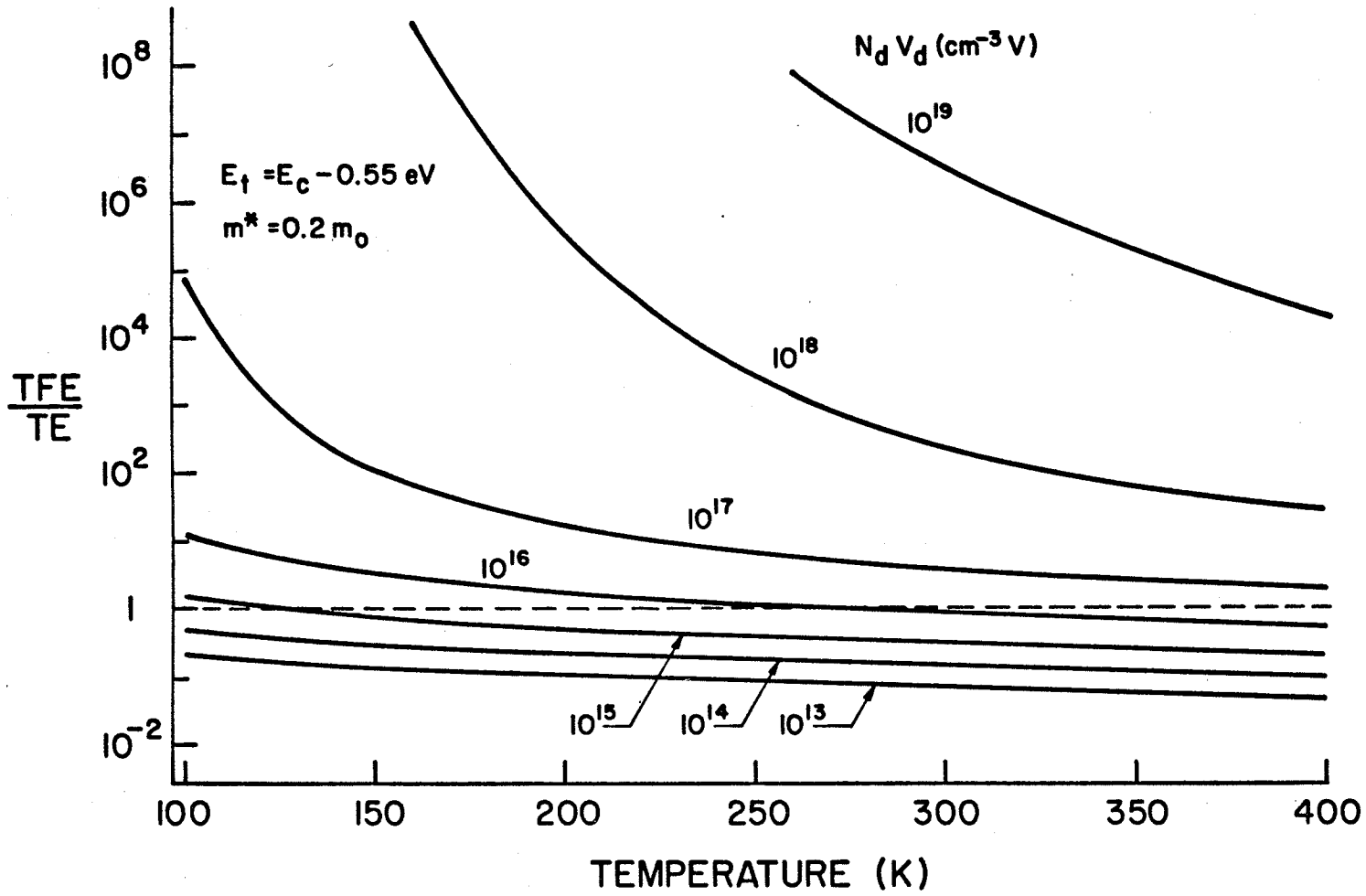

Fig. 3 Ratio of thermionic-field emission to thermal emission of majority carriers from GB interface states in silicon, vs. temperature, with $N_d V_d$ as parameter. N_d is the doping concentration and V_d is the diffusion potential (on the reverse-biased side of grain boundary). Effective mass $m^* = 0.2\, m_o$ is employed $\varepsilon_s = 11.8\, \varepsilon_o$ $E_c - E_t$ (or $E_t - E_v$ in p-type case) = 0.55 eV .

as a parameter. $(N_d V_d)^{1/2}$ enters into Eqn. (16) via $E_{oo} V_d^{1/2} = \frac{\hbar}{2}\left(\frac{N_d}{m^* \varepsilon_s}\right)^{1/2} V_d^{1/2}$. V_d is the diffusion potential in Fig. 2 on the reverse-biased side of the grain boundary. We have employed an effective mass $m^* = 0.2\ m_o$ in the calculations appropriate to the transverse effective mass in the conduction band ($0.19\ m_o$) which will dominate for tunneling. These calculations also will be accurate for p-type silicon in which tunneling is weighted by the light hole mass in the valence band $m^* = 0.16\ m_o$ [13]; in this case N_d is replaced by N_a in E_{oo}.

We observe in Fig. 3 that for values of $N_d V_d$ in excess of $\simeq 10^{16}$ $cm^{-3}V$ at a temperature of 300 K, or in excess of $\simeq 10^{15}$ $cm^{-3}V$ at 130 K, the ratio TFE/TE is greater than unity, which means that emission of electrons from the GB interface states is predominantly by thermionic-field emission.

In order to correct the SRH expressions to include TFE from the GB interface states, we must replace the emission term $N_{is}\ f_{is}\ \sigma_n\ v_n\ n_1$ in Eqns. (1) and (13) by $N_{is}\ f_{is}\ \sigma_n\ v_n\ n_1\ (\frac{TE+TFE}{TE})$. Defining

$$n_1' = n_1\left(1 + \frac{TFE}{TE}\right) \tag{17}$$

where (TFE/TE) is defined by Eqn. (16) and plotted in Fig. 3, we may generalize Eqn. (1) to

$$U_{cn} = N_{is}\ \sigma_n\ v_n\left[(1-f_{is})n - f_{is}\ n_1'\right] \tag{18}$$

Similarly, Eqn. (5) becomes

$$f_{is} = \frac{n\,\sigma_n + p_1\,\sigma_p}{\sigma_n(n + n_1') + \sigma_p(p + p_1)} \qquad (19)$$

A similar treatment applies for GBs in p-type semiconductors, provided the GB charge Q_{is} is positive.

In addition to knowing the ratio of thermionic-field emission to thermal emission, we are also interested in the absolute emission rate, given by Eqn. (15). This has been calculated for emission from interface states of various energies from E_c - 0.55 eV to E_c - 0.2 eV. These extreme cases are presented in Figs. 4 and 5, where we plot the emission rate (s^{-1}) per occupied interface state as a function of temperature, again with N_dV_d as a parameter. A value for τ_o of 10^{-12} s has been assumed.

We note from these results that for small N_dV_d, i.e. below $\approx 10^{15}$ $cm^{-3}V$, the emission process exhibits the temperature dependence characteristic of pure thermal emission to the conduction band. As N_dV_d increases further, however, the temperature dependence is reduced and for $N_dV_d \approx 10^{19}$ $cm^{-3}V$ it has all but disappeared. In this latter case the states empty by pure field emission at the energy E_t. In other words, the SRH kinetics are applicable for $N_dV_d \lesssim 10^{15}$ $cm^{-3}V$ and are a reasonable approximation at the higher temperatures up to 10^{16} $cm^{-3}V$. The approximation is better for energetically-deeper states.

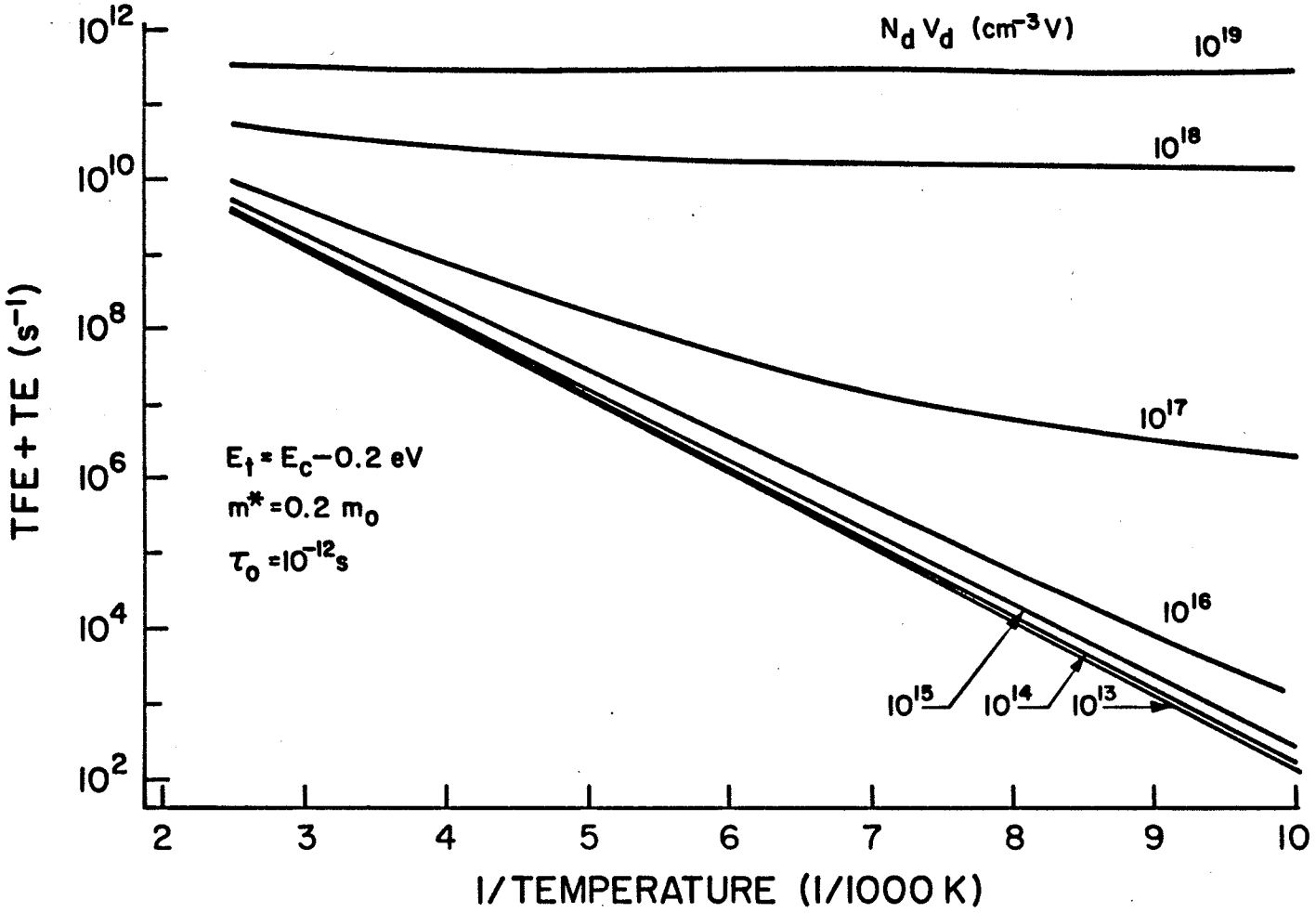

Fig. 4 Total emission rate from GB interface states per occupied state ($N_{is} f_{is} = 1$ in Eqn. (15)) for states of energy E_c - 0.2 eV; $m^* = 0.2\ m_o$, $\tau_o = 10^{-12}$ s.

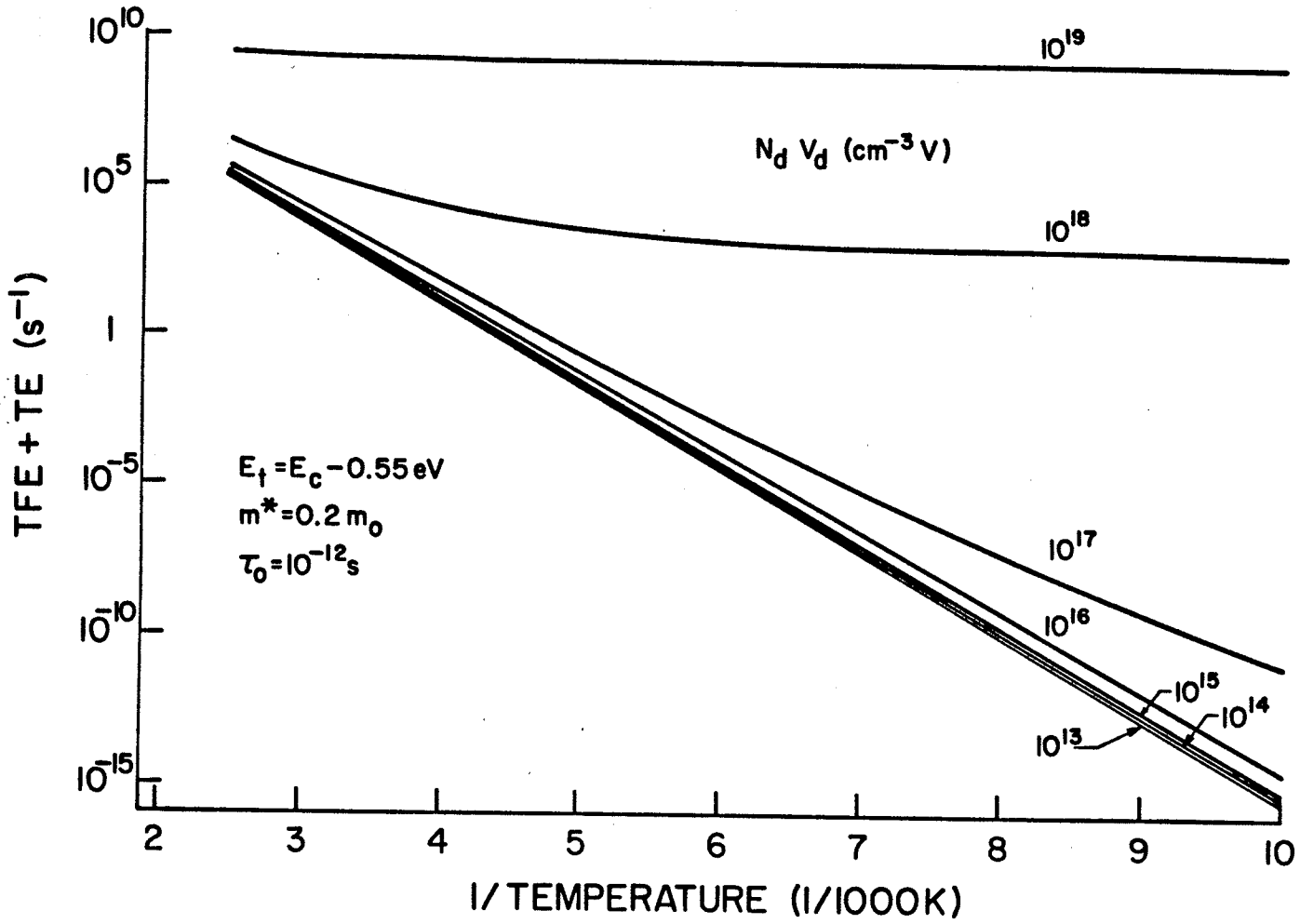

Fig. 5 Similar calculation to Fig. 4, but for GB interface states of energy E_c - 0.55 eV ; m^* = 0.2 m_o , τ_o = 10^{-12} s.

3. Experiments on Grain Boundaries in Silicon

Measurements of the current-voltage (I-V) characteristics of isolated electrically-active grain boundaries in silicon have been made; discussion of the experimental methods and results are presented elsewhere.[6,15] A typical example of the characteristics is given in Fig. 6. From these characteristics it is possible to extract the energy distribution of the GB interface states using a deconvolution scheme introduced by Seager and Pike.[1] This scheme assumes that the charge in the GB interface states remains in equilibrium with the majority carriers on the forward-biased side of the grain boundary.

When a voltage V is applied across the grain boundary, it divides between a forward voltage which lowers the diffusion potential (to the left of the GB in Fig. 2) and a reverse voltage V_2 which increases the diffusion potential on the other side. We have that $V_1 + V_2 = V$, but the distribution of voltage between the two sides depends among other things upon the charge in the GB interface states and how this charge changes with V. For interface states distributed in energy which are in equilibrium with the majority carriers on the forward-biased side, increases in V_1 are accompanied by more negative charge in the interface states. This exerts a negative feedback on V_1, and for high interface state densities tends to pin the energy of the Fermi level for the majority carriers at the grain boundary. The result of this is that V_1 is a very small portion of V, and since the electron current across the GB is controlled by V_1, the current increases slowly with V.[1,6]

By assuming that the GB interface states are filled to the Fermi level on the forward-biased side (i.e. that V_1 controls Q_{is}

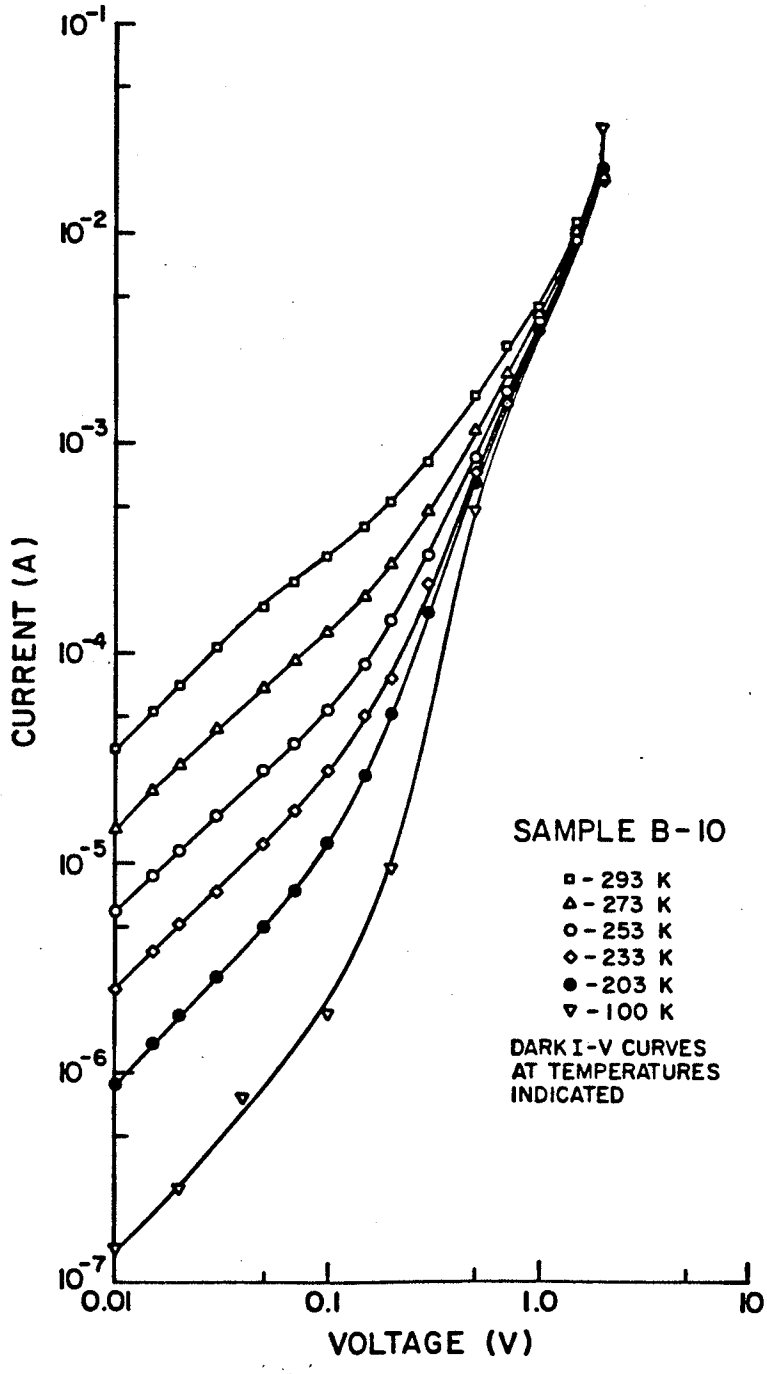

Fig. 6 Example of current-voltage characteristics of isolated grain boundary in p-type (Wacker Silso) silicon, for several measurement temperatures.

as well as the current) the energy distribution of the interface states $N_{is}(E)$ may be obtained by the deconvolution of the I-V characteristics. Results of this procedure are shown for several samples of GBs in p-type silicon from our laboratory in Fig. 7. Also shown in this figure are the results obtained by Seager and Pike on GBs in n-type silicon.

We believe that the densities obtained from the characteristics at low voltages are correct for all of these samples. This corresponds to the points closest to midgap for each device. As the densitites are explored towards the majority-carrier band and away from midgap, however, the applied voltages are increasing. This means that thermionic-field emission from the states is increasing, which has the effect of increasing n_1' in Eqn. (17), for n-type samples, thereby reducing f_{is} in Eqn. (19), and unpinning the electron Fermi level at the grain boundary. V_1 can then increase rapidly with further increases in voltage, which gives an <u>apparent</u> decrease in $N_{is}(E)$.

We cannot rule out the possibility that $N_{is}(E)$ is decreasing away from midgap. We wish to point out however that the results of Fig. 7 may also be explained by the onset of thermionic-field emission from GB interface states whose density is not decreasing. In this case, the apparent decrease in N_{is} results from the inability to store any additional electrons in the GB interface states as the voltage increases; equilibrium with the conduction band electrons at the GB is lost.

Let us examine the numerical values of TFE/TE at the critical point in Fig. 7 where the decline in N_{is} is observed. For the n-type case, $N_d = 10^{16}$ cm^{-3} and $V_d \approx 5$ V when the rapid rise in current is

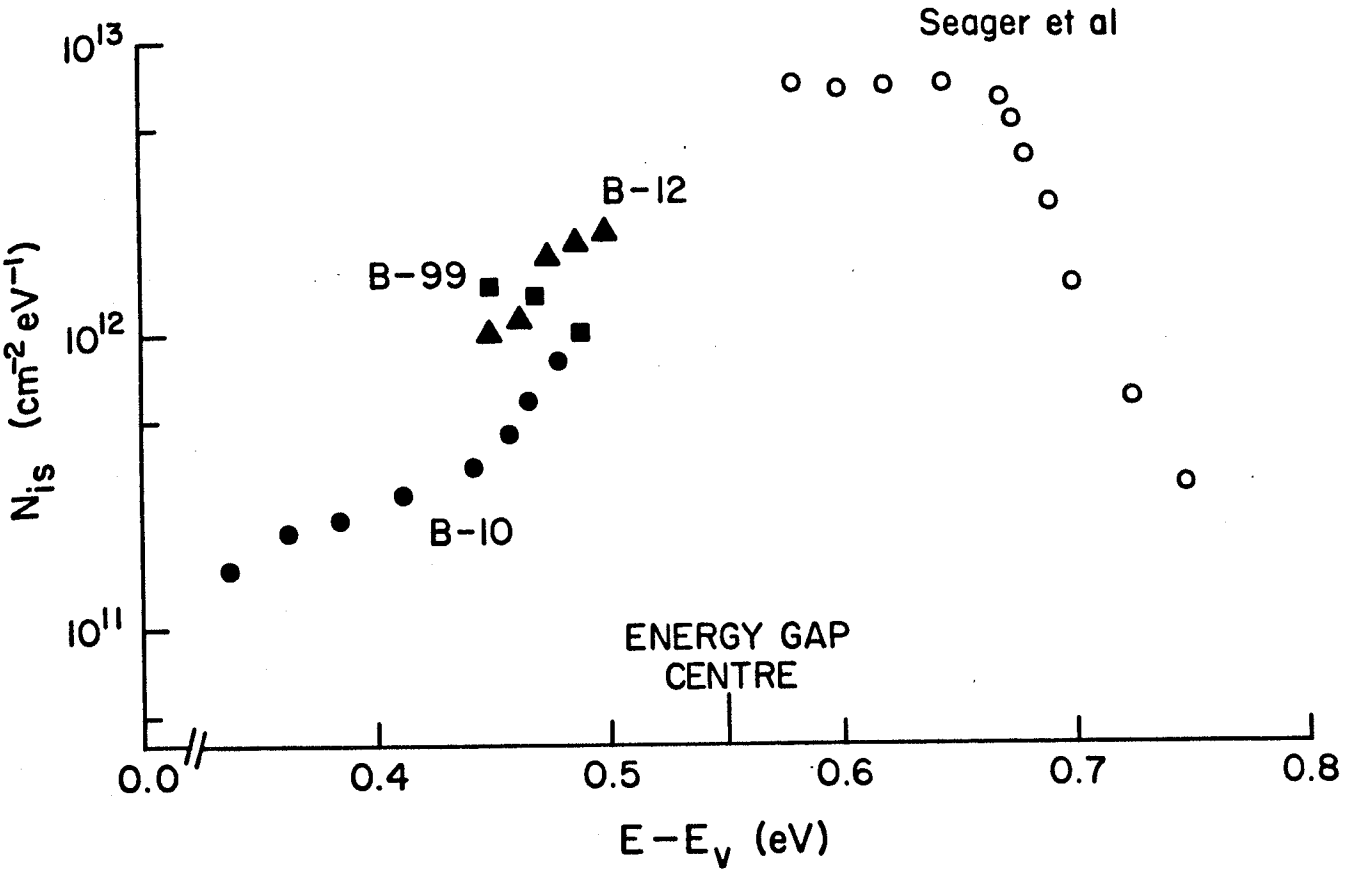

Fig. 7 Interface state density at grain boundaries in silicon, determined using Seager-Pike deconvolution scheme to interpret data such as that of Fig. 6. Data in lower half of energy gap obtained on p-type samples in our laboratory; data in upper half of energy gap from n-type samples of Seager and Pike.[1] Equilibrium of GB interface states with majority carriers on forward-biased side of grain boundary is assumed in these results. Decrease in N_{is} with energy away from midgap may also be explained by thermionic-field emission from states of constant density.

initiated.[1] From the theoretical results of the previous section, for $N_d V_d \simeq 5 \times 10^{16}$ cm^{-3} V , we obtain a ratio TFE/TE $\simeq$ 5 at 300K . Thermionic-field emission has exceeded thermal emission (which implies that f_{is} in Eqn. (19) is $\ll 1$ at the energy of the electron Fermi level. On the other hand, for $V_d \simeq 1$ V , the results of Fig. 3 imply that the GB interface states are occupied to within $\approx$ kT of the Fermi level. Our suggestions thus seem quantitatively reasonable.

Considering now the data on our p-type samples, Fig. 7 shows a less precipitous decline in N_{is} with increasing voltage, or increasing energy away from midgap. This is exactly what one expects on the basis of the above discussion, since the doping concentration in our case is somewhat lower; we have $N_a = 3 \times 10^{15}$ cm^{-3} and from Fig. 3 we expect only modest contributions to the emission rate from thermionic-field emission. For $V_d \simeq 3$ V , TFE/TE $\simeq$ 1 . In this case, the equilibrium with majority carriers is lost in a more gradual manner as the voltage across the grain boundary is increased.

This mechanism is of practical importance in improving the behaviour of varistors which employ grain-boundary conduction;[1] the present discussion suggests that the doping concentration may be of prime importance in controlling the nonlinearity of the characteristics of these devices.

The role of thermionic-field emission in the discharge of majority carriers from GB interface states must also be considered in the interpretation of transient capacitance measurements, in which a nonequilibrium charge is established in these states at reduced temperatures and the return to equilibrium is monitored.[2,3] Systematic errors in the energy scale of interface state distributions may other-

wise be encountered in certain cases.

4. Conclusions

Emission of majority carriers from localized states at interfaces such as grain boundaries may be assisted, in the presence of electric fields normal to the interface, by tunneling transitions through the space-charge regions. These effects may be described by a generalization of SRH kinetics which incorporates thermionic-field emission. The importance of TFE is apparent from our calculations even for modest doping concentrations and at room temperature. Interpretation of experiments including carrier transport across grain boundaries and transient capacitance measurements should include TFE, the effects of which may be well-disguised in phenomenological studies.

References

1. C.H. Seager and G.E. Pike, Appl. Phys. Lett., 35, 709 (1979).
2. C.H. Seager, G.E. Pike, and D.S. Ginley, Phys. Rev. Lett., 43, 532 (1979).
3. A. Broniatowski and J.-C. Bourgoin, Phys. Rev. Lett., 48, 424, (1982).
4. J. Werner, W. Jantsch, K.H. Froehner and H.J. Queisser, in Grain Boundaries in Semiconductors, North-Holland, New York, pp. 99-104 (1982).
5. M. Spencer, R. Stall, L.F. Eastman and C.E.C. Wood, J. Appl Phys., 50, 8006 (1979).
6. G.C. McGonigal, D.J. Thomson, J.G. Shaw, and H.C. Card, Phys. Rev. B, in press.
7. H.F. Mataré, Defect Electronics in Semiconductors, Wiley, New York, e.g. pp. 282-306 (1971) and references to earlier work therein.
8. W. Shockley and W.T. Read, Jr., Phys. Rev., 87, 835 (1952).
9. R.N. Hall, Phys. Rev., 87, 387 (1952).
10. L.B. Freeman and W.E. Dahlke, Solid St. Electron. 13, 1483 (1970).
11. F.A. Padovani and R. Stratton, Solid St. Electron, 9, 695 (1966).
12. I. Lundström and C. Svensson, J. Appl. Phys., 43, 5045 (1972).
13. S.M. Sze, Physics of Semiconductor Devices, 2nd Edition, Wiley, New York, (1981).
14. A.G. Milnes, Deep Impurities in Semiconductors, Wiley, New York, p93 (1973).
15. D.J. Thomson and H.C. Card, J. Appl. Phys., 54, 1976 (1983).

CHAPTER IV

INTERPRETATION OF CHARGE EMISSION FROM INTERFACE STATES AT SILICON GRAIN BOUNDARIES BY THERMAL EMISSION AND THERMIONIC-FIELD EMISSION*

* The contents of this chapter have been submitted for publication in IEEE Transactions on Electron Devices.

1. Introduction

The measurement and interpretation of majority carrier emission from defect states at grain boundaries in semicrystalline semiconductors has been the subject of several studies recently, e.g. Refs. 1-2, for the purpose of determining the density and energy distribution of these interface states. The charge in the interface states induces space-charge regions of uncompensated dopant impurities on both sides of the grain boundary and the concomitant electric fields present potential barriers which are the dominant factor controlling current transport through the boundary plane.

In the earlier work it has generally been assumed that excess majority carriers, introduced into the interface states through application of a bias voltage to the grain boundary, are released as a result of thermal emission to the majority carrier band, i.e. the conduction band for n-type semiconductors or the valence band in case of p-type material. The decay of the excess charge is monitored through measurement of the zero bias capacitance of the grain boundary at various temperatures and for several values of initial charge in the interface states. Assuming that the correct charge decay mechanism is used, it is then possible to deduce the density and energy distribution of the interface states.

The theory presented in the previous chapter[3] showed that under appropriate conditions, and considering only traps (or interface states) at a single energy level, a second charge release mechanism may be of practical importance. In this chapter we aim to extend the

theory to cover the case of interface states distributed in energy. We shall also show that, even when considering thermal emission only, the previous treatment in the literature of the emission rate is significantly in error.

2. Extension of the Combined Thermal Emission/Thermionic-Field Emission Theory to Interface States Distributed in Energy

The development that follows is in terms of electrons in an n-type semiconductor which are trapped in acceptor-like interface states. However, it is equally applicable to holes trapped in donor-like states in p-type material if we reverse the roles of electrons and holes, and the conduction and valence bands. It has been observed that for grain boundaries in n-type silicon, the interface states invariably contribute a net negative charge, while those in p-type material contribute a net positive charge[4]. In other words, grain boundary interface states act as majority carrier traps.

There are three basic mechanisms through which a filled state at an energy level E_t can lose its charge (Fig. 1):

a) pure thermal emission, whereby the trapped electron can be thermally excited to the conduction band (process 1);

b) pure field emission, in which case the electron tunnels through the potential barrier at the same energy level (process 2). In this case the trap energy level, E_{tl}, must lie between the bottom of the conduction band in the bulk, E_{cb}, and the conduction band energy at the boundary, E_c;

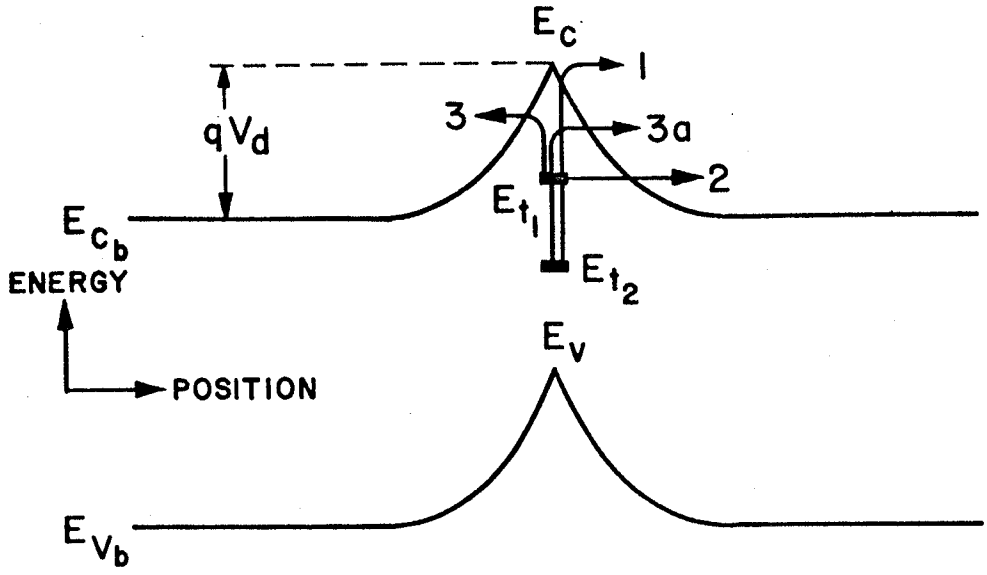

Fig. 1 Emission processes from two trap levels: E_{t_1} within range of potential barrier, and E_{t_2} below range of potential barrier. Process 1 is pure thermal emission from either level; process 2 is pure field emission from E_{t_1} only; processes 3 and 3a are thermionic-field emission from levels E_{t_1} and E_{t_2}, resp.

c) thermionic field emission (process 3a), where the electron receives thermal excitation prior to tunneling. This process applies to electrons in states that lie either above or below E_{cb}, but in the latter case thermal excitation to virtual states above E_{cb} must occur prior to tunneling (process 3a).

The thermionic-field emission rate per unit area at an energy range E to E + dE between E_{cb} and E_c and from traps at an energy level E_t with surface density $N_{is}(E_t)$ ($cm^{-2}eV^{-1}$) is given by[3]

$$U(E)dE = \frac{N_{is}(E_t)\, f_{is}}{\tau_t(E)} \frac{1}{kT} \exp\left(\frac{E_t - E}{kT}\right)dE \quad (cm^{-2}s^{-1}) \qquad (1)$$

where [5,6] $$\tau_t = \tau_o \exp\left[\frac{2(E_c - E)^{3/2}}{3\, E_{oo} V_d^{1/2}}\right] \quad (s) \qquad (2)$$

$$E_{oo} = \frac{\hbar}{2}\left(\frac{N_d}{m^* \varepsilon_s}\right)^{1/2} \quad (volts) \qquad (2a)$$

and $\tau_0 \simeq 10^{-12}$ s.[3,6]

The other quantities in Eqns.(2) and (2a) are the conduction band to trap energy difference $E_c - E_t$ (eV), the reduced Planck's constant $\hbar(=h/2\pi)$(Js), the effective electron mass m* (kg), the permittivity of silicon ε_s (F/m), the diffusion potential V_d(V), and the doping concentration N_d (m^{-3}). $f_{is}(E_t) = (1 + \exp\left[E_t - (E_c - E_s)/kT\right])^{-1}$ is the occupation function of the traps where E_s marks the transition from

filled to empty grain boundary interface states, as it is assumed that the electrons in the interface states are in equilibrium with each other and follow a Fermi-Dirac distribution with a trap Fermi level $E_c - E_s$.

Although tunneling can only occur via real or virtual states between E_c and $E_c - qV_d$, Eqn. (1) also applies to the pure thermal emission component where E lies in the conduction band at the grain boundary, i.e. $E > E_c$, but with τ_t replaced by τ_o.[3]

The energy band diagram of the grain boundary under bias is shown in Fig. 2. On the forward biased side the bulk Fermi level E_{Fb} is brought closer to E_c by an amount qV_1 where V_1 is the fraction of the applied voltage V which appears across the forward biased side of the grain boundary. This lowers the diffusion potential on the forward biased side from its zero bias value V_{do} to $V_{do} - V_1$. Similarly, the diffusion potential on the reverse biased side is increased to $V_{do} + V_2$. The additional charge in the grain boundary interface states is determined by the position of the Fermi level at the grain boundary $E_c - E_s$. At time $t = 0$, the bias is removed and the energy band diagram is as shown by the solid lines in Fig. 3. The additional charge is gradually released and at $t = \infty$ the equilibrium state (illustrated by the dashed lines) will be reached.

The zero bias equilibrium diffusion potential V_{do} can be determined from measurement of the zero bias capacitance or J - V data, while V_1 can be deduced from J - V data. The droop of the Fermi level

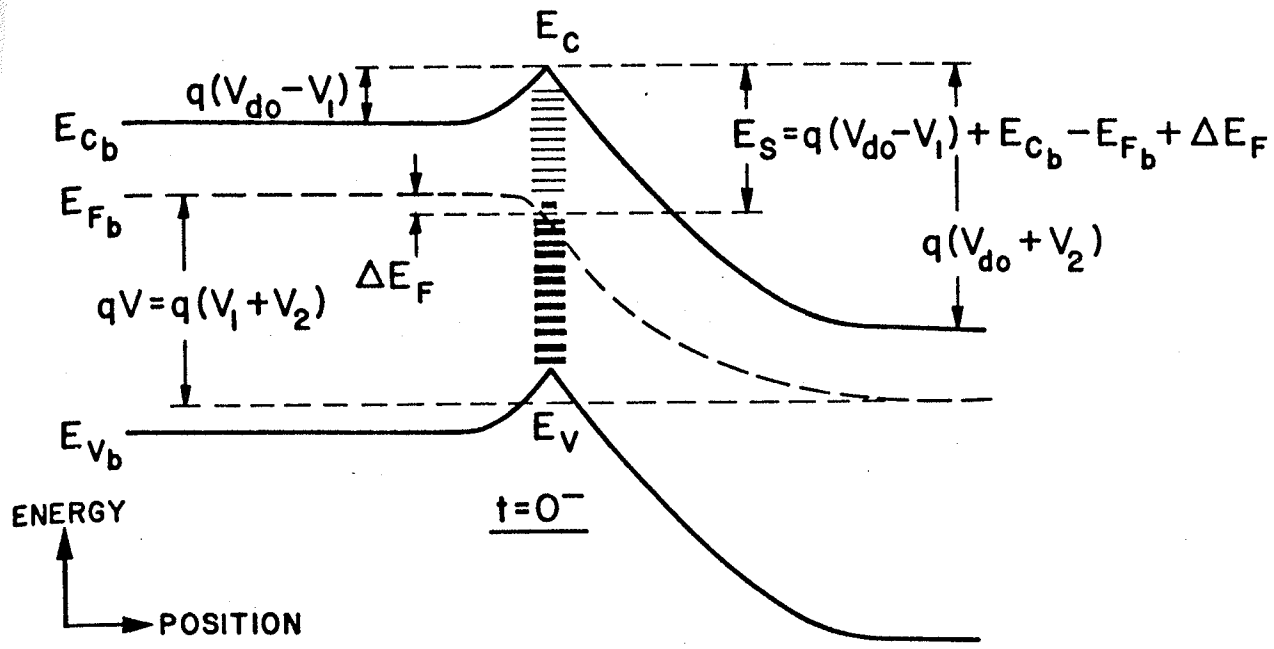

Fig. 2 Band diagram in vicinity of grain boundary under applied bias in steady state just prior to bias removal.

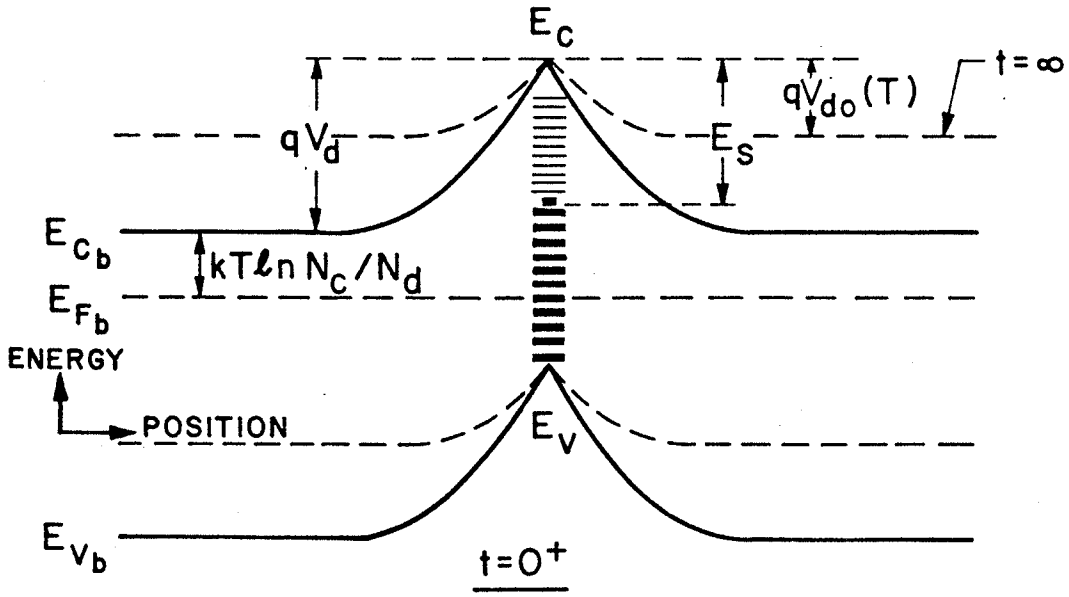

Fig. 3 Band diagram in vicinity of grain boundary immediately following bias removal ($t = 0+$). Dotted lines indicate equilibrium state ($t = \infty$).

at the grain boundary, ΔE_F, can be estimated from numerical calculations by finite-element methods.[7]

Note that although $E_{cb} - E_{Fb} = kT \ln N_c/N_d$ is temperature dependent, the barrier height $q\phi_b = qV_{do} + kT \ln N_c/N_d = E_c - E_{Fb}$ is not, due to pinning of the Fermi level, except for low values of the interface state density, N_{is}, around the equilibrium Fermi level. This will be discussed more fully in section 4. Therefore, the zero bias diffusion potential V_{do} has a temperature dependence which is opposite to that of $kT \ln N_c/N_d$. All these quantities will be evaluated in section 4.

First, let us consider the total thermal emission (TE) component at $t = 0+$, where we will assume that all trap states below E_{Fb} in Fig. 3 remain filled. In that case

$$U_{TE} = \int_{E_t = E_{Fb}}^{E_c} \int_{E = E_c}^{\infty} \frac{N_{is}(E_t) f_{is}(E_t)}{kT\,\tau_o} \exp\,[(E_t - E)/kT]\; dE\; dE_t \qquad (3)$$

The inner integral represents TE from states at energy level E_t to all states in the conduction band, while the outer integral yields the sum of the contributions from all trap states between E_{Fb} and E_c. Equation (3) can be simplified by evaluation of the inner integral to

$$U_{TE} = \int_{E_t = E_{Fb}}^{E_c} \frac{N_{is}(E_t) f_{is}(E_t)}{\tau_o} \exp\,[(E_t - E_c)/kT]\, dE_t \qquad (4)$$

where $E_{Fb} = E_c - qV_d - kT \ln N_c/N_d$ and V_d follows from a capacitance measurement at $t = 0^+$ provided that the doping concentration is spatially uniform in the depletion regions adjacent to the grain boundary.

The quantity we wish to determine is $N_{is}(E_t)$. Since TE occurs primarily from the higher filled states because of the exponential decrease with E_t, only a small error will be introduced by taking $N_{is}(E_t) \simeq \text{constant} = N_{is}(E_c - E_s)$. In other words, provided the energy dependence of N_{is} is weak compared to that of f_{is}, we can write

$$U_{TE} \simeq \frac{N_{is}(E_c-E_s)}{\tau_o} \int_{E_{Fb}}^{E_c} \frac{\exp[(E_t-E_c)/kT]\, dE_t}{1 + \exp([E_t-(E_c-E_s)]/kT)} =$$

$$\frac{N_{is}(E_c-E_s)}{\tau_o} kT\, e^{-E_s/kT} \ln \frac{1 + e^{E_s/kT}}{1 + e^{E_s/kT} \exp[-(qV_d+kT \ln N_c/N_d)/kT]} (cm^{-2}s^{-1}) \quad (5)$$

In virtually all situations, with the possible exception of extremely high doping (where $E_{cb} - E_{Fb} = kT \ln N_c/N_d$ is small) and heavy bias at $t = 0^-$ (near flat band condition; V_d is large at $t = 0^+$), $e^{E_s/kT}$ will be much larger than 1, while on the other hand $\exp[(E_s - (qV_d + kT \ln N_c/N_d))/kT]$ will be much less than 1 except for very small bias at $t = 0^+$.

Hence, at $t = 0^+$

$$U_{TE} \simeq \frac{N_{is}(E_c - E_s)}{\tau_o} E_s \, e^{-E_s/kT} \quad (cm^{-2}s^{-1}) \qquad (6)$$

The appearance of E_s in Eqn.(6) is a consequence of the equal contribution to the emission rate from all states above $E_c - E_s$, because the decrease in f_{is} with energy is exactly counteracted by the increase in the thermal emission probability with energy.

It is interesting to note that inclusion of an additional constraint to those applying to Eqn.(5), viz. $f_{is} = 0$ for $E_c - E_t < E_s$ and $f_{is} = 1$ for $E_c - E_t > E_s$ (OK approximation), yields

$$U_{TE} \simeq \frac{N_{is}(E_c - E_s)}{\tau_o} kT \, \{\exp[-E_s/kT] - \exp[-(qV_d + kT \, \ln N_c/N_d)/kT]\} \qquad (5a)$$

while the equivalent to Eqn.(6) is

$$U_{TE} \simeq \frac{N_{is}(E_c - E_s)}{\tau_o} kT \, e^{-E_s/kT} \qquad (6a)$$

The thermal emission rate given by Eqn.(6a) is identical to expression (7) in Ref. 1, but it is considerably less than that of Eqn.(6), and, when used to interpret transient capacitance data, it will lead to an overestimation of N_{is} for all but the shallowest traps. This may in part explain the results of Ref. 1 where the OK occupation function was used.

Next, we shall consider the thermionic-field emission (TFE) component of the overall emission rate. The starting state at $t = 0^+$ is illustrated in Fig. 3, and the following points should be borne in mind. Filled states above $E_t = E_c - qV_d$ can lose their charge through direct tunneling at the same energy level (pure field emission), as well as at higher energy levels (up to E_c) with thermal excitation to virtual states in the range from E_{Fb} to E_c. Filled states in the range from E_{Fb} to E_{cb} require thermal assistance prior to tunneling. The low bias case where the trap Fermi level lies below E_{cb} need <u>not</u> be considered separately, however.

The TFE from any trap level E_t between E_{Fb} and E_c to the conduction band through the range E to E + dE between E_{cb} and E_c is given by Eqn.(1). Thus, the total TFE from a single energy level E_t will be

$$U_{TFE(E_t)} = \int_{E=E_{cb}}^{E_c} \frac{N_{is}(E_t)\, f_{is}(E_t)}{\tau_t(E)} \; \frac{1}{kT}\, e^{(E_t-E)/kT}\, u(E-E_t)dE \qquad (7)$$

where the Heaviside step function $u(E-E_t)$ ensures that no field emission takes place from trap levels E_t above E_{cb} through states between E_{cb} and E_t.

The total TFE component at $t = 0^+$ from all traps can now be described by

$$U_{TFE} = \int_{E_t=E_{Fb}}^{E_c} \frac{N_{is}(E_t) f_{is}(E_t)}{\tau_o kT} \int_{E=E_{cb}}^{E_c} \frac{u(E-E_t)\, e^{(E_t-E)/kT}}{\exp\left[\dfrac{2(E_c-E)^{3/2}}{3E_{oo}V_d^{1/2}}\right]}\, dE\, dE_t \qquad (8)$$

As before, we shall take $N_{is}(E_t)$ to be approximately constant and equal to $N_{is}(E_c-E_s)$, so that

$$U_{TFE} \simeq \frac{N_{is}(E_c-E_s)}{\tau_o kT} \int_{E_t=E_{Fb}}^{E_c} f_{is}(E_t)\, e^{E_t/kT} \int_{E=E_{cb}}^{E_c} \frac{u(E-E_t)\, e^{-E/kT}}{\exp\left[\frac{2(E_c-E)^{3/2}}{3\, E_{oo} V_d^{1/2}}\right]}\, dE\, dE_t \quad (9)$$

We can now combine the results given by Eqns.(5) and (9) to arrive at the total emission rate of trapped electrons at $t = 0^+$

$$U_{TOT(t=0+)} = U_{TE} + U_{TFE} \quad (10)$$

By monitoring the discharge rate at $t = 0^+$ through the initial rate of change of the grain boundary capacitance, the interface state density at energy level E_c-E_s can be determined in the following manner.

If we designate the number of charges in the interface states and the zero bias capacitance (both per unit area) by Q_o and C_o, respectively, then[1], for a spatially uniform doping concentration

$$Q_o = \varepsilon_s N_d / C_o \text{ (cgs units)} \quad (11)$$

and at $t = 0^+$

$$-\frac{dQ_o}{dt} = \frac{\varepsilon_s N_d}{C_o^2} \frac{dC_o}{dt} = U_{TOT} \quad (12)$$

Unfortunately, however, the double integral in Eqn.(9) has no closed form solution, necessitating a numerical approach. For this purpose it is convenient to arbitrarily select the conduction band energy at the grain boundary as reference level, i.e. $E_c = 0$. Then the equation to be used for computer evaluation reads

$$\frac{\tau_o}{N_{is}(-E_s)} \; U_{TOT(t=0^+)} \equiv U_{TOTN} = U_{TEN} + U_{TFEN} \tag{13}$$

where

$$U_{TEN} = kT\, e^{-E_s/kT} \ln \frac{1 + e^{E_s/kT}}{1+\exp[q(V_{do}-V_1-V_d+\Delta\phi_F)/kT]} \tag{14}$$

and

$$U_{TFEN} = \frac{1}{kT} \int_{E_t=-qV_d-kT\,\ln N_c/N_d}^{o} [e^{-E_t/kT} + e^{E_s/kT}]^{-1} \cdot$$

$$E=\int_{-qV_d}^{o} u(E-E_t)\, \exp\left[\frac{-E}{kT} - \frac{2(-E)^{3/2}}{3E_{oo}V_d^{1/2}}\right] dE\,dE_t \tag{15}$$

with $E_s = q(V_{do}-V_1) + kT\,\ln N_c/N_d + q\Delta\phi_F$ (eV).

The quantities E_t and E are also expressed in eV and they are negative, i.e. measured from the conduction band edge at the grain boundary. E_{oo}, V_{do}, V_1 and $\Delta\phi_F = \Delta E_F/q$ are all expressed in volts. If all energies are measured in eV we express k in eV/K, and we may drop the electronic charge q from the above expressions.

In order to perform the computation, and present the results of the theory developed here, numerical values must be found for the following parameters: E_{oo} (from Eqn.(2a) and knowledge of the doping concentration), kT $\ln N_c/N_d$, V_{do}, V_d, V_1 and $\Delta\phi_F$. After section 3 we shall determine these quantities as a function of temperature and applied bias for the grain boundary sample B-12 which was used in the experiments.

3. Sample Fabrication and Measurements

The material used in this study was p-type cast silicon of large grain size (typically 1 mm) of the 'Silso' type, obtained from Wacker Chemitronic Ltd. The doping concentration N_a from bulk measurements (C^{-2} vs V of Schottky barrier capacitance-voltage characteristics for diodes within single grains) was $\approx 3\times10^{15}$ cm^{-3}. Nevertheless, we found the doping in the vicinity of the grain boundary to be significantly different from the bulk value. This will be discussed further in section 5.

The polycrystalline wafers (100 mm x 100 mm x 0.4 mm) were cut into strips approximately 1 mm x 20 mm. These strips were chemically polished in 3:1:1 HNO_3 (79%), HF (49%), glacial acetic acid, for three minutes to minimize saw damage and to highlight the grain boundaries. Grain boundaries were examined under an optical microscope to identify those which were planar and which extended over the entire cross-section of the strip in both the lateral and vertical directions; the latter requirement was determined by examining the back face of the samples.

Aluminum contacts were evaporated and sintered at 600°C for 20 minutes in N_2 to form ohmic contacts. By using a 200 μm thick wire as a mask centered over the grain boundary during the aluminum evaporation, contacts at approximately 100 μm from the boundary were obtained. Voltages, and higher current values were measured with Tektronix 200-series digital multimeters, while for the lower current values a Keithley 610C electrometer was employed. Where necessary, the voltage drop across the current meter was taken into account. Capacitance and capacitance transients were measured with a Boonton 72 AD digital capacitance meter with analog output, and recorded on either a Hewlett Packard 7132A or a Gould Brush 220 strip-chart recorder, depending on the required speed.

Temperatures were measured with a Fluke 2100 A digital thermometer with analog output which formed an integral part of a cryogenic

system whose construction and performance is described in detail in the next chapter. J-V, capacitance, and capacitance transient measurements were performed at temperatures from 300 K to 93 K.

4. Measurement and Interpretation of Steady-State Current-Voltage Characteristics

The steady-state current-voltage characteristics of a grain boundary in general consist of a component due to the transport of majority carriers over the potential barrier of height $V_{do} - V_1$ (Fig. 2) on the forward biased side of the grain boundary, J_1, a component due to minority carrier transport in the opposite direction, J_2, over a barrier of similar height, and finally a component associated with recombination of electrons and holes in grain boundary interface states, J_3. However, the first component is completely dominant over the other two, at least under dark conditions[7-13]. Thus, the currents shown in Fig. 4 are to be identified with the transport of majority carriers (in our case, holes, although the band diagram of Fig. 2 actually applies to n-type Si) over the potential barrier. The unusual behaviour below 193 K is attributed[14] to leakage current resulting from surface damage. The current for low voltage and 93 K was indistinguishable from that at 113 K. The leakage conductance is calculated to be 100 nS, which corresponds to 408 nS/cm of circumference for our sample. This leakage conductance is not reflected in the theoretical J-V relationship Eqn.(16).

It has been shown [7] that the majority carrier component is

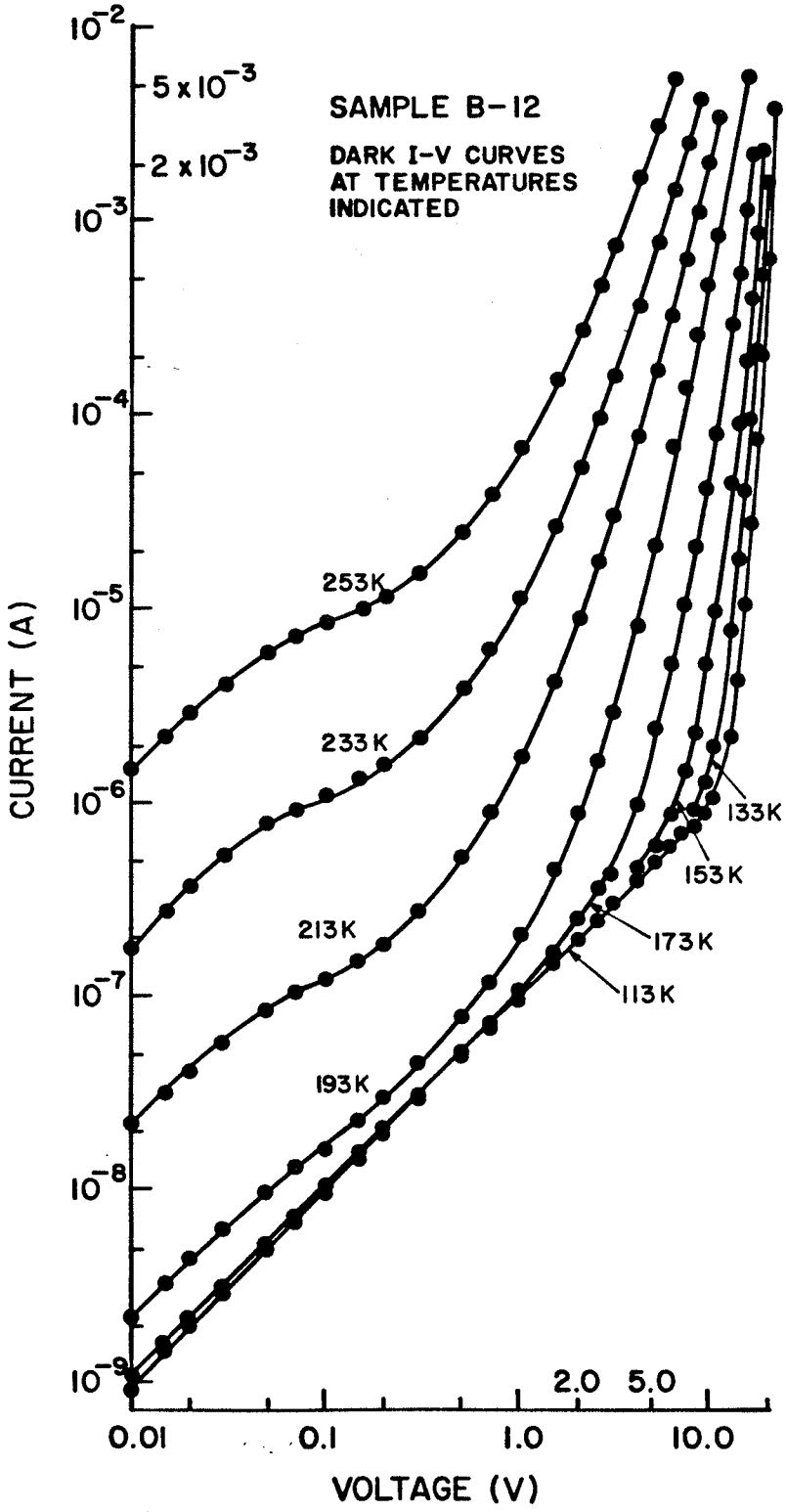

Fig. 4 Dark I-V characteristics for various temperatures, showing dominance of surface leakage below 193K.

described by

$$J_1 \ (\approx J) = qN_a\mu_p \xi_{mf} \exp(\frac{-V_{do}}{V_T}) \exp(\frac{V_1}{V_T}) \ [1 - \exp(\frac{-V}{V_T})] \qquad (16)$$

The new quantities are the hole mobility, μ_p, the thermal voltage $V_T = kT/q$, and the maximum electric field in the space-charge region on the forward biased side which is given by

$$\xi_{mf} \simeq [\frac{2qN_a}{\varepsilon_s} (V_{do} - V_1 - V_T)]^{1/2} \qquad (17)$$

For low values of the applied voltage ($V \ll V_T$ and $V_1 \ll V_T$) we can simplify Eqn.(16) to

$$J \simeq qN_a\mu_p \xi_{mf} \exp(\frac{-V_{do}}{V_T}) \frac{V}{V_T} \qquad (18)$$

and define an activation temperature for the potential barrier at the grain boundary as

$$T_a = - \frac{d \ ln\frac{J}{qN_a\mu_p(T)\xi_{mf} \ V/V_T)}}{d(1/T)} = - \frac{d}{d(1/T)} \ln(\exp(- \frac{V_{do}}{V_T})) =$$

$$\frac{q}{k} V_{do}(T) + \frac{q}{k} \frac{1}{T} \frac{dV_{do}(T)}{d(1/T)} = \frac{q}{k} (V_{do}(T) - T \frac{dV_{do}(T)}{dT}) \qquad (19)$$

As was mentioned briefly in section 2, the temperature dependence of $V_{do}(T)$ is the opposite to that of $\frac{kT}{q} \ln N_c/N_d$ (the energy difference between the Fermi level and bottom of the conduction band in the bulk) for large values of $N_{is}(E)$ around $E = E_F$. This can be explained as follows. A slight increase in the bulk Fermi level relative to E_c would cause a substantial increase in the grain boundary charge which, in turn, must be balanced by an increase of the charge due to uncompensated impurities in the depletion regions. As a result, $qV_{do} = E_c - E_{cb}$ will increase and offset the originally assumed decrease in $E_c - E_{Fb}$. This negative feedback effect is referred to as pinning of the Fermi level by interface states. Consequently, Eqn.(19) can be rewritten in the form

$$T_a = \frac{q}{k} \left(V_{do}(T) + T \frac{k}{q} \ln N_c/N_d\right) \tag{20}$$

from which we obtain the temperature dependent expression for the zero bias diffusion potential

$$V_{do}(T) = \frac{k}{q} T_a - \frac{kT}{q} \ln N_c/N_d \tag{21}$$

In order to find the activation temperature T_a we write the left hand side of Eqn.(19) in the form

$$T_a = - \frac{d}{d(1/T)} \left[\ln \left(\frac{J(T)}{\mu_p(T)} V_T \right) - \ln \left(q \, N_a \xi_{mf} \, V \right) \right] \qquad (22)$$

where we can neglect the second term on the right hand side after differentiation because according to Eqn.(17), $V_{do}(T)$ appears here only to the power one half rather than in an exponential as in the first term. Therefore,

$$T_a \simeq - \frac{d}{d(1/T)} \ln \frac{J(T)}{\mu_p(T)} V_T = - \frac{d}{d(1/T)} \ln \frac{I(T)/A}{\mu_p(T)} \frac{kT}{q} =$$

$$- \frac{d}{d(1/T)} \ln \frac{I(T)T}{\mu_p(T)} \qquad (23)$$

In this expression A is the area of the grain boundary, and the temperature dependent low-field hole mobility is given by[15]

$$\mu_p(T) = 54.3 \, T_n^{-0.57} + \frac{407 \, T_n^{0.316}}{T_n^{2.546} + N_a/(2.67 \times 10^{17})} \qquad (24)$$

where $T_n = T/300$, and N_a and μ_p are expressed in cm^{-3} and cm^2/Vs, respectively.

For the n-type case the electron mobility may be written as

$$\mu_n(T) = 88 \, T_n^{-0.57} + \frac{1252 \, T_n^{0.216}}{T_n^{2.546} + N_d/(1.43 \times 10^{17})} \qquad (24a)$$

In Fig. 5a we have plotted $-\ln(I(T)T/\mu_p(T))$ versus the reciprocal temperature 1/T, and using a least squares linear approximation we find the slope to be

$$T_a = 5.90 \times 10^3 \text{ (K)} \tag{25}$$

It should be pointed out here that in Eqn.(23) we have used current values at V = 1 mV, which are extrapolated from the I-V relationships shown in Fig. 4, in order to satisfy the conditions $V \ll V_T$ and $V_1 \ll V_T$. This procedure is legitimate because of the linear behaviour for low voltages, i.e., a slope of one on the log-log graph of Fig. 4. Notice also that the slope of $-\ln(I(T)T/\mu_p(T))$ vs 1/T has a very weak temperature dependence (which was ignored to arrive at Eqn.(25)) and this is indicative of a spatially uniform grain boundary[16]; i.e. the zero bias diffusion potential V_{do} is virtually independent of position on the boundary plane.

Combining Eqns.(19) and (25) we find that for our sample

$$V_{do}(T) = 0.509 - 5.96 \times 10^{-4}T \text{ (V)} \tag{26}$$

where we have used $\ln N_v/N_a$ (p-type) rather than $\ln N_c/N_d$ (n-type), with $N_v = 10^{19}$ cm^{-3} and $N_a \simeq 10^{16}$ cm^{-3}. Figure 5b shows the zero bias diffusion potential as a function of temperature.

A second quantity that can be derived from the current-vol-

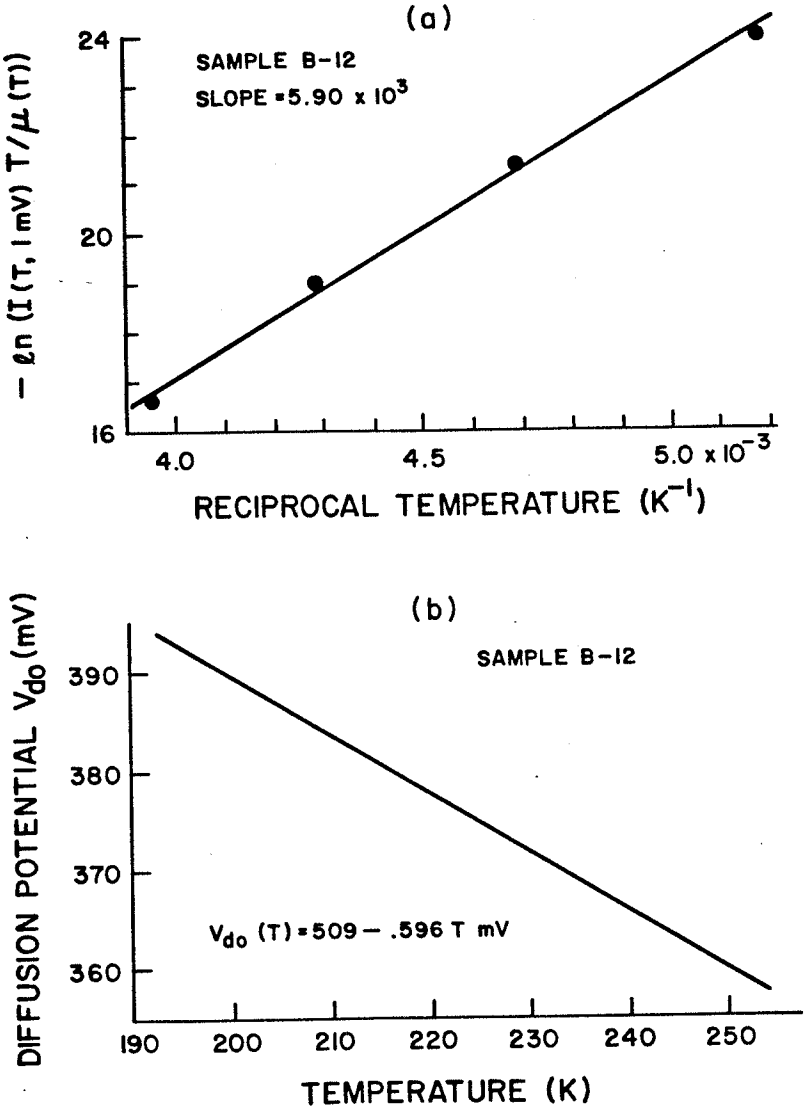

Fig. 5. (a) Determination of activation temperature T_a. A slight temperature dependence is noticeable.

(b) Equilibrium diffusion potential vs T for strong pinning of the Fermi level.

tage characteristics of Fig. 4, and which must be known in order to evaluate the integrals in section 2, is the voltage V_1, which depends strongly on the applied voltage V, and in an as yet unknown manner upon temperature.

First of all, it should be realized that a measure of doubt exists as to whether the use of the maximum field on the forward biased side of the boundary, as stated in Eqn.(16), applies in all cases. As discussed in Ref. 7, the argument revolves around an estimation of the relative values of the majority carrier diffusion velocity, v_d, and collection velocity, v_r. If $v_r \gg v_d$ then Eqn.(16) is correct provided that the expression for the maximum field (Eqn.(17)) is accurate. We eliminate this problem by introducing a temperature dependent correction factor, C_T, by modifying Eqn.(18) to read

$$J = C_T \, q \, N_a \, \mu_p \, \xi_{mf} \, \exp\left(\frac{-V_{do}}{V_T}\right) \frac{V}{V_T} \qquad (27)$$

and then, by comparison with measured currents, we obtain C_T for each temperature. In the range from 253 K to 193 K we find $C_{253} \simeq 0.53$ decreasing to $C_{213} \simeq 0.34$, but $C_{193} \simeq 0.48$. The latter value may arise from a slight influence by the surface leakage current. An added advantage of using the empirical correction factor is that it corrects for any misestimation of the doping concentration which, in Eqn.(16), appears explicitly, as well as implicitly in ξ_{mf}.

For large applied bias voltages $V \gg V_T$ the current-voltage

relationship becomes

$$J = C_T\, q\, N_a\, \mu_p(T)\, \xi_{mf}\, e^{\frac{-(V_{do}-V_1)}{V_T}} \tag{28}$$

and, using expression (17) for ξ_{mf}, and the boundary surface area A, the following relationship can easily be derived:

$$V_1(V,T) = V_{do}(T) + V_T \ln\frac{I(V,T)}{C_T \mu_p(T)(V_{do}-V_T-V_1)^{1/2}} -$$

$$V_T \ln q\, N_a A\left(\frac{2qN_a}{\varepsilon_s}\right)^{1/2} \tag{29}$$

where all known constants have been collected in the second logarithm.

Equation (29) can be solved numerically for all temperatures for which an I-V curve is available and in Fig. 6 we show the result for the temperature extremes of 253 K and 193 K. The results for the intermediate temperatures were found to lie between the curves shown.

Over the indicated temperature and voltage ranges, and with sufficient accuracy for the purpose of evaluating the emission integrals, we obtain

$$V_1(V) \simeq 0.07\, V^{1/2} \quad \text{(volts)} \tag{30}$$

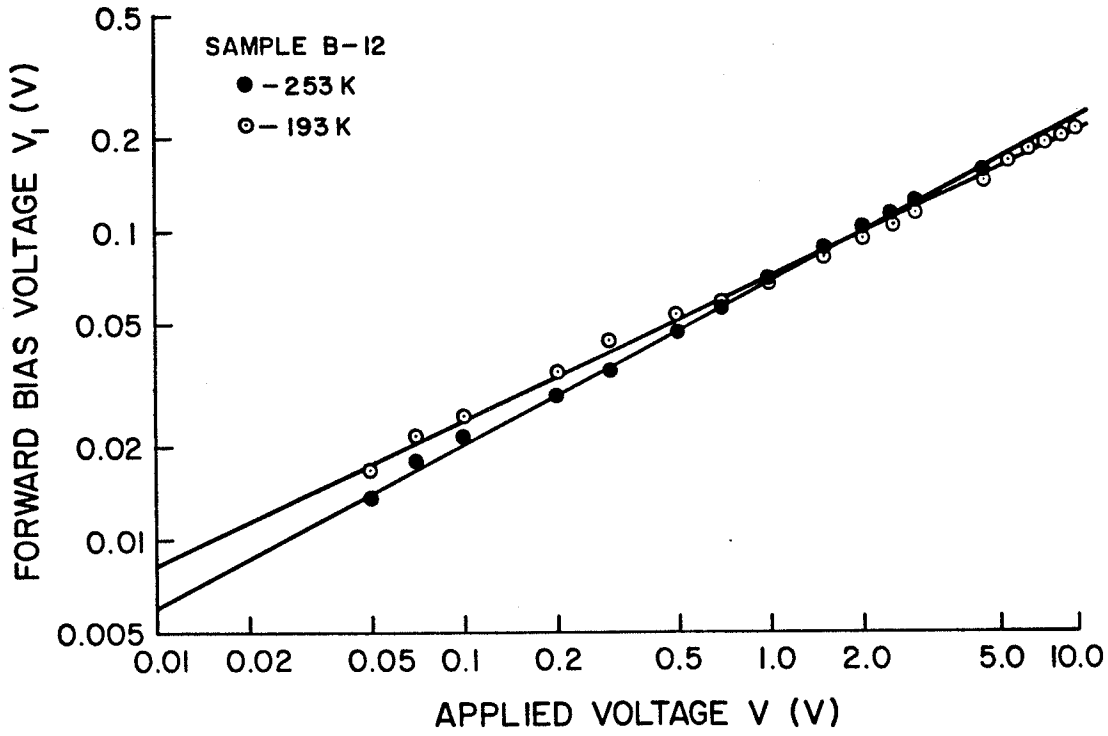

Fig. 6 Dependence of voltage on forward biased side (V_1) on total applied voltage (V) for extremes of the useful temperature range. Approximate relationship is $V_1 \approx 0.07\ V^{1/2}$.

The physical basis for this result is that, for uniform doping and a density of interface states which is constant in energy, changes with V in the grain boundary interface charge are proportional to V_1 above. This charge is also proportional to the width W of the adjacent space-charge regions and for $V >> V_1$, W varies as $V^{1/2}$.

5. Measurement and Interpretation of Steady-State Capacitance-Voltage Characteristics

Capacitance measurement are used extensively in semiconductor work. Specifically, steady-state capacitance as a function of applied voltage for abrupt p^+-n or n^+-p junctions, or Schottky barriers, yields information about the doping profile and, in restricted cases, the built-in junction potential or barrier heights[17]. For example, if we plot C^{-2} vs V for an abrupt junction, and a straight line results then the (uniform) doping concentration follows from $N = 2/(A^2 q\varepsilon(d(1/C^2)/dV)$ and the built-in potential (or zero bias diffusion potential in the case of a Schottky barrier) is given by the intercept with the voltage axis. In general, the doping at a distance x from the junction is

$$N(x) = \frac{2}{A^2 q\varepsilon} \left(\frac{d\ 1/C^2}{dV}\right)^{-1} \tag{31}$$

and

$$x = \frac{\varepsilon A}{C} \tag{32}$$

In the context of capacitance measurements, a grain boundary can be modelled as two back-to-back Schottky barriers, i.e. two capacitors in series, each with a capacitance given by Eqn.(32) where x is the depletion region width on the appropriate side. For very large applied voltages the doping profile on the reverse biased side may be found using Eqn.(31) because (see Fig. 2) the capacitance of the forward biased side is much larger than that of the reverse biased side which is therefore approximately equal to the measured overall capacitance.

In general, however, it is not possible to determine an arbitrary doping profile near the boundary plane by the above method, even if symmetry is assumed. Nevertheless, if the doping concentration in the vicinity of the boundary is uniform, but not necessarily the same as in the bulk, then its value can be determined by the method outlined below.

For uniform doping near the grain boundary, the high frequency capacitance on the forward biased side, C_f, and that of the reverse biased side, C_r, can be written as

$$C_f = \frac{K}{(V_{do} - V_T - V_1)^{1/2}} \tag{33}$$

and

$$C_r = \frac{K}{(V_{do} - V_T + V_2)^{1/2}} \tag{34}$$

respectively, while the total capacitance is

$$C = \frac{C_f C_r}{C_f + C_r} = \frac{K}{(V_{do} - V_T - V_1)^{1/2} + (V_{do} - V_T + V - V_1)^{1/2}} \qquad (35)$$

In these expressions K is a constant with units $pFV^{1/2}$. Direct contributions to C from interface states are assumed negligible at the high measurement frequency (1 MHz). Subtituting Eqns.(26) and (30), evaluated at V = 0 and (arbitrarily) T = 173 K, and setting the resulting expression equal to the measured capacitance at that temperature and bias - which is shown in Fig. 7 - we find that

$$K = 67.53 \ (pF \ V^{1/2}) \qquad (36)$$

To test the validity of this approach we have plotted in Fig. 8 the calculated capacitance-voltage relationship at T = 173 K from Eqn.(35) together with the measured values from Fig. 7, and find a surprisingly close agreement. The maximum deviation at the highest bias voltage is only 5%, and in fact, the actual difference is less when we consider that the upward bending in the measured C-V curves displayed in Fig. 7 is due to a capacitance measurement error resulting from grain boundary conduction (an in-phase component) at the higher bias voltages.

From the Schottky barrier capacitance for uniform doping, given by[18]

$$C_{SB} = A\left[\frac{q \varepsilon_s N}{2(V_{do} - V_T - V)}\right]^{1/2} \qquad (37)$$

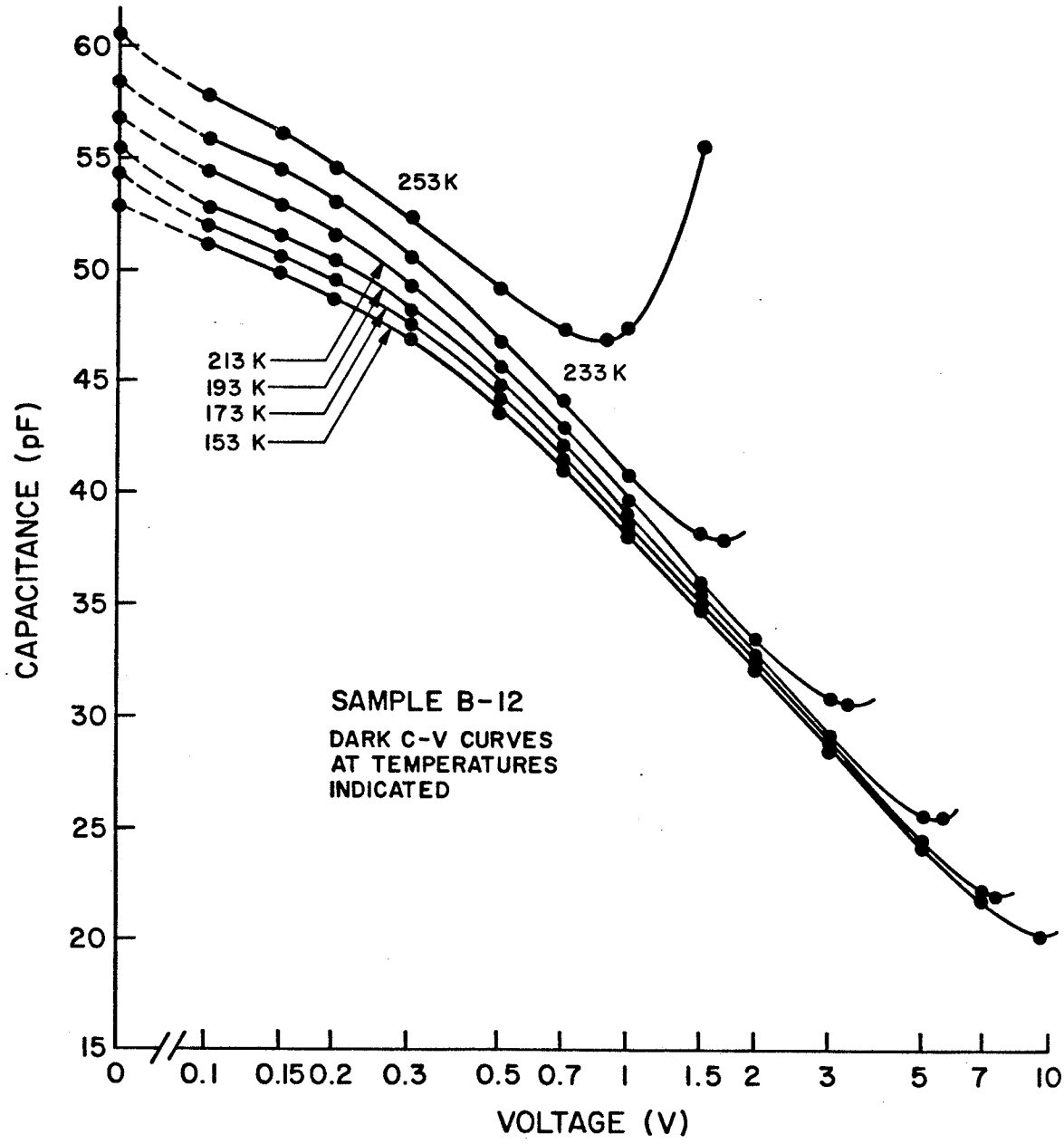

Fig. 7 Dark capacitance vs voltage at various measurement temperatures.

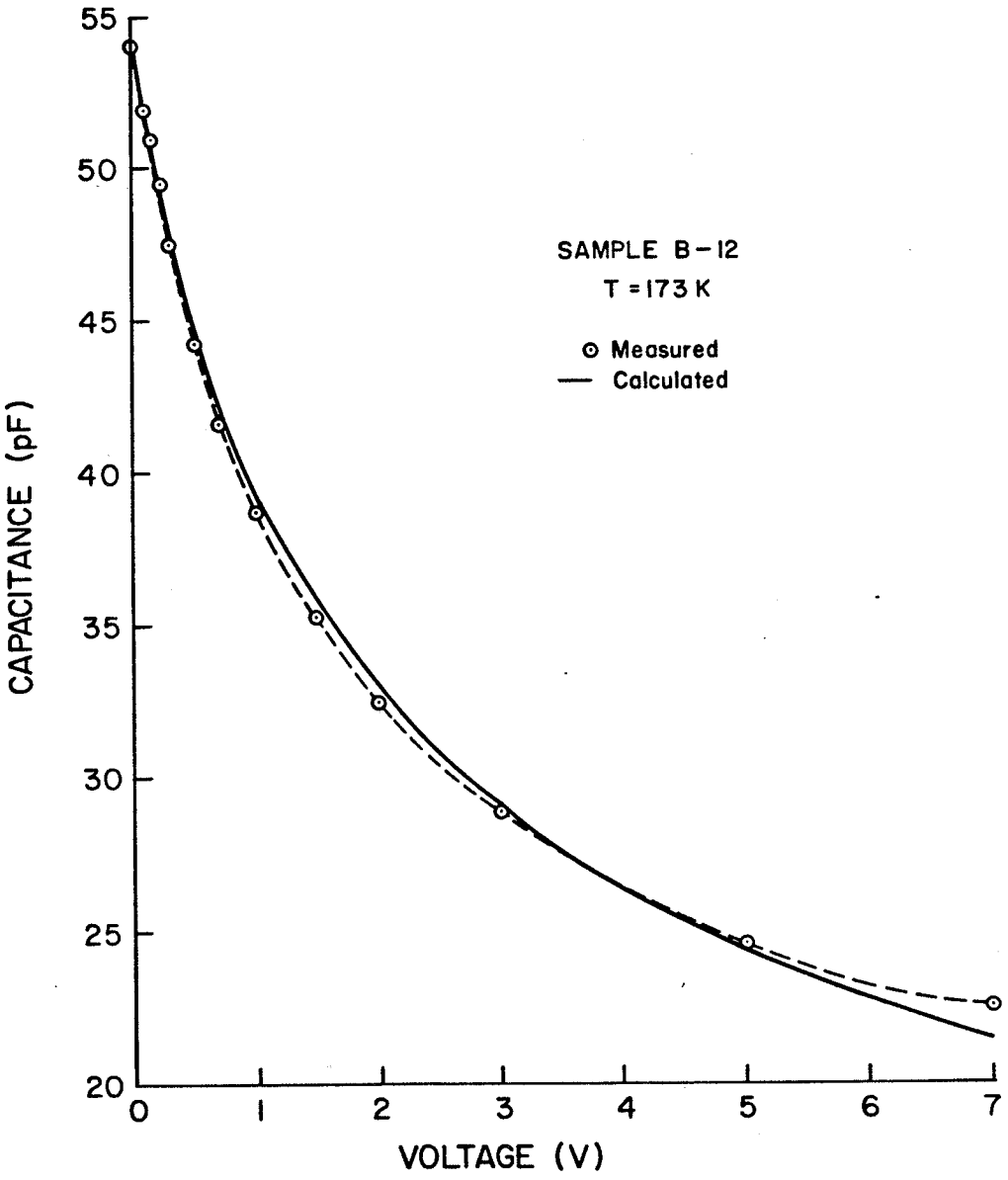

Fig. 8 Comparison of C-V curves of sample, and model having uniform doping and same zero bias capacitance. $V_1 = 0.07V^{1/2}$ was used.

we find

$$N_a \simeq 8.6 \times 10^{15} \quad (cm^{-3}) \tag{38}$$

Repeating the procedure for other temperatures yields values scattered within 7%. Note also that this value is significantly different from the published[7] bulk doping concentration $N_a = 3 \times 10^{15}$ cm^{-3}. The increased doping concentration near the grain boundary is attributed to impurity decoration of dislocations[19], i.e. the grain boundary tends to act as a diffusion sink for the boron atoms in the melt during the fabrication of the polycrystalline material.

Equation (37) affords an alternative method to determine the zero bias equilibrium diffusion potential $V_{do}(T)$ if the doping near the grain boundary is known and constant. By setting $V = 0$ and C_{SB} to twice the measured grain boundary capacitance, Eqn.(37) can be solved for $V_{do}(T)$.

Next, we wish to determine how the diffusion potential at $t = 0+$ (V_d in Fig. 3) depends on the applied bias at $t = 0^-$. The grain boundary capacitance under bias is given by Eqn.(35) which we repeat here in the form

$$C_{(V,\ t = 0^-)} = \frac{K}{(V_{do}-V_T-0.07V^{1/2})^{1/2} + (V_{do} - V_T + V - 0.07\ V^{1/2})^{1/2}} \tag{39}$$

Under zero bias, but with excess charge in the interface states, the capacitance at $t = 0^+$ is found by setting $V = 0$ and replacing V_{do} with V_d in Eqn.(39), which yields

$$C_{(V = 0,\ t = 0^+)} = \frac{K}{2(V_d - V_T)^{1/2}} \tag{40}$$

As the excess charge does not diminish abruptly at $t = 0^+$ and no discontinuity in the capacitance is observed, we may equate Eqns.(39) and (40) and find

$$V_{d(t=0^+)} =$$

$$\frac{V}{4} + V_T + \frac{V_{do} - V_T - 0.07V^{1/2}}{2}\left[1+(1+V/(V_{do}-V_T-0.07V^{1/2}))^{1/2}\right] \tag{41}$$

The only quantity that remains to be determined is the droop in the Fermi level at the grain boundary under bias, ΔE_F, or the equivalent potential $\Delta\phi_F$. Exact values for $\Delta\phi_F$ are difficult to obtain, but based on numerical analyses available for the sample used in this study at bias voltages below 1.5 V[20], our approximation is that

$$\Delta\phi_F \simeq V_1/2 \tag{42}$$

6. Theoretical Results and Discussion

The values derived for the quantities N_a, E_{oo}, kT ln N_c/N_d (or equivalently, kT ln N_v/N_a), V_{do} (V,T), V_d(V,T), V_1(V) and $\Delta\phi_f$(V) for our sample B-12 were used to evaluate the (normalized) thermal emission and thermionic-field emission rates, as given by Eqns.(13) through (15). The Pascal program for this computation is listed in the Appendix.

The ratios of thermionic-field to thermal emission, plotted in Fig. 9, show that the TFE component is dominant except for low bias and high temperature. It is instructive to compare these results with those for a single trap level at midgap, as shown in Fig. 3 of the previous chapter. At 100K and $N_dV_d \approx 10^{16}\,cm^{-3}V$ the ratio is approximately the same for both (≈12), but it drops off less rapidly for the distributed states at high temperatures. This effect is more pronounced at higher values of N_dV_d. This can be understood by observing that an increase in N_dV_d affects tunnelling only by reducing the width of the barrier.

Figure 10 illustrates how the total emission rate depends on (reciprocal) temperature and applied bias or N_dV_d product. Note that there is no exact one-to-one correspondence between the latter two quantities since V_d has a slight temperature dependence.

Comparison with Figs. 4 and 5 in the previous chapter indicates that, for $N_dV_d \approx 10^{16}\,cm^{-3}V$ and over the 100 - 300K temperature range, a 7 orders of magnitude variation is found for emission from shallow traps (E_c - 0.2 eV), but a 17 orders of magitude variation for deep traps (E_c - 0.55 eV). In contrast, we find for distributed traps a variation of 14 orders of magnitude, suggesting that for the rela-

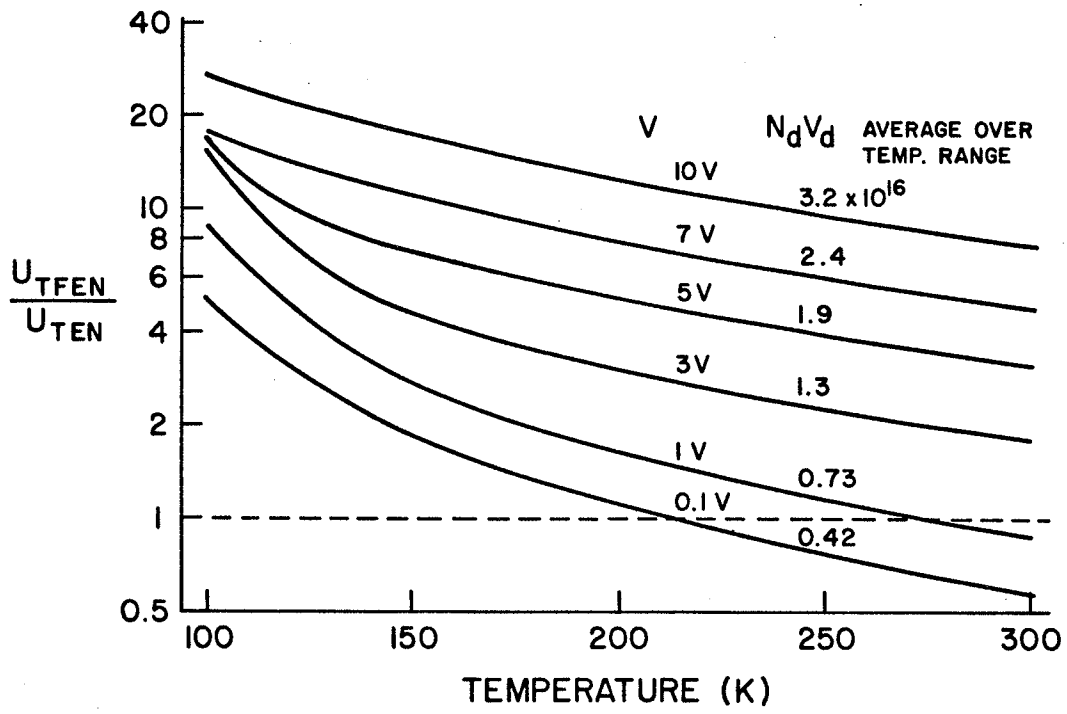

Fig. 9 Calculated ratio of normalized thermionic-field emission rate to normalized thermal emission rate vs temperature with bias voltage as parameter. $N_a = 10^{16}$ cm^{-3}; $\tau_o = 10^{-12}$ s.

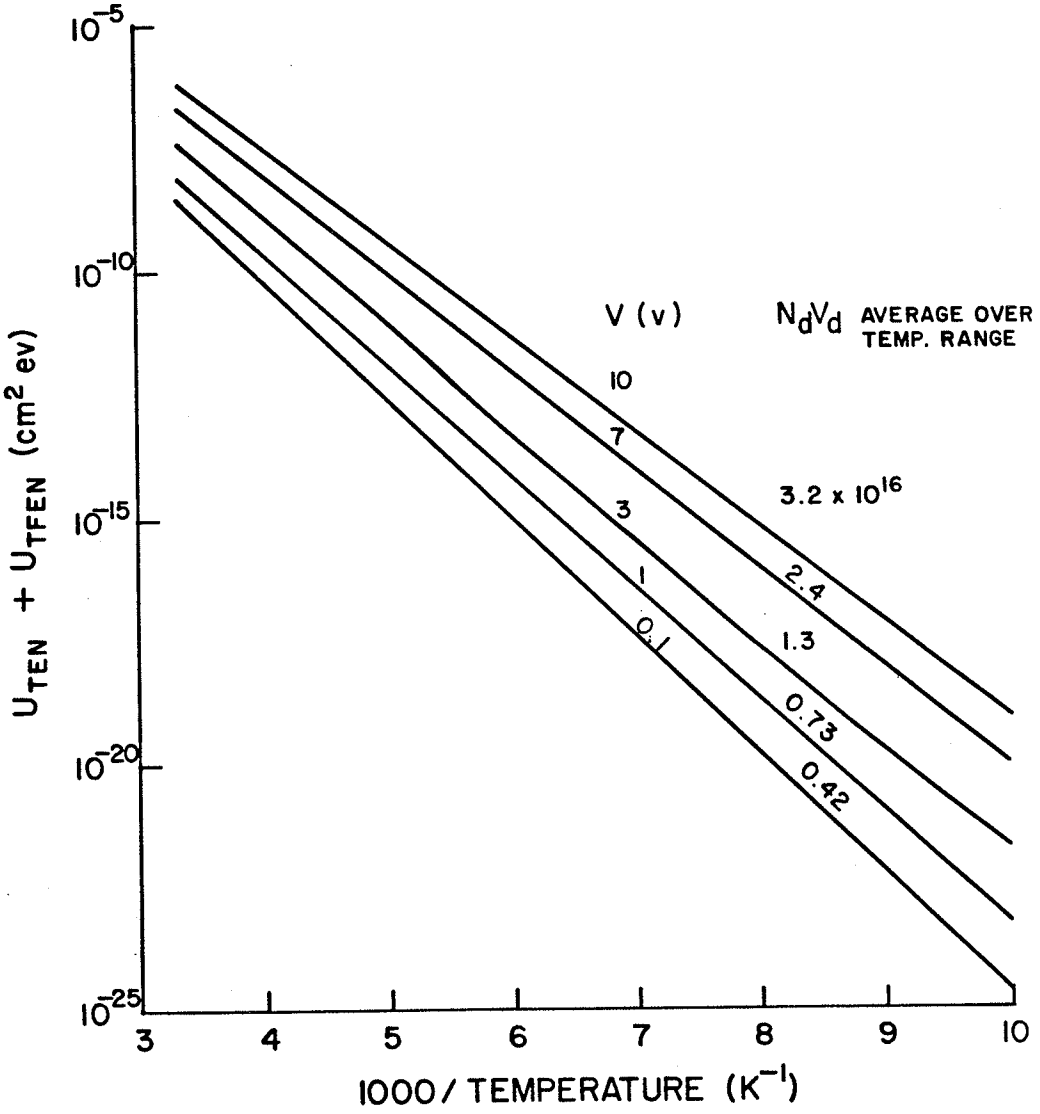

Fig. 10 Calculated normalized total emission rate vs temperature with bias voltage as parameter. $N_a = 10^{16}$ cm^{-3}; $\tau_o = 10^{-12}$ s.

tively low bias for this case (≈ 2 V, with $V_d \approx$ 1 V at t = 0^+) we are observing emission primarily from deep traps, as expected.

7. Experimental Results and Discussion

Some of the raw data from the experiments conducted, as outlined in section 2, Figs. 2 and 3, is presented in Fig. 11. The strong temperature dependence of the release rate of excess grain boundary charge is evident from Fig. 11(a). The total charge in the grain boundary is inversely proportional to the measured capacitance for spatially uniform doping concentration (Eqn.(11)). Note that the initial total grain boundary charge is the same for the cases shown, although the final values wil be different due to the temperature dependence of the zero bias diffusion potential.

In Fig. 11(b) we plot the capacitance transients at the same temperature for different initial values of the grain boundary charge. Observe also that the charge decay rates at a given amount of charge depends on the initial charge. This result indicates that the decay rate at a given temperature not only depends on the charge in the GB ($\propto$ 1/C) but also on the way in which this charge is distributed over the interface states. Thus, we would expect the charge associated with the Boltzmann tails of the occupation function to be emitted rapidly at t = 0^+.

Data such as that of Fig. 11 was reduced to the form shown in Fig. 12 where the charge decay rate is plotted versus the initial charge per unit area, Q_o.

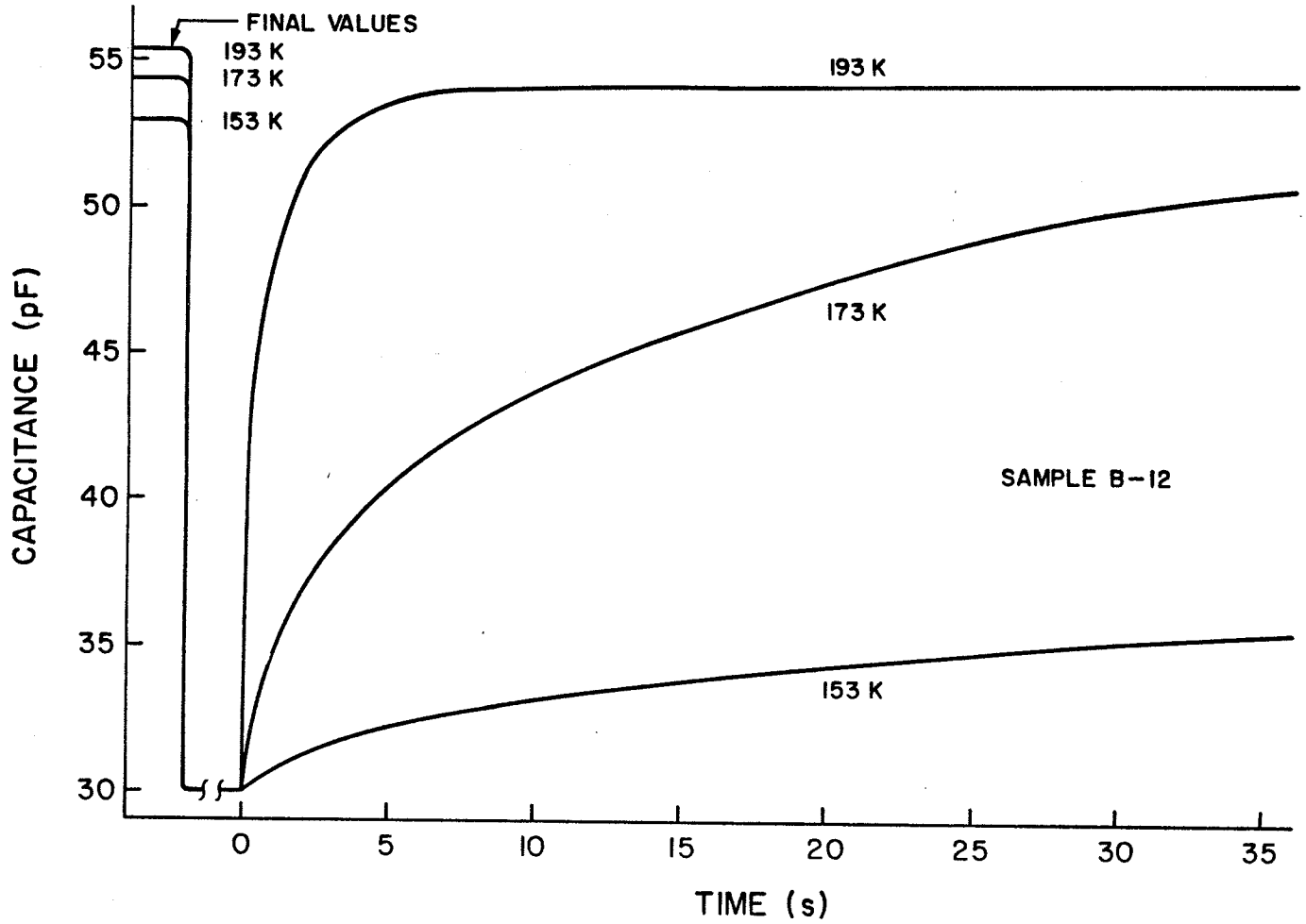

Fig. 11 (a) Capacitance transient curves for several temperatures. Same initial Q_{is} and C, but different final values as V_{do} is T dependent.

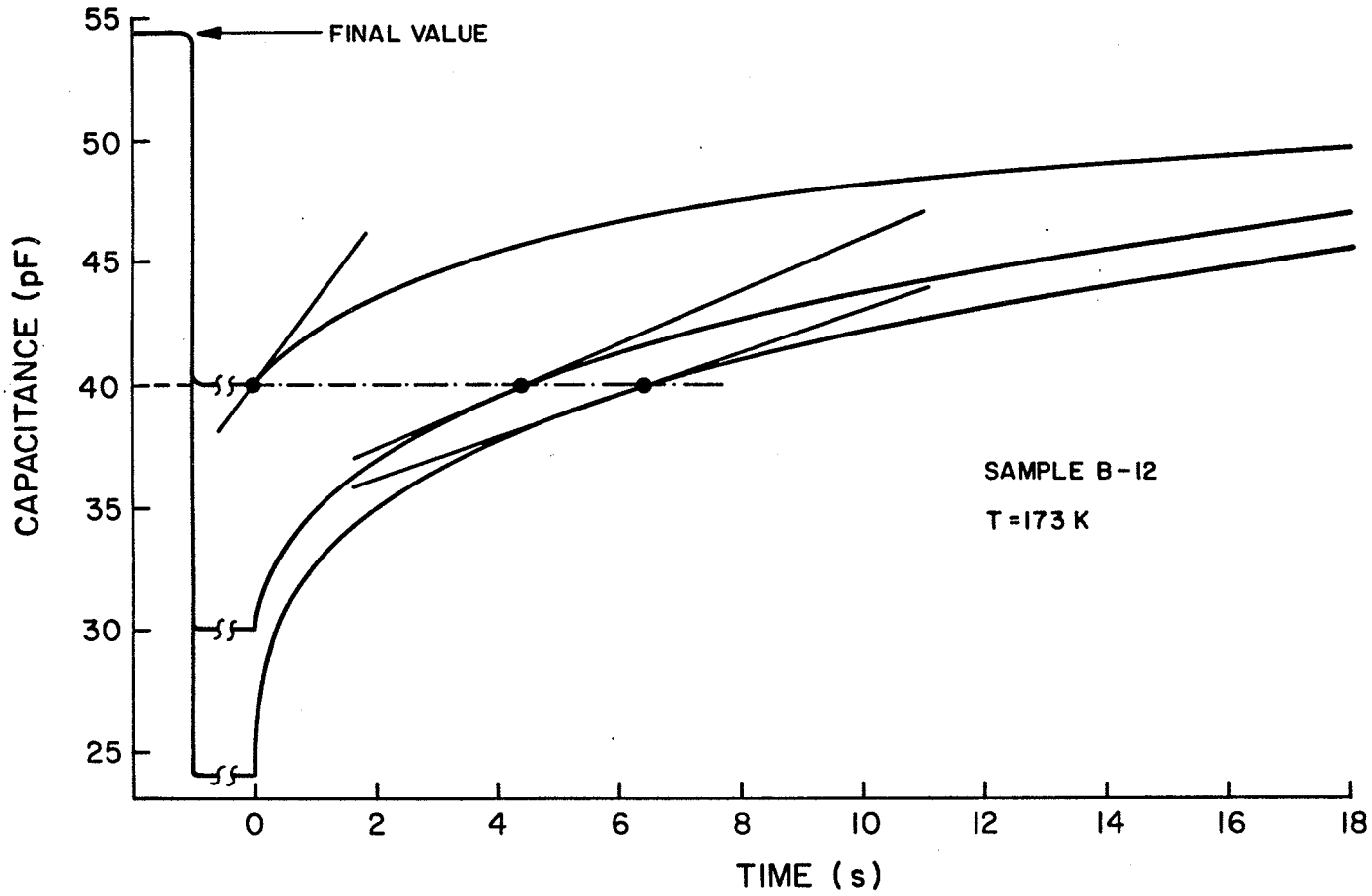

Fig. 11 (b) Capacitance transient curves at fixed temperature but different initial values of Q_{is}. Note different charge decay rates at same value of capacitance.

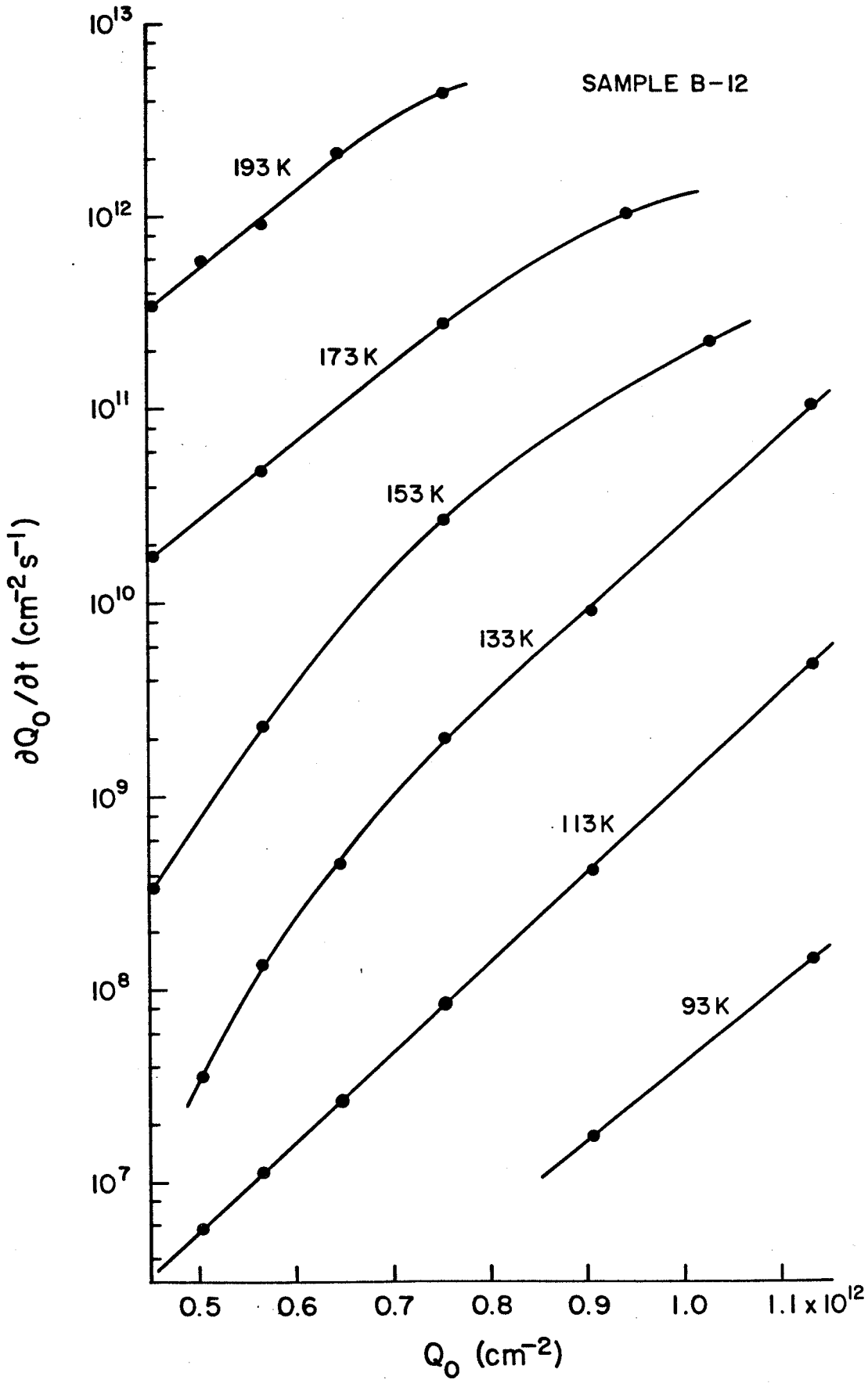

Fig. 12 Charge decay rate as a function of initial charge per unit area Q_o, deduced from capacitance recovery measurements according to Ref. 1.

According to Ref. 1, and subject to the following constraints i) charge decay according to SRH thermal emission theory, ii) a constant $N_{is}(E)$, at least above E_F, and iii) OK approximation to the Fermi function, we may derive N_{is} from

$$\frac{\partial}{\partial Q_o} \ln \frac{-\partial Q_o}{\partial t} \Bigg|_{Q_o(E_1)} = \frac{1}{kT\ N_{is}} \tag{43}$$

where E_1 is the highest filled trap level at any t. This implies, contrary to our earlier observation, that the charge release rate at a given temperature depends on Q_o and not on the energy distribution of Q_o.

Thus, in accordance with (43), the interface state density at Q_o follows from the slope of $\ln(-\partial Q_o/\partial t)$ vs Q_o.

The energy level E_1, relative to E_c, or E_v in the p-type case, may be found by plotting $-(\partial Q_o/\partial t)/kT$ (for a particular Q_o but at different temperatures) against 1/kT on a logarithmic scale. If a straight line results then its slope equals the energy sought.

However, the large temperature range in our study (5x larger than that of Ref. 1) resulted in substantial deviations from a straight line, and more so for decreasing values of Q_o. In the summary table below we have given two values for $E_1 - E_v$. The first, $(E_1 - E_v)$ all T, represents a best straight line fit over the entire temperature range, while the second, $(E_1 - E_v)$ some T, was determined from the largest collection of at least three approximately collinear points.

Table 1. Summary of results according to Ref. 1

$Q_o(cm^{-2})$	(E_1-E_v)allT(eV)	(E_1-E_v)someT(eV)	N_{is}^* avg	N_{is}high	N_{is}low
5×10^{11}	0.288	0.403	6.2×10^{12}	9.6×10^{12}	3.7×10^{12}
7.5×10^{11}	0.238	0.233	8.7×10^{12}	12.6×10^{12}	6.9×10^{12}
10^{12}	0.171	0.176	9.3×10^{12}	14.8×10^{12}	8.5×10^{12}

* all N_{is} in $cm^{-2}eV^{-1}$

We turn now to the interpretation of the experimental observations of Fig. 12 in terms of the complete theory of the total emission rate, including thermionic-field emission, as outlined in section 2, and which was calculated in section 6 as the emission rate per interface state and unity τ_o.

The experimental emission rates in Fig. 12 should correspond to $U_{TOT} \times N_{is}/\tau_o$. Comparison of experiment and theory for an assumed $\tau_o = 10^{-12}$ s at 193 K yields the interface state distribution shown in Fig. 13 by the solid line. Approximately the same interface state distribution is obtained for the somewhat lower temperature of 173 K. However, if this process is continued over the entire experimental temperature range it becomes clear that the emission rates at the lowest temperatures is well in excess of the theoretical predictions.

While this could be the result of a τ_o which increases sharply with declining temperature, there appears to be no physical basis for such a hypothesis. Instead, we interpret our observations as resulting from a decrease of the activation energy of interface states for substantial temperature decreases. The discrepancy between theoretical values and those arising from Fig. 12 implies an experimental emission rate which is too large by a factor of approximately 10^6 at

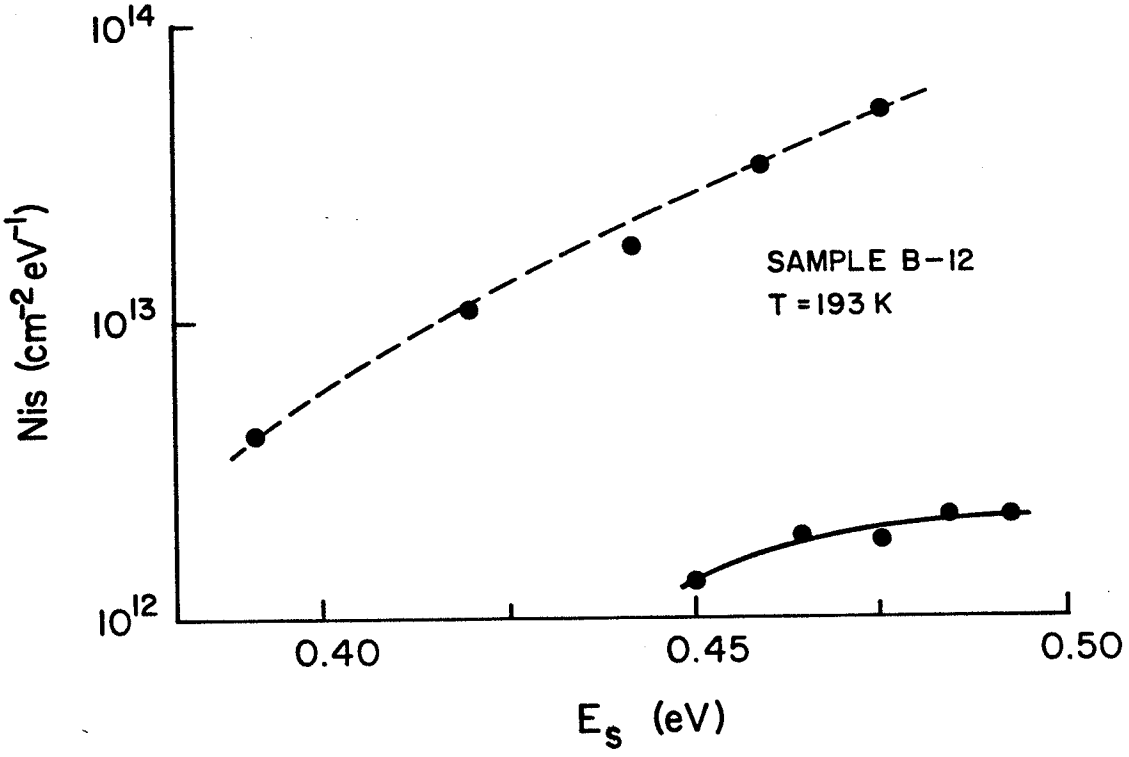

Fig. 13 Grain boundary interface state density vs energy in the band-gap, measured from valence band edge. Dashed line shows erroneous result when neglecting $\Delta\phi_F$ and using Eqn.(6a), as in earlier worker's treatments, rather than Eqn.(6).

93 K. This implies a reduction ΔE in the activation energy, given by $\exp(\Delta E/kT) = 10^6$, or $\Delta E \simeq 14\ kT \approx 0.1$ eV at 93 K.

There are physical reasons to expect such a decrease in the activation energy for interface state emission at the lower temperatures. Contraction of the crystal will be most pronounced at the grain boundary. Such a contraction of the potential well for interface states, based upon elementary wave mechanical arguments, would cause an increase in oscillation frequency for these states and hence, a reduced activation energy for emission out of the potential wells. This, in turn, implies a modest increase in τ_o, but the overwhelming increase in the emission rate is a consequence of the reduced activation energy.

Comparing the results for N_{is} by the present method with those obtained using the treatment of Ref. 1, we observe that the neglect of thermionic-field emission overestimates the interface state density. This is due to an underestimation of the emission rate. Similar arguments apply to the energy range of the interface states obtained by the two methods.

8. Conclusions

In this chapter previous treatments of grain boundary interface state emission have been extended to include a rigorous treatment of states distributed in energy and of thermionic field emission from these states. Comparison with experimental observations of transient capacitance measurements have indicated that the interface state distribution at grain boundaries exhibits a temperature dependence. A physical argument, based upon non-uniform contraction of this type of material, substantiates this observation.

Interpretation of the experimental data in terms of earlier theoretical treatments has been shown to lead to erroneous estimates of both the density and the energy distribution of these states.

It is concluded that transient capacitance characteristics as well as transport measurements, as discussed in the previous chapter, must be interpreted by a model which takes full account of thermionic field emission.

Semiconductor interfaces in other types of device structures are expected to be subject to the same conclusions, particularly when one deals with high doping concentrations and bias voltages.

It has also been shown that, in polycrystalline silicon, there may be a significant difference between the doping concentration in the bulk (inside the grain) and that at the grain boundary.

References

1. C.H. Seager, G.E. Pike and D.S. Ginley, Phys. Rev. Lett., 43, 532-535, 1979.

2. A. Broniatowski and J. -C. Bourgoin, Phys. Rev. Lett., 48, 424-427, 1982.

3. A.W. De Groot, G.C. McGonigal, D.J. Thomson and H.C. Card, accepted for publication in J. Appl. Phys.

4. H.F. Matare, Defect Electronics in Semiconductors, John Wiley, New York, 1971.

5. F.A. Padovani and R. Stratton, Solid St. Electron., 9, 695, 1966.

6. I. Lundström and C. Svensson, J. Appl. Phys., 43, 5045, 1972.

7. G.C. McGonigal, D.J. Thomson, J.G. Shaw and H.C. Card, accepted for publicaton in Phys. Rev. B.

8. G.E. Pike and C.H. Seager, J. Appl. Phys., 50, 3414-3422, 1979.

9. C.H. Seager and G.E. Pike, Appl. Phys. Lett., 35, 709-711, 1979.

10. J.Y.W. Seto, J. Appl. Phys., 46, 5247-5253, 1975.

11. G. Baccarani, B. Riccò and G. Spadini, J. Appl. Phys., 49, 5565-5570, 1978,

12. H.C. Card, J. Appl. Phys., 52, 3671-3673, 1981.

13. W.E. Taylor, N.H. Odell and H.Y. Fan, Phys. Rev., 88, 867-875, 1952.

14. H.J. Leamy, et al. (Editors), Grain Boundaries in Semiconductors, 91, Materials Research Society Symposia Proceedings, Vol. 5, North Holland, New York, 1982.

15. N.D. Arora, J.R. Hauser and D.J. Roulston, IEEE Trans. on Electron Dev., ED-29, 292-295, 1982.

16. D.J. Thomson and H.C. Card, J. Appl. Phys., 54, 1976-1980, 1983.

17. J. Hilibrand and R.D. Gold, RCA Rev., 21, 245, 1960.

18. S.M. Sze, Physics of Semiconductor Devices, 371, John Wiley, New York, 1969.

19. K.V. Ravi, Imperfections and Impurities in Semiconductor Silicon, 221, John Wiley, New York, 1981.

20. J.G. Shaw, Numerical Analysis of Semiconductor Devices, Ph.D. dissertation, University of Manitoba, Winnipeg, 1983.

CHAPTER V

INEXPENSIVE CONTROLLED LOW TEMPERATURE APPARATUS FOR SEMICONDUCTOR STUDIES*

* The contents of this chapter have been submitted for publication in IEEE Transactions on Instrumentation and Measurement.

1. Introduction

Many research projects on semiconductor materials and devices require the use of a cryogenic chamber for low temperature measurements. Examples are deep level transient spectroscopy (DLTS)[1,2] and thermally stimulated current (TSC)[3] experiments. In some cases a particular temperature must be maintained for some time while in other cases, such as TSC, a (usually linearly) time-varying temperature is employed.

A commonly used apparatus for low temperature experiments consists of a brass chamber which is evacuated to avoid condensation of water vapour onto the sample upon cooling by immersion in liquid nitrogen (LN). Such a closed system has several disadvantages: it requires a (frequently noisy) pump, the sample is not easily accessible since the vacuum must first be broken, the unit has a large thermal mass, the quartz window used for measurements under illumination has a tendency to fog over, and it is difficult to quickly establish and then maintain a constant arbitrary temperature for extended periods. In addition, significant temperature gradients may exist over the sample and between the sample and the thermocouple used to measure the temperature, particularly under transient conditions (e.g. linear ramp) because heat transfer is based on conduction.

The low temperature apparatus described in this paper offers several advantages over the conventional system, and may be of interest to many other workers in the field. It has a small thermal mass and no vacuum pump is required since the sample is immersed in nitrogen gas which prevents water vapour condensation. It is an open system which provides direct access to the sample and there is no window that could

fog over, while any filter that may be required is situated such that this problem does not occur. Stable temperatures down to -193°C (80K) are attainable. Linear temperature changes (or other temperature profiles) may be effected by applying an appropriate reference temperature input signal. A uniform temperature is obtained as heat transfer is based on turbulent convection, and finally, the unit is easy to construct from inexpensive materials.

The block diagram of the system is shown in Fig. 1. The basic cooler consists of two adjacent compartments made of styrofoam, an excellent thermal insulator. The first compartment contains a heat exchanger made from a copper tube wound into a coil which is then immersed in liquid nitrogen (LN).

Nitrogen gas is fed through the coil under pressure and into the second compartment which contains the sample, a thermocouple and a heater coil.

The thermocouple signal is fed to a Fluke 2100A digital thermometer which also provides an analog output. This output signal, together with a temperature reference signal representing the desired temperature are the inputs to a simple electronic control system whose output is the heater voltage.

2. Mechanical Construction

The two adjacent chambers, shown in Fig. 2, form a single unit made from part of a Fisher Scientific styrofoam shipping container for four 1 gallon acetic acid bottles. In addition to having a low thermal conductivity and specific heat styrofoam is also an easily workable material.

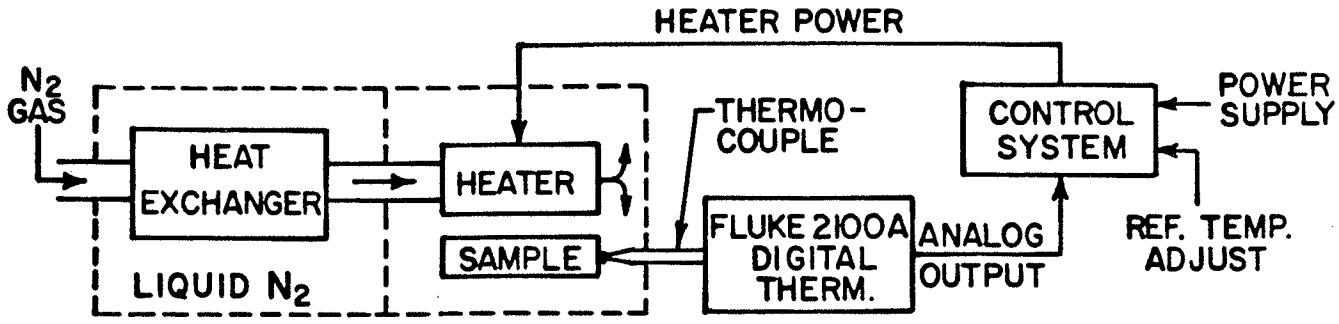

Fig. 1 Block diagram of the temperature controlled cryogenic system.

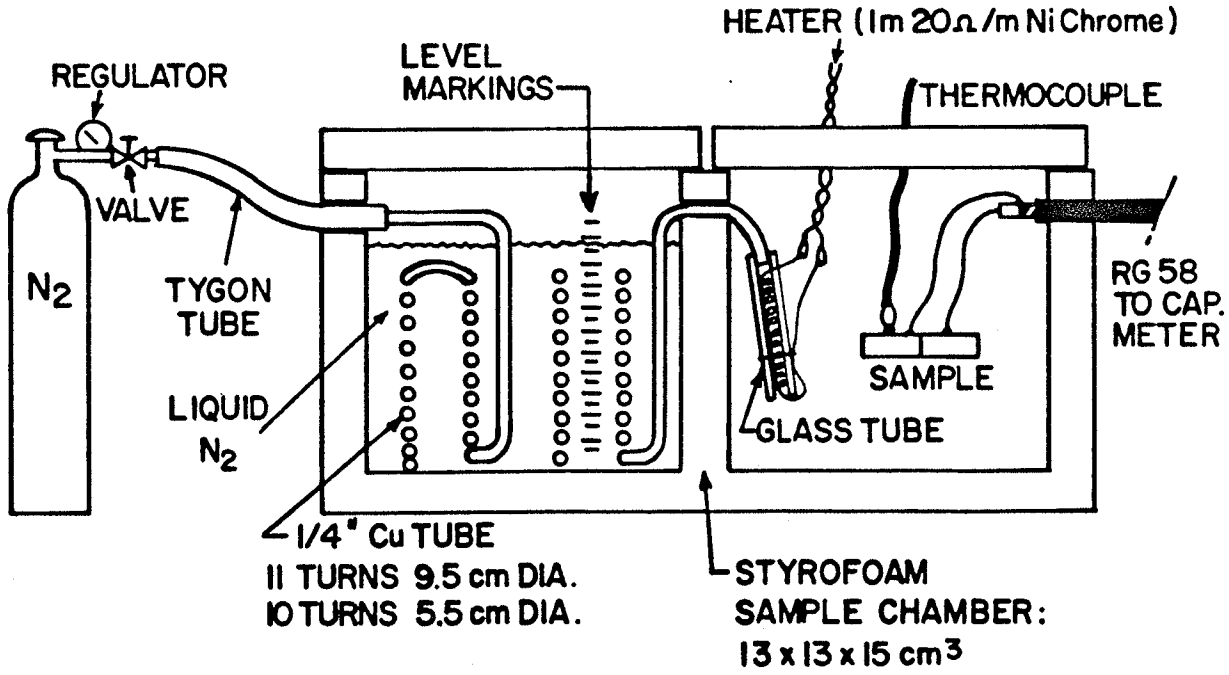

Fig. 2 Cross-sectional view of the low temperature apparatus.

Nitrogen gas is fed from a standard high pressure cylinder through a pressure reduction valve and an ordinary gas valve to the heat exchanger via a Tygon tube which enters the LN compartment above the LN level.

The heat exchanger is made from two lengths of copper tube which were wound separately and subsequently soldered together. Dimensions are indicated in Fig. 2.

The heater coil was wound from 1 m of 20 Ω/m Nichrome wire and placed into a 10 cm glass tube which just fits over the 1/4" copper tube. One end of the heater wire emerges from the bottom end of the glass tube and is tied to it with a piece of copper wire. The other end is brought out through a cut in the tube, made with a diamond saw. The assembly was then fastened to the copper tube with epoxy which was also used to fill in the cut, so that all of the low-temperature nitrogen gas must flow over the heater wire.

The ends of the heater wire are connected to a twisted pair of 14 gauge copper wire by means of a "press fit" since Nichrome does not solder. The twisted pair, the thermocouple wire and the electrical connections to the sample are brought out through the wall near the top of the sample chamber.

The situation illustrated in Fig. 2 has been employed for grain-boundary capacitance measurements. The RG58 cable provides a constant stray capacitance, which has been measured and corrected for.

Details of the sample mounting are shown in Fig. 3.

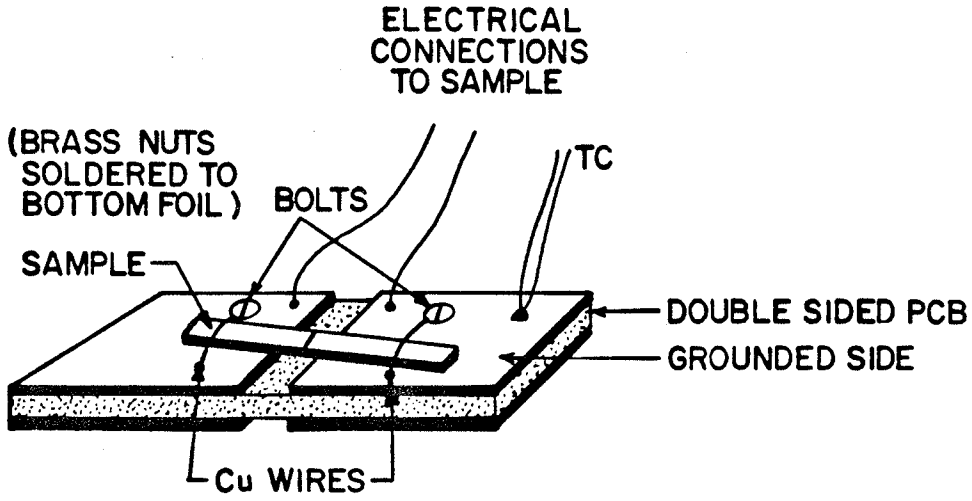

Fig. 3 Sample mounting arrangement for grain-boundary experiments.

3. Control Circuit

The circuit diagram of the controller is shown in Fig. 4. It comprises a 741 operational amplifier connected as a differential amplifier which drives a Darlington connected transistor pair which, in turn, drives the heater coil. The two input signals are the analog output from the thermometer (Fluke 2100A) and the reference temperature voltage.

The gain of the circuit (defined here as R_7/R_6) can be adjusted by means of R_6, while the reference temperature is set with R_3 in the range from 22 mV to -180 mV, which corresponds to a temperature range from 22 to -180°C in accordance with the calibration of the thermometer's analog output: 1 mV/°C and 0V representing 0°C. Alternatively, the reference temperature input can be switched to an external signal which may be time-varying.

The internal reference voltage source is stabilised against power supply fluctuations by the Low Voltage References D_1 and D_2.

Each transistor has its own heatsink: the small signal transistor has a standard clip-on heatsink while the power transistor (NJE 520) is bolted onto a copper plate, with silicone grease on the contact area providing good thermal conduction.

The circuit requires a ±8 V power supply at less than 10 mA, and although the actual voltage is not critical it should be reasonably well regulated. A separate 10-25 V supply, capable of providing 1.25 A maximum at 25 V, is used for the heater. Notice also that the ground return for the heater current is kept separate from that for the rest of the circuit to avoid undesirable coupling.

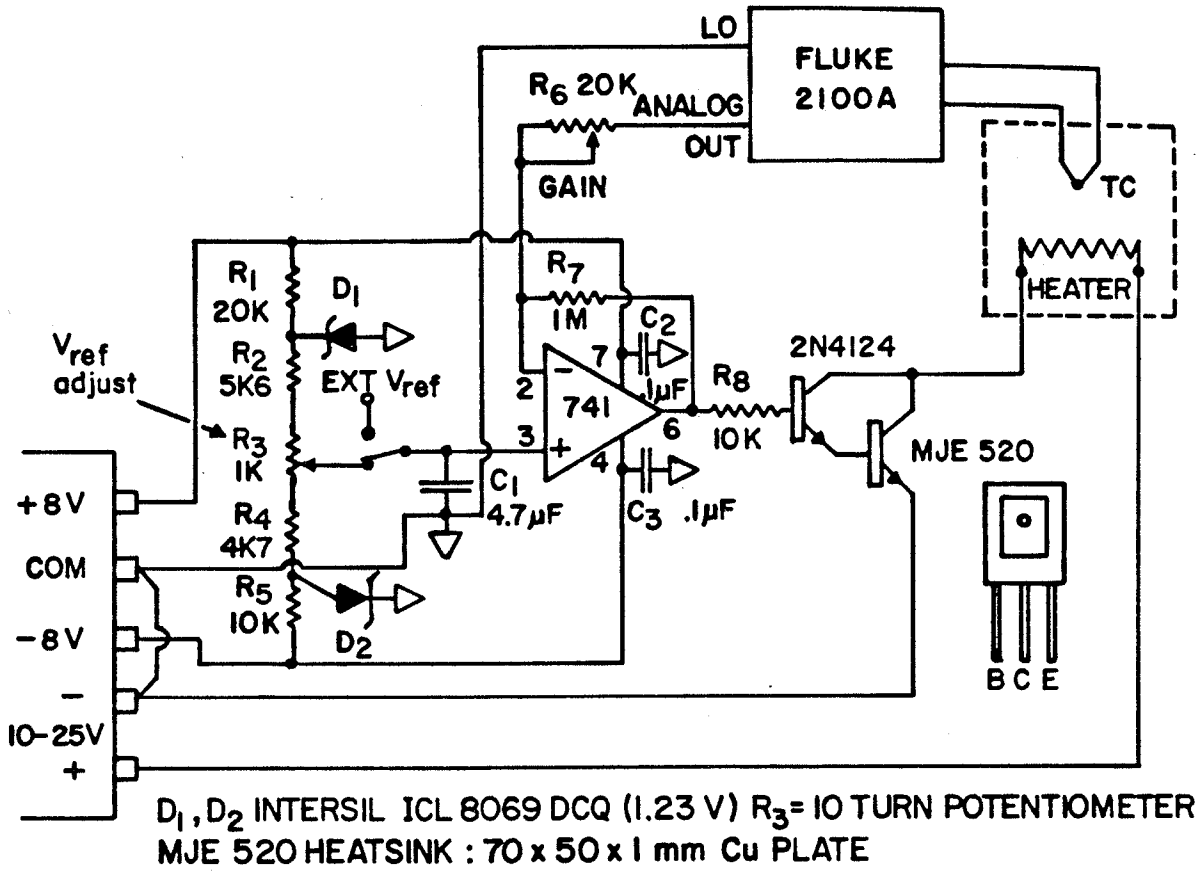

Fig. 4 Schematic diagram of the control system and interconnections to other system components.

The Joule heating in the coil is approximately proportional to the square of the difference between the measured temperature (analog out) and the reference voltage when $V_{ref} > V_{analog}$, and is zero otherwise. The maximum heat generation rate is, of course, limited by the heater supply voltage.

4. Performance

The factors that determine the steady-state temperature in the sample chamber are, in decreasing order of importance, the nitrogen gas flow rate, heat generation in the heating coil, LN level in the heat exchanger chamber, and ambient temperature.

Figure 5 shows temperature as a function of time for various nitrogen gas flow rates with the heater switched off and with the LN level at maximum (level markings were written on the inside of the heat exchanger chamber).

The lowest temperature obtained was -193°C (80 K) although this requires a high gas flow rate, beyond the capability of the gauge used to obtain the data of Fig. 5, and frequent replenishing of LN.

For proper operation of the system it is, of course, necessary that the desired temperature, as set by V_{ref}, is higher than the uncontrolled temperature but still within the heater capability. It is therefore useful to monitor the heater voltage which should always lie between zero and its maximum value (except under transient conditions, e.g. when V_{ref} is changed significantly), and if necessary the nitrogen gas flow rate should be increased or decreased, respectively.

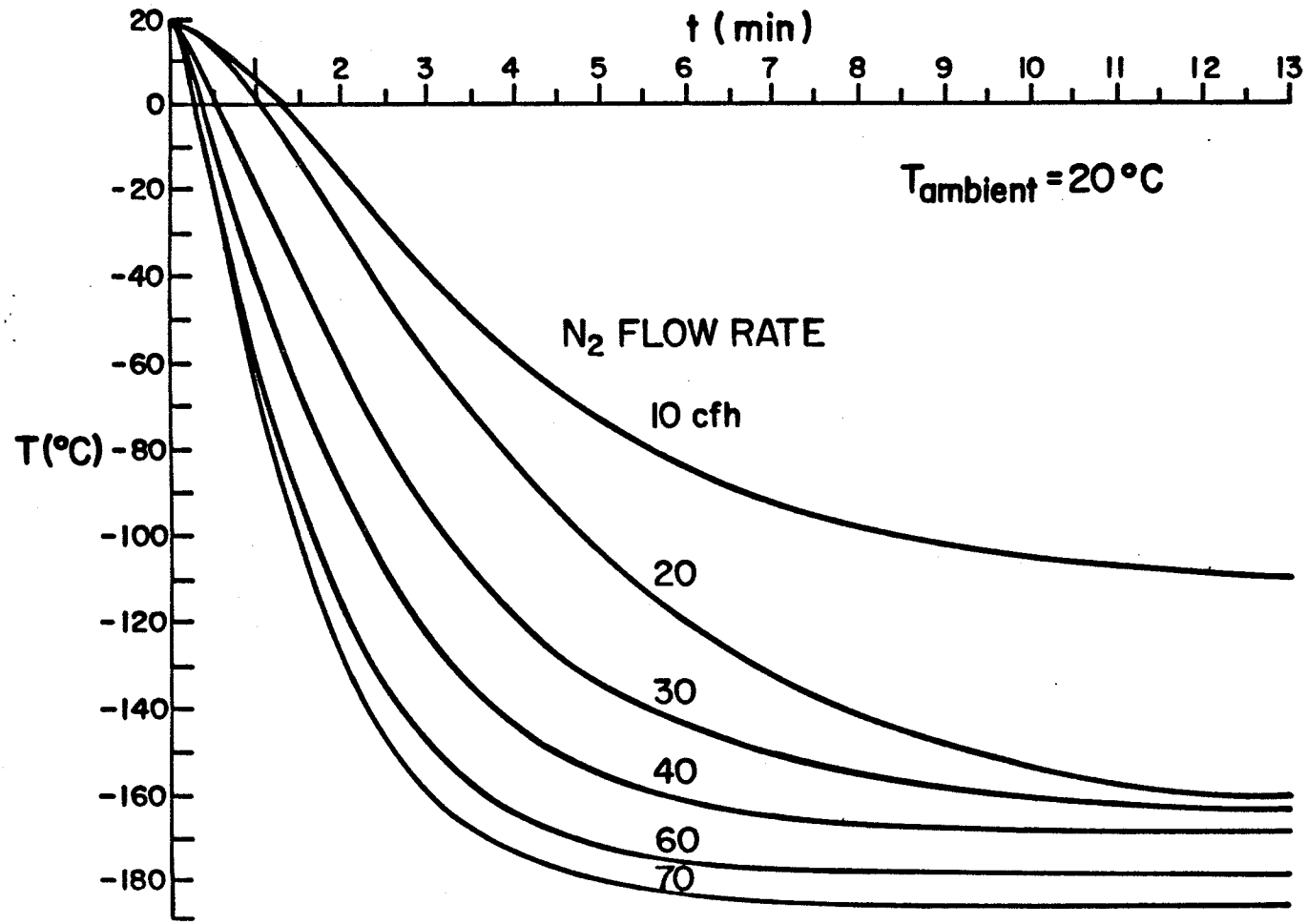

Fig. 5 Temperature vs time at various nitrogen gas flow rates (in cubic feet per hour) and with the heater disabled.

The main criteria for evaluation of system performance are: a) how little does the actual temperature deviate from the desired temperature - any constant offset can be taken into account when setting V_{ref}, b) how well does the system compensate for disturbances (adjustment of N_2 flow; adding LN), and c) how well does the temperature track a time-varying V_{ref} - typically a linearly increasing signal.

There are two factors which limit the degree to which ideal system behaviour may be attained. The first one stems from the fact that the analog output signal from the Fluke thermometer is not a continuous variable, but instead, changes by 0.25 mV for every 0.4°C change in temperature. As a result, the gain of the control system must be limited in order to avoid limit cycles which, in turn, would prevent the temperature from settling to the desired value. Consequently, the temperature control cannot be as "tight" as one would prefer in some cases.

Secondly, a system with a significant amount of delay between application of a correction (heater voltage change) and the desired effect (adjusted temperature) has a tendency to overshoot, and to exhibit ringing in response to a sudden change of an input parameter, particularly for high gains. In extreme cases this leads to oscillation or limit cycling. Both effects are shown in Fig. 6.

Figure 7 shows the effect of decreasing the nitrogen gas flow rate: a transient towards a higher temperature followed by a steady-state value at a slightly higher temperature. This effect is in addition to any inherent offset, e.g. due to the operational amplifier and cut-in voltage of the Darlington pair.

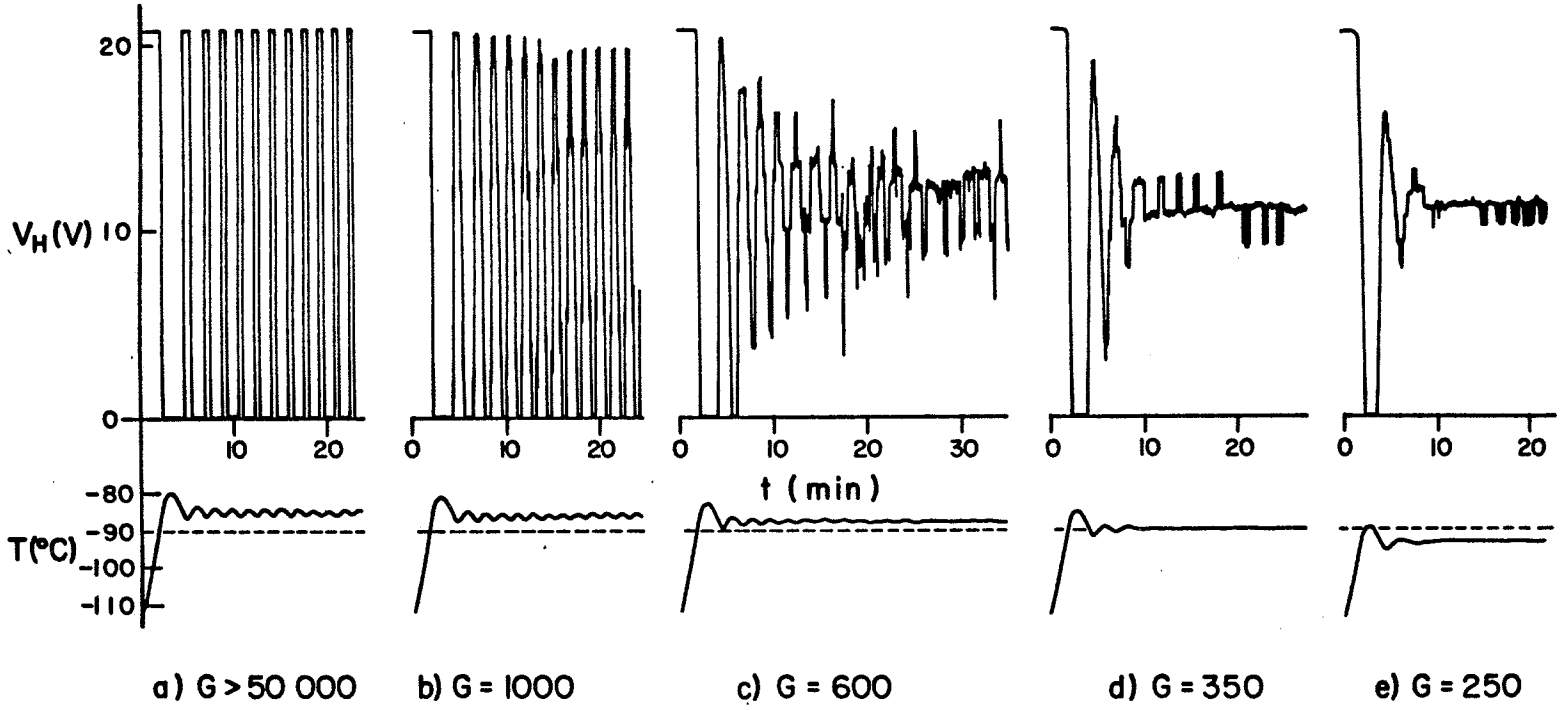

Fig. 6 Transient response of temperature and corresponding heater voltage for various gain settings. Nitrogen gas flow rate is 25 cfh, V_{ref} = -90 mV.

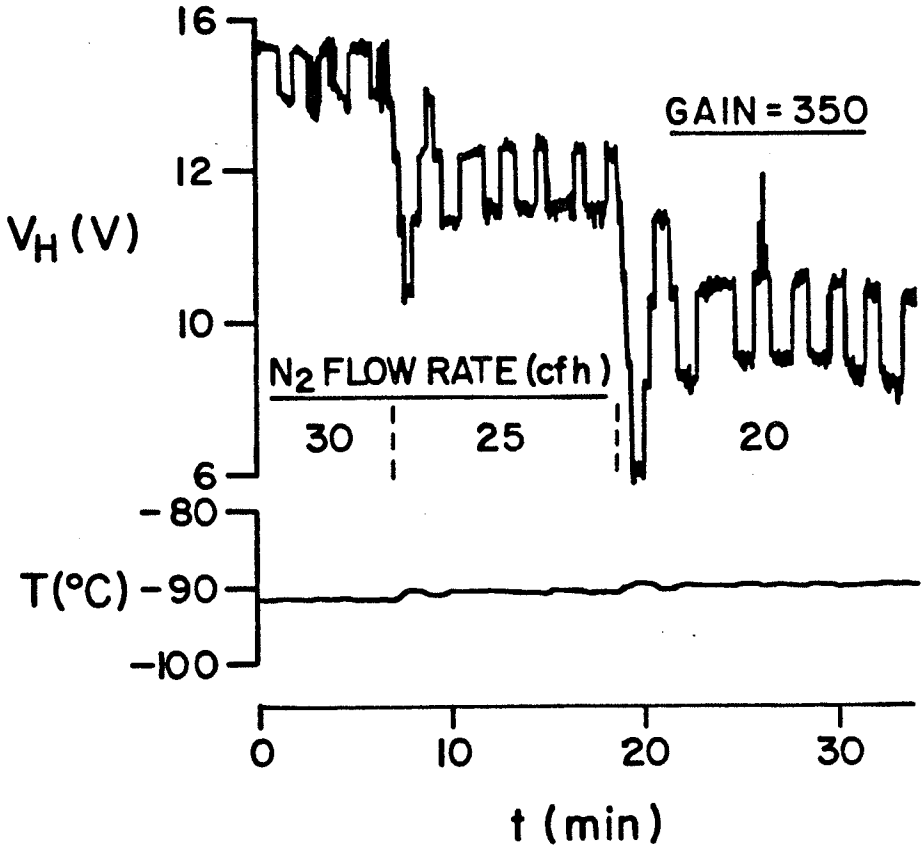

Fig. 7 Transient response of temperature and corresponding heater voltage for step changes in the nitrogen gas flow rate.

Similar effects occur when changing the LN level. Thus, when a very stable temperature over a long period of time is desired it is preferable to add small amounts of LN frequently rather than larger amounts occasionally.

The system response to a ramp input is shown in Fig. 8. It should be noted that, although the "steady-state" error increases with time, good linearity of the temperature is maintained after the initial transient has subsided. Of course, for slower ramps the subsiding LN level will partially compensate this effect.

It can be seen from Fig. 6 that a gain of about 300 gives optimum results in terms of settling time and temperature flutuations, which can in this case easily be maintained to within ± 0.5°C . The optimum figure for the gain will depend on the current gain of the Darlington pair and the heater supply voltage.

Using an accurate thermometer with a true analog output (i.e. continuous signal) would allow a higher gain to be used and result in an improved temperature stability and a diminished dependence of temperature on nitrogen flow rate and LN level.

Because of the inherent system delay it is not possible to entirely eliminate ringing resulting from shocks to the system.

For low temperature measurements under optical illumination the configuration depicted in Fig. 9 has proved useful. A filter can be suspended from the cover of the sample chamber by means of a holder made from stiff copper wire. The advantage of locating the filter inside the sample chamber is that condensation is avoided. If the light source must be situated close to the cover a piece of printed circuit board is used to dissipate most of the generated heat. This is necessitated by the low melting point of styrofoam.

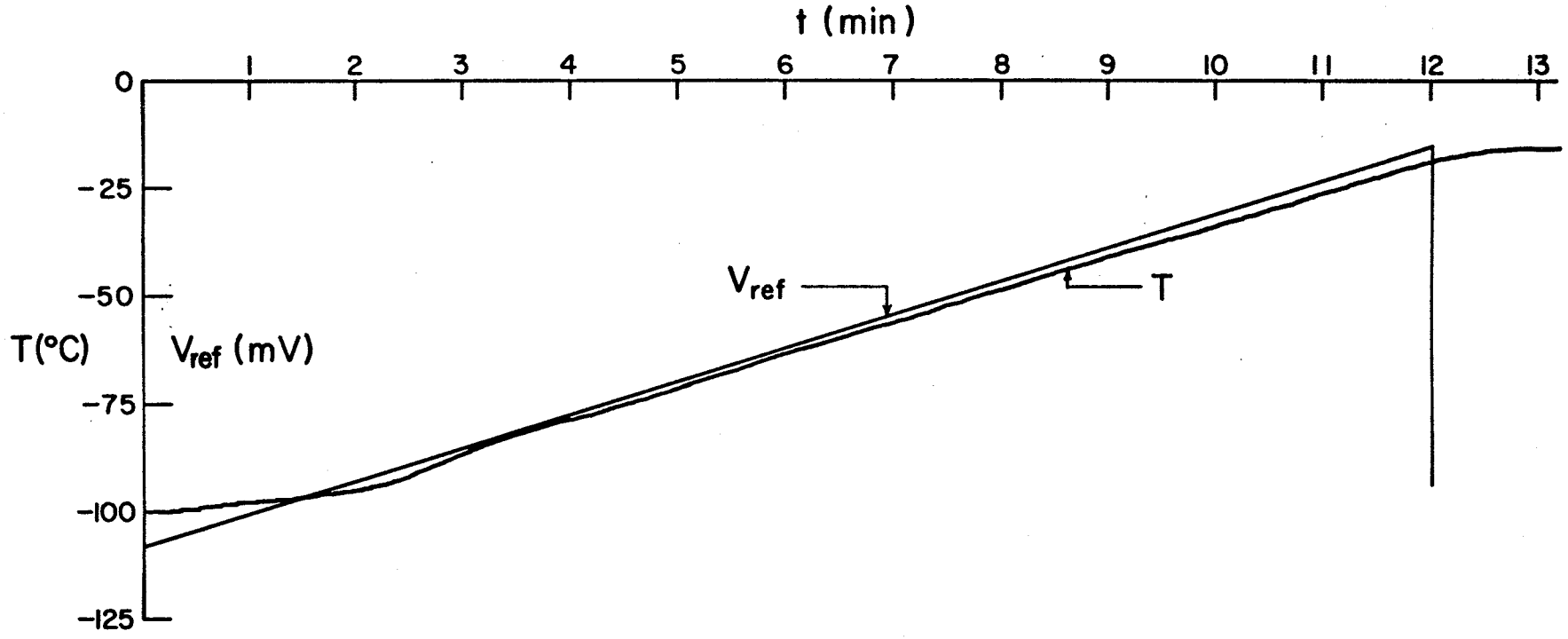

Fig. 8 Temperature vs time for a linearly increasing V_{ref} .

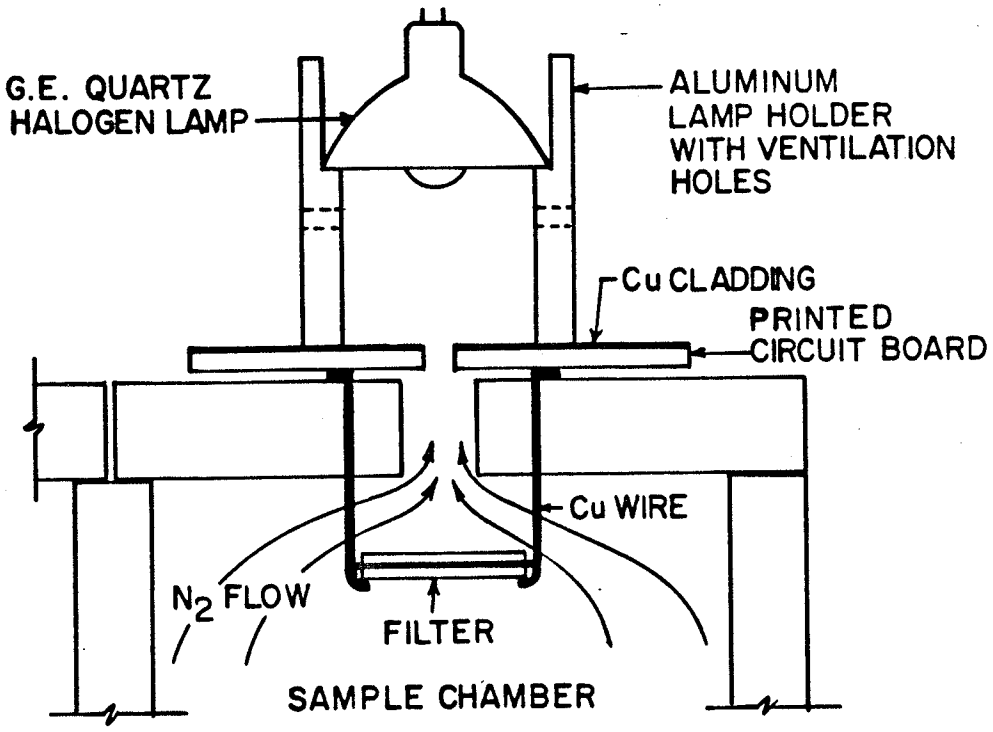

Fig. 9 Possible arrangement for low temperature measurements under optical illumination.

5. Conclusions

It has been shown that a controlled low temperature apparatus may be easily and inexpensively constructed from readily available materials costing less than $25.00. The complete system requires, in addition, a high-pressure cylinder of nitrogen gas with a regulator, a suitable quantity of LN, a thermometer with an analog output, and three power supplies (± ≈ 8V, 10-25V).

Temperature stability to within ± 0.5°C can be maintained and further improvement would be possible with a thermometer which provides a continuously-variable analog output signal.

Controlled temperatures from approximately -180°C to room temperature are readily obtained, while -193°C (80K) has been achieved with extreme nitrogen gas flow rates and continuous replenishing of LN.

Linearly varying temperatures (e.g. for DLTS or TSC measurements) of rates up to at least 4°C/min (at 20V heater supply) are possible, with a linearity better than 0.5%.

References

1. G.L. Miller, D.V. Lang, and L.C. Kimerling, Ann. Rev. Mater. Sci. 1977, 377.
2. F. Lau, H. Poth, and P. Balk, Solid-St. Electron. 23, 703 (1980).
3. B.L. Smith, Appl. Phys. Lett. 21, 350 (1972).

CHAPTER VI

RECOMMENDATIONS FOR FURTHER WORK

The studies presented in this thesis could be extended in several ways in order to further improve our understanding of defects in silicon. One of the interesting extensions would be to consider the effect of impurities, deliberately introduced into grain boundaries. (see, e.g. C.H. Seager and D.S. Ginley, Appl. Phys. Lett., 34, March 1979.) This procedure would be facilitated by the enhanced diffusion along these boundaries as opposed to bulk diffusion. Such studies are of importance, for example, in optimizing the behaviour of polysilicon interconnections in VLSI circuits.

Since no evidence was found in this study to suggest strongly energy dependent interface state densities, it might be interesting to investigate why emission rates depend so much on the charge distribution in the grain boundary for a given amount of charge (see CH IV, Fig. 11b).

A theoretical study of the temperature dependence of grain boundary interface state energy distributions, and the development of experimental procedures to test any resulting hypotheses is strongly recommended (see CH IV, section 8).

One of the parameters which is of prime importance in determining the characteristics of defect states in grain boundaries is the orientational mismatch between adjacent grains. In our study this mismatch angle was not under our control. However, recent work by J.P. Salerno and co-workers (Proc. 16th IEEE Photovoltaic Specialists Conference, Sept. 1982, pp 1299-1303) has demonstrated the possibility of growing GaAs bicrystals with predefined mismatch angles. The same

procedure could be applied to silicon bicrystals, thereby permitting the correlations between grain boundary interface states density and mismatch angle. Such a procedure would be helpful in relating these states to a particular bonding disorder.

Determination of interface state densities at the shallow energy levels is hampered by several problems. It is difficult to fill those states through current injection as E_s (in CH IV, Figs. 2 and 3) cannot be made arbitrarily small, and the emission rates from those states will be very high. In the literature, the interface state density is generally shown to vanish with energy in the direction of the majority carrier band. It may be possible to charge the shallow states by means of sufficiently short wavelength light and measure the discharge rate, after removal of the light, at very low temperatures. However, the high absorption that is to be expected at suitable wavelengths will complicate the quantitative interpretation of data obtained by this method.

APPENDIX

DESCRIPTION AND LISTING OF PASCAL PROGRAM FOR EVALUATION OF NORMALIZED COMBINED THERMAL EMISSION/THERMIONIC-FIELD EMISSION RATES

The Pascal program employed in this study, together with a sample output, is presented on pages 124-126.

The input data consists of the following:

a) constants

Permittivity of the semiconductor	EpSubS	in F m^{-1}
Effective mass of the majority carrier	Mlh	in kg
Doping concentration	Na	in cm^{-3}
Boltzmann's constant	k	in eVK^{-1}
Effective density of states in majority carrier band	Nv	in cm^{-3}

b) variables

Temperature in K, listed at the end (93 to 193 K) and put in TT: array [1..m], where m is the number of temperatures entered.

Applied voltages in V, listed at the end (0.115 to 9.0 V) and put in VV:array [1..n], where n is the number of voltages entered.

m and n are also entered in the *Main* program on the second page.

First, the following functions are computed:

Vl : fraction of applied voltage, V, appearing across forward biased side, from Eqn.(30);

Delta Phi : droop in the Fermi level, from Eqn.(42);

Vdo : equilibrium zero bias diffusion potential, from Eqn.(26);

Es: the energy difference between the majority carrier band at the grain boundary and the Fermi level at the grain boundary under applied bias, from Eqn.(15);

Note that the expression for E_s contains either $\ln(N_c/N_d)$ (n-type) or $\ln(N_v/N_a)$ (p-type) and <u>not</u> $\ln(N_a/N_v)$, as in either case the contribution to E_s must be positive.

Vd : the zero bias diffusion potential at t = 0+ after application of a bias V for t < 0.

Note that for V = 0 this reduces to its equilibrium value V_{do}. Eqn.(41);

Next, the normalized thermal emission component Uten is calculated from Eqn.(14).

Ea : establishes the lower limit of the outer integral in Eqn.(15).

U : is the Heaviside step function.

FE : is the integrand of the inner integral in Eqn.(15)

AreaE is a contribution from the inner integral, and

Fet : is the integrand of the outer integral, which contains exponents designated E_1 and E_2.

The procedure for integration by Simpson's rule is listed next. The outer integral is divided up in 100 strips (M:=100;) and the inner integral is initially divided into 100 strips (N:= 100;), but the number is decremented every time the inner intregal is re-evaluated for the next contribution to the outer integral.

The main program first computes the quantity E_{oo}, followed by repeated calling of the Simpson's procedure for all the combinations of voltages and temperatures.

Finally, an output is generated in the format shown.

```
program Integrate;
const EpSubS=1.04E-10;
      Mlh=1.46E-31;
      Na=1.0E16;
      k=8.621E-5;
      Nv=1.0E19;

var Et,E,E00,AreaEt,AreaE,StepEt,StepE,Etmin,Etmax,Emin,Emax,SumEt,
    SumE,V,T,Uratio,Utotn:real;
    M,N,i,j,l:integer;
    TT:array [1..6] of real;
    VV:array [1..26] of real;
Function Vl(V:real):real;
begin
  Vl:=0.07*sqrt(V);
end;
Function DeltaPhi(V:real):real;
begin
  DeltaPhi:=0.5*Vl(V);
end;
Function Vd0(T:real):real;
begin
  Vd0:=0.509-5.96E-4*T;
end;
Function Es(V,T:real):real;
begin
  Es:=Vd0(T)-Vl(V)+k*T*ln(Nv/Na)+DeltaPhi(V);
end;
Function Vd(V,T:real):real;
begin
  Vd:=0.25*V+k*T+0.5*(Vd0(T)-k*T-0.07*sqrt(V))*
      (1.0+sqrt(1+(V)/(Vd0(T)-k*T-0.07*sqrt(V))));
end;
Function Uten(V,T:real):real;
begin
  Uten:=k*T*exp(-Es(V,T)/(k*T))*
ln((1+exp(Es(V,T)/(k*T)))/(1+exp(Vd0(T)-Vl(V)-Vd(V,T)+DeltaPhi(V))));
end;
Function Ea(V,T:real):real;
begin
  Ea:=-Vd(V,T)-k*T*ln(Nv/Na);
end;
Function U(E,Et:real):real;
begin
  if E < Et then U:=0.0 else U:=1.0;
end;
Function FE(E,V,T:real):real;
begin
    FE:=U(E,Et)*exp(-E/(k*T)-(2*sqrt(-E*E*E))/(3*E00*sqrt(Vd(V,T))));
end;
Function FEt(Et,V,T,AreaE:real):real;
var El,E2:real;
begin
  El:=-Et/(k*T);
  E2:=Es(V,T)/(k*T);
  if El >  174.0 then El:= 174.0;
  if E2 >  174.0 then E2:= 174.0;
    FEt:=1.0/(exp(El)+exp(E2))*AreaE
end;
```

```
procedure Simpson(var Etmin,Etmax,Emin,Emax:real;M,N:integer;
                  var AreaEt,AreaE,StepEt,StepE:real);
var i,j,parity:integer;
begin
  M:=100;
  N:=100;
  Etmin:=Ea(V,T);
  Etmax:=0.0;
  StepEt:=(Etmax-Etmin)/M;
  SumEt:=0.0;
  Et:=Etmin+StepEt;
  for i:=2 to M do begin
    SumE:=0.0;
    Emin:=-Vd(V,T);
    Emax:=0.0;
    StepE:=(Emax-Emin)/N;
    E:=Emin+StepE;
    for j:=2 to N do begin
      if (j-(j div 2)*2)=0 then SumE:=SumE+4.0*FE(E,V,T)
      else SumE:=SumE+2.0*FE(E,V,T);
      E:=E+StepE;
    end;
    N:=N-1;
    AreaE:=StepE*(FE(Emin,V,T)+SumE+FE(Emax,V,T))/3.0;
    if (i-(i div 2)*2)=0 then SumEt:=SumEt+4.0*FEt(Et,V,T,AreaE)
    else SumEt:=SumEt+2.0*FEt(Et,V,T,AreaE);
    Et:=Et+StepEt;
  end;
  AreaEt:=StepEt*(FEt(Etmin,V,T,AreaE)+SumEt+FEt(Etmax,V,T,AreaE))/3.0;
end;
begin(*Main*)
  E00:=5.28E-35*sqrt(1.0E6*Na/(M1h*EpSubS));
  for i:=1 to 26 do read(VV[i]);
  for j:=1 to 6 do read(TT[j]);
  writeln(' Emin   Emax   Etmin    Etmax    V     T    Vd(V,T)',
          '  Es(V,T)      Utfen/Uten            Utotn',
          '                Uten');
  writeln('-------------------------------------------------',
          '----------------------------------------',
          '---------------------------');
  for i:=1 to 26 do begin
    for j:=1 to 6 do begin
      V:=VV[i];
      T:=TT[j];
      Simpson(Etmin,Etmax,Emin,Emax,M,N,AreaEt,AreaE,StepEt,StepE);
      Utotn:=AreaEt/(k*T)+Uten(V,T);
      Uratio:=AreaEt/(Uten(V,T)*k*T);
  writeln(Emin:7:3,Emax:7:3,Etmin:7:3,Etmax:7:3,VV[i]:7:3,
    TT[j]:7:2,Vd(V,T):9:5,Es(V,T):9:5,Uratio,Utotn,Uten(V,T));
      end;
    end;
end;
//GO.INPUT DD *
 0.115 0.175 0.228 0.346 0.387 0.508 0.669 0.772 0.810 0.861 0.933
 1.400 1.630 2.410 2.490 2.560 2.650 2.840 4.490 4.500 4.650 5.440
 6.800 8.770 8.870 9.000
  93 113 133 153 173 193
```

Emin	Emax	Etmin	Etmax	V	T	Vd(V,T)	Es(V,T)	Utfen/Uten	Utotn	Uten
-0.486	0.0	-0.541	0.0	0.115	93.00	0.48560	0.49709	6.7029146713481E+00	4.4889351823950E-27	5.8275800445929E-28
-0.474	0.0	-0.541	0.0	0.115	113.00	0.47363	0.49708	3.6568487030611E+00	1.5800822094311E-22	3.3930288703441E-23
-0.462	0.0	-0.541	0.0	0.115	133.00	0.46166	0.49707	2.4448231911448E+00	2.5085811168895E-19	7.2821766973062E-20
-0.450	0.0	-0.541	0.0	0.115	153.00	0.44968	0.49706	1.8163843389535E+00	5.9200833977287E-17	2.1020154514594E-17
-0.438	0.0	-0.541	0.0	0.115	173.00	0.43770	0.49705	1.4363233353188E+00	3.9868532651847E-15	1.6364220657366E-15
-0.426	0.0	-0.541	0.0	0.115	193.00	0.42571	0.49704	1.1826089256075E+00	1.1270459000205E-13	5.1637555715890E-14
-0.508	0.0	-0.563	0.0	0.175	93.00	0.50796	0.49431	7.0012989629655E+00	6.5532935415244E-27	8.1902870669584E-28
-0.496	0.0	-0.563	0.0	0.175	113.00	0.49593	0.49430	3.7963949381986E+00	2.1515218040979E-22	4.4857061018122E-23
-0.484	0.0	-0.563	0.0	0.175	133.00	0.48390	0.49429	2.5283134964991E+00	3.2546036673384E-19	9.2242474218000E-20
-0.472	0.0	-0.563	0.0	0.175	153.00	0.47186	0.49428	1.8757839706105E+00	7.4190361892343E-17	2.5798308444077E-17
-0.460	0.0	-0.563	0.0	0.175	173.00	0.45981	0.49427	1.4828927058473E+00	4.8670751827458E-15	1.9602438604309E-15
-0.448	0.0	-0.563	0.0	0.175	193.00	0.44775	0.49427	1.2213199588197E+00	1.3478394148113E-13	6.0677409819314E-14
-0.528	0.0	-0.583	0.0	0.228	93.00	0.52790	0.49224	7.2956217916917E+00	8.7608805653551E-27	1.0560848584164E-27
-0.516	0.0	-0.583	0.0	0.228	113.00	0.51581	0.49223	3.9204486832101E+00	2.7189079680081E-22	5.5257317839442E-23
-0.504	0.0	-0.583	0.0	0.228	133.00	0.50371	0.49222	2.6018104557990E+00	3.9640645917422E-19	1.1005755689781E-19
-0.492	0.0	-0.583	0.0	0.228	153.00	0.49160	0.49221	1.9277138932681E+00	8.8017274354077E-17	3.0063482144365E-17
-0.479	0.0	-0.582	0.0	0.228	173.00	0.47947	0.49220	1.5233441538735E+00	5.6606231773299E-15	2.2433020753988E-15
-0.467	0.0	-0.582	0.0	0.228	193.00	0.46734	0.49219	1.2547220578730E+00	1.5433371695385E-13	6.8449109465597E-14
-0.572	0.0	-0.628	0.0	0.346	93.00	0.57213	0.48837	7.9646508669621E+00	1.5235135449802E-26	1.6994677958903E-27
-0.560	0.0	-0.627	0.0	0.346	113.00	0.55988	0.48836	4.1958268039223E+00	4.2416165202294E-22	8.1635063682790E-23
-0.548	0.0	-0.627	0.0	0.346	133.00	0.54760	0.48835	2.7637383034904E+00	5.7646510426010E-19	1.5316290819835E-19
-0.535	0.0	-0.626	0.0	0.346	153.00	0.53531	0.48834	2.0419635440524E+00	1.2177714101034E-16	4.0032413027578E-17
-0.523	0.0	-0.626	0.0	0.346	173.00	0.52299	0.48833	1.6123281919095E+00	7.5433282677484E-15	2.8875882789576E-15
-0.511	0.0	-0.626	0.0	0.346	193.00	0.51065	0.48832	1.3281450683100E+00	1.9969050214061E-13	8.5772362237533E-14
-0.587	0.0	-0.643	0.0	0.387	93.00	0.58737	0.48718	8.2004669385051E+00	1.8085699380558E-26	1.9657371198050E-27
-0.575	0.0	-0.642	0.0	0.387	113.00	0.57505	0.48717	4.2907253888800E+00	4.8668351992348E-22	9.1988051571603E-23
-0.563	0.0	-0.642	0.0	0.387	133.00	0.56270	0.48716	2.8192328094957E+00	6.4721000874194E-19	1.6946073754205E-19
-0.550	0.0	-0.641	0.0	0.387	153.00	0.55034	0.48715	2.0811469042265E+00	1.3464133792970E-16	4.3698448050306E-17
-0.538	0.0	-0.641	0.0	0.387	173.00	0.53795	0.48714	1.6429186275539E+00	8.2445945863106E-15	3.1195037563230E-15
-0.526	0.0	-0.640	0.0	0.387	193.00	0.52553	0.48713	1.3534410131287E+00	2.1628788627029E-13	9.1902828693698E-14
-0.632	0.0	-0.687	0.0	0.508	93.00	0.63182	0.48401	8.9037448209 91E+00	2.8739132908366E-26	2.9018451516305E-27
-0.619	0.0	-0.687	0.0	0.508	113.00	0.61930	0.48400	4.5615750569391E+00	7.0418663697441E-22	1.2661640448344E-22
-0.607	0.0	-0.686	0.0	0.508	133.00	0.60675	0.48399	2.9804580635384E+00	0.8841345043746E-18	2.2211878388405E-19
-0.594	0.0	-0.685	0.0	0.508	153.00	0.59416	0.48398	2.1952007273954E+00	1.7652180745389E-16	5.5245921153060E-17
-0.582	0.0	-0.685	0.0	0.508	173.00	0.58153	0.48397	1.7322756972828E+00	1.0480791145706E-14	3.8359200559918E-15
-0.569	0.0	-0.684	0.0	0.508	193.00	0.56887	0.48396	1.4275836137096E+00	2.6837347434190E-13	1.1055169133054E-13
-0.690	0.0	-0.745	0.0	0.669	93.00	0.68979	0.48033	9.8544131267163E+00	4.9493207551442E-26	4.5597313252821E-27
-0.677	0.0	-0.744	0.0	0.669	113.00	0.67697	0.48032	4.9232121607977E+00	1.0865573723885E-21	1.8344056280472E-22
-0.664	0.0	-0.743	0.0	0.669	133.00	0.66412	0.48031	3.1892299898615E+00	1.2737374607696E-18	3.0405049707278E-19
-0.651	0.0	-0.742	0.0	0.669	153.00	0.65121	0.48030	2.3436277421979E+00	2.4248535218421E-16	7.2521635445223E-17
-0.638	0.0	-0.741	0.0	0.669	173.00	0.63826	0.48029	1.8494292027347E+00	1.3893633495899E-14	4.8759356725078E-15
-0.625	0.0	-0.740	0.0	0.669	193.00	0.62526	0.48028	1.5254585685586E+00	3.4595450472474E-13	1.3698680668604E-13
-0.726	0.0	-0.782	0.0	0.772	93.00	0.72620	0.47820	1.0470916588604E+01	6.7891626374725E-26	5.9185877475713E-27
-0.713	0.0	-0.780	0.0	0.772	113.00	0.71320	0.47819	5.1499408669840E+00	1.3973171372148E-21	2.2720822320688E-22
-0.700	0.0	-0.779	0.0	0.772	133.00	0.70014	0.47818	3.3195912463070E+00	1.5743220621340E-18	3.6446088816389E-19
-0.687	0.0	-0.778	0.0	0.772	153.00	0.68703	0.47817	2.4368980139072E+00	2.9163522148871E-16	8.4854197101173E-17
-0.674	0.0	-0.777	0.0	0.772	173.00	0.67386	0.47816	1.9236453108341E+00	1.6372736050405E-14	5.6001102424199E-15
-0.661	0.0	-0.776	0.0	0.772	193.00	0.66063	0.47815	1.5879048060665E+00	4.0121263524444E-13	1.5503376874757E-13
-0.740	0.0	-0.795	0.0	0.810	93.00	0.73951	0.47746	1.0699892990164E+01	7.5903663898224E-26	6.4875519769311E-27
-0.726	0.0	-0.794	0.0	0.810	113.00	0.72644	0.47745	5.2326863057428E+00	1.5268660245980E-21	2.4497719758351E-22
-0.713	0.0	-0.793	0.0	0.810	133.00	0.71331	0.47744	3.3656764145314E+00	1.6958950674834E-18	3.8846100957884E-19
-0.700	0.0	-0.791	0.0	0.810	153.00	0.70012	0.47743	2.4710228732680E+00	3.1126672379576E-16	8.9675791592435E-17